



Skolkovo Institute of Science and Technology

Skolkovo Institute of Science and Technology

TAILORING THE FUNCTIONAL PROPERTIES OF NITI SHAPE MEMORY ALLOY
BY HIGH-RESOLUTION LASER POWDER BED FUSION

Doctoral Thesis

by

STANISLAV CHERNYSHIKHIN

DOCTORAL PROGRAM IN MATHEMATICS AND MECHANICS

Supervisor

Associate Professor Igor Shishkovsky

Moscow - 2023

© Stanislav Chernyshikhin 2023

I hereby declare that the work presented in this thesis was carried out by myself at Skolkovo Institute of Science and Technology, Moscow, except where due acknowledgement is made, and has not been submitted for any other degree.

Candidate (Stanislav Chernyshikhin)

Supervisor (Associate Professor Igor Shishkovsky)

Abstract

Among the shape memory alloys, NiTi is the most applicable due to the highest actuation energy density, biocompatibility, and corrosion resistance. However, despite the aforementioned advances, poor machining of the material limits the utilization of NiTi in advanced engineering problems. In the last decade, Laser Powder Bed Fusion (LPBF) received increased attention and appears to be a promising manufacturing technology for intermetallic NiTi alloy. Many efforts have been made to achieve acceptable mechanical and functional properties. Furthermore, several studies have demonstrated a strong influence of the LPBF process parameters on the resulting material properties, i.e. temperatures of the martensitic phase transformation, reversible/irreversible strain after cyclic loading, phase composition, chemical composition, etc. However, the mechanisms of functional properties altering during LPBF consolidation remain unexplored at the present state of the art. This thesis aims to advance the knowledge about tailoring material properties of NiTi under laser influence.

In this work, thin-walled samples were manufactured from pre-alloyed NiTi powder via LPBF in a wide window of laser power and scanning speed. Excluding hatch spacing by employing a single track-based scanning strategy allowed to reveal the pure effect of the laser influence. NiTi samples were characterized by various methods such as differential scanning calorimetry, X-ray diffraction, and mechanical tests. Finally, the feasibility of the 4D printing concept was demonstrated experimentally.

Simulation of the melt pool formation and consolidation of thin walls were carried out with a high fidelity physical model based on an LBM hydrodynamic solver. In the simulations, many significant aspects were taken into account such as Marangoni effect, recoil pressure, two-component evaporation, powder recoating, and energy deposition by ray tracing of the laser beam. The results of simulation were validated with the obtained experimental data. Combined results of experimental study and numerical simulation shed light on the mechanisms of tailoring functional properties by laser process parameters. NiTi melt surface tension, thermal diffusivity of solid, and heat capacity were measured experimentally for the utilization in the model.

Importantly, developed approaches of high-resolution LPBF possess possible industrial applications. Manufacturing of patient-specific stents for coronary vessels with

superelastic behavior was only known to date. In the thesis, a novel application for high-resolution LPBF was proposed, namely the production of endodontic files for root canal treatment. Such instruments have complex geometry, high requirements in mechanical properties, surface roughness, and superelasticity. In this regard, the thesis expanded existing knowledge about the technology for manufacturing of micro devices from intermetallic NiTi alloy.

Publications

- [1] **S. V. Chernyshikhin**, D.G. Firsov, I. V. Shishkovsky, Selective Laser Melting of Pre-Alloyed NiTi Powder: Single-Track Study and FE Modeling with Heat Source Calibration, *Materials (Basel)*, 14 (2021) 7486.
- [2] **S. V. Chernyshikhin**, I.A. Pelevin, F. Karimi, I. V. Shishkovsky, The Study on Resolution Factors of LPBF Technology for Manufacturing Superelastic NiTi endodontic Files, *Mater.* 2022, Vol. 15, Page 6556, 15 (2022) 6556.
- [3] **S. V. Chernyshikhin**, I. V. Shishkovsky, Method for direct laser synthesis of superelastic Nickel Titanium endodontic instruments, Patent № 2792335, March 2023.
- [4] **S. V. Chernyshikhin**, S.N. Zhevnenko, D.Yu. Ozherelkov, V.Yu. Egorov, D.Yu. Ozherelkov, I. V. Shishkovsky, Surface tension measurement of equiatomic NiTi alloy for the melt pool simulation during Laser Powder Bed Fusion. Under revision.

Acknowledgments

I express my gratitude to my family and my wife for their constant support. I thank my scientific supervisor Prof. Igor Shishkovsky for the opportunity to implement this study. I acknowledge my dear colleagues Anton Nalivaiko from Moscow Polytechnic University, Ivan Pelevin, Dmitry Ozherelkov, Sergey Zhevnenko, Alexander Gromov from NUST MISiS, and Andrey Zakirov, Sergey Belousov, Boris Korneev, Maria Bogdanova from Kintech lab for all valuable advice. The work was financially supported by the Russian Science Foundation (RSF), Grants No. 19-79-30025, 21-79-10240, 21-79-10239. The presentation on the research was recognized as the best oral report at the fifth international conference “Shape Memory Alloys V”. The startup idea on NiTi endodontic files printing was developed with the support of the Skoltech Translational Research and Innovation Program.

Table of Contents

Table of Contents	7
List of Abbreviations	10
List of Figures	12
List of Tables	15
Chapter 1. Introduction	16
1.1 NiTi shape memory alloy	16
1.1.1 NiTi alloy as a smart material	16
1.1.2 Functional properties of NiTi.....	17
1.1.3 NiTi metallurgy basics	20
1.1.4 Characterization of NiTi properties	22
1.1.5 Ni content dependence	22
1.2 Additive manufacturing concept	23
1.2.1 Laser Powder Bed Fusion	25
1.2.2 LPBF manufacturing of NiTi parts	26
1.2.3 4D printing concept.....	29
1.2.4 LPBF manufacturing of micro-objects	30
1.3 Mesoscale simulation of the melt pool during LPBF.....	32
1.4 Applications of SMA	33
1.5 Thesis objectives	35
Chapter 2. Materials and methodology	36
2.1 Materials and equipment	36
2.1.1 Powder analysis	36
2.1.2 LPBF installation	36
2.2 Characterization methods.....	37
2.2.1 Differential scanning calorimetry	37

2.2.2	Microstructural studies.....	37
2.2.3	X-Ray diffraction analysis	38
2.2.4	Mechanical tests.....	38
2.2.5	Pendant drop tensiometry	38
2.3	Simulation procedure	39
2.3.1	Fluid dynamics in the melt pool.....	40
2.3.2	Heat conduction	41
2.3.3	Marangoni effect.....	42
2.3.4	Evaporation solver	43
Chapter 3.	Manufacturing of NiTi via Laser Powder Bed Fusion.....	45
3.1	NiTi powder characteristics	45
3.2	Single track analysis.....	47
3.2.1	Width of the melt pool	49
3.2.2	Depth of the melt pool	51
3.3	Single Track-Based Thin Walls	53
3.3.1	Samples manufacturing for mechanical testing	59
3.3.2	Microstructure of thin-walled samples	61
3.4	Static mechanical testing of thin wall samples.....	62
3.4.1	Static uniaxial tensile tests until fracture	63
3.4.2	Single loading cycle uniaxial tensile tests	64
3.5	Characteristic temperatures of phase transformation.....	67
3.6	Phase composition variation.....	68
3.7	High-resolution LPBF 4D printing concept.....	72
Chapter 4.	Simulation of the melt pool during LPBF.....	75
4.1	Thermophysical properties of NiTi for LPBF simulation.....	75
4.1.1	Surface tension measurements of NiTi melt.....	76

4.1.2	Graphite crucible and NiTi melt interaction	78
4.1.3	Thermal diffusivity	79
4.2	Powder layer simulation.....	81
4.2.1	Layer thickness during LPBF	81
4.2.2	Generated layer analysis	82
4.3	Single tracks calculations and experimental convergence	84
4.4	Effect of the surface tension on the melt pool formation.....	89
4.5	Simulation of thin walls consolidation.....	91
4.6	Multicomponent evaporation and Ni depletion.....	93
Chapter 5. Endodontic files manufacturing via high-resolution LPBF		97
5.1	Regime optimization for file manufacturing.....	98
5.2	SAF manufacturing via high-resolution LPBF	99
5.3	Characterization of SAF Samples	101
5.4	Simulation of the layer-wise consolidation for SAF	103
Conclusions.....		106
Appendix A. Partial Gibbs free energy, activity coefficient, and activity.....		109
Bibliography		110

List of Abbreviations, Abbreviations

SMA – Shape Memory Alloy
TT – Transformation Temperature
SME – Shape Memory Effect
SE – Superelasticity
BCC – body-centered cubic
OWSME – One-Way Shape Memory Effect
PE – Pseudoelasticity
TWSME – Two-Way Shape Memory Effect
ED – elastic deformation
PD – plastic deformation
DSC – Differential Scanning Calorimetry
AM – Additive Manufacturing
SLA – stereolithography
EBM – electron beam melting
DMD – direct metal deposition
LPBF – Laser Powder Bed Fusion
SLM – selective laser melting
VED – volumetric energy density
FE – finite element (method)
KiSSAM – Kintech simulation software for additive manufacturing
LBM – Lattice Boltzmann method
PDF – particle distribution functions
LBE – Lattice Boltzmann equation
DFs – distribution functions
HTSMAs – high temperature shape memory alloys
PSD – particle size distribution
EIGA – electrode induction-melting gas atomization
ICP-MS – inductively coupled plasma mass spectrometry,
OM – optical microscopy
BD – building direction

DIC – digital image correlation

XRD – X-Ray diffraction analysis

SEM – Scanning Electron Microscopy

EDX – Energy-Dispersive X-ray spectroscopy

HAZ – Heat Affected Zone

SAF – Self-Adjusting Files

E_v – volumetric energy density

P – laser power

V – laser scanning speed

h – hatch distance

t – layer thickness

List of Figures

Figure 1. Actuation energy density diagram indicating typical ranges of actuation stress, actuation strain, and the actuation energy densities of different active materials [1].	16
Figure 2. Change in phase fraction during cooling and heating of SMA.	18
Figure 3. Structural changes in SMA for a) OWSME and b) SE.	19
Figure 4. Schematic diagram of the thermomechanical response of NiTi depending on the stress-temperature condition.	20
Figure 5. Phase diagram of Ni-Ti system [13].	21
Figure 6. Typical DSC response of heating/cooling cycle of SMA with marked characteristic temperatures.	22
Figure 7. Dependence of experimental M_s and calculated T_0 temperatures from Ni content. [22]	23
Figure 8. Scheme of LPBF system [34].	25
Figure 9. Particle size distribution histogram with cumulative curve.	46
Figure 10. Results of the SEM powder analysis: a) SEM image of powder; b) powder particle with dendritic fragments under high magnification; c) Ni $K\alpha_1$; d) Ti $K\alpha_1$.	46
Figure 11. Cross-sections of NiTi single-track deposits: (a) common shape of the melt pool for the LPBF process; (b) no bonding defect; (c) appearance of the pores during keyhole mode in the longitudinal cross-section.	48
Figure 12. Micrographs of the single tracks' top view.	49
Figure 13. Cross-sections of single-track deposits for all combinations of parameters.	52
Figure 14. The depth-to-width ratio for the experimentally obtained single tracks.	53
Figure 15. The samples of thin walls in Materialise Magics software.	54
Figure 16. OM of cross-sections for single track based thin walls. Samples with lack of fusion defect are highlighted with red.	56
Figure 17. Dependence of wall thickness and width of single tracks on linear energy density for vertical samples.	57
Figure 18. Dependence of wall thickness on linear energy density for inclined walls.	58
Figure 19. a) OM of walls with different inclined angles; b) schematic representation of the overlapping between adjacent tracks during single track manufacturing of inclined objects.	59

Figure 20. Cassette assemblies of thin walls in z orientation.	60
Figure 21. Drawing of a) flat dog-bone sample, b) mounting for mechanical tests.	60
Figure 22. SEM images of thin wall samples' microstructure for regimes: a) P50V600, b) P100V850, c) P150V500.	61
Figure 23. Stress-strain curves with corresponding DIC images for sample a) P50V600 [until fracture] and b) P100V850 [single cycle loop]	62
Figure 24. SEM images of fracture surface for samples P100V350 (a,c) and P100V1350 (b,d) with magnification of 10k (a,b) and 30k (c,d).....	63
Figure 25. Results of mechanical tests with one cycle of loading-unloading up to 3 % .	65
Figure 26. DSC curves of as-built samples with different LPBF regimes a) cooling and b) heating.....	67
Figure 27. Dependence of the M_s temperature on the linear energy density.	68
Figure 28. XRD patterns for as-built samples consolidated under different process conditions.....	70
Figure 29. Change in integral intensity ratio for B19' with relation to the consolidation regimes.....	71
Figure 30. a) design of thin-walled structure, b) consolidated sample on the NiTi substrate.	72
Figure 31. Multistage SME activation: a) initial state, b) shape recovery of samples manufactured with low linear energy density, c) activation of SME for samples P100V200 and P50V100, d) final state (P150V300 with irrecoverable strain).....	74
Figure 32. a) a typical image of a NiTi drop with a defined profile (green), an axis of symmetry (red), and a fitted profile (yellow) b) thermal imaging of a drop, c) surface tension of NiTi melt at constant temperature.....	77
Figure 33. Analysis of solidified melt in the graphite: a) SEM image and chemical mapping, b) distribution of the elements along the marked line perpendicular to the channel	79
Figure 34. Temperature dependence of thermal diffusivity for consolidated NiTi.	80
Figure 35. Generated powder bed: isometry of a) 30 μm , b) 45 μm ; cross-sections of c) 30 μm , d) 45 μm , e) 60 μm , f) 100 μm	83
Figure 36. Particle size distribution along the z-axis.....	84
Figure 37. Calculated and experimentally obtained the transverse melt pool's shape.	85

Figure 38. Calculated morphology and experimentally obtained top views of single tracks.	87
Figure 39. Validation of the model by width and depth of the melt pool for all regimes.	89
Figure 40. Calculated temperature field with velocity vectors, color-coded by magnitude for different surface tension values at the same time step.	90
Figure 41. Normalized frequency distribution of velocity magnitude extracted from the velocity field.	91
Figure 42. Thermal history analysis for thin wall processed with a) P150V300 regime, and b) P150V1350.	92
Figure 43. Distribution of Ni in thin wall consolidated with regimes a) P50V1000, b) P150V500.	95
Figure 44. a) dependence of calculated change in Ni content from linear energy density, b) dependence of experimentally measured martensite start transformation temperature from calculated Ni content. Frenzel et. al [22].	96
Figure 45. 3D-model of Self-Adjusting File adopted for LPBF manufacturing: a) isometry; b) XZ plane view; c) YZ plane view; d) sweep of the SAF, supplemental support strut highlighted with a solid line, critical inclined angle highlighted with a dashed line.	97
Figure 46. P-V map of high-resolution LPBF process conditions.	98
Figure 47. a) Matrix of LPBF regimes of Self-Adjusting files fabrication; b) Produced samples of SAF.	99
Figure 48. 3D-printed SAF samples fabricated with various regimes: a) P100V850, b) P150V1100, c) P100V400, d) P50V200.	100
Figure 49. High magnification images of 3D-printed SAF sample P100V850: a) the upper part, b) the tip, c) the strut of the upper part.	101
Figure 50. Differential scanning calorimetry for raw powder and sample P100V850. ...	102
Figure 51. XRD patterns of initial NiTi powder and 3D-printed P100V850 sample.	103
Figure 52. Rendered SAF geometry after simulation: a) layer 1250, b) layer 1350, c) layer 1484.	105

List of Tables

Table 1. The parameter combinations for the printing of NiTi reported in the literature.	28
Table 2. Problems of LPBF simulations and its scales.	33
Table 3. The combinations of parameters used in the experiments.	47
Table 4. The window of process parameters used for the optimization procedure.	54
Table 5. Mechanical properties of NiTi thin wall samples.	66
Table 6. Characteristic temperatures of austenite and martensite transformations.	68
Table 7. Summarized thermophysical properties for the melt pool simulation.	75
Table 8. Surface tension of equiatomic liquid NiTi obtained by different methods.	77
Table 9. Comparison of powders for layer density analysis.	82
Table 10. Utilized sets of mixing parameters.	94
Table 11. Temperatures of phase martensitic transition of initial powder material and fabricated sample.	102

Chapter 1. Introduction

1.1 NiTi shape memory alloy

1.1.1 NiTi alloy as a smart material

Smart materials are a class of materials that respond to specific external stimuli by changing their properties in a controlled and, importantly, reversible way. Smart materials are classified by a property-stimulus couple and a microscopic structure. Thus, piezoelectricity refers to the coupling of electric and mechanical fields in such materials as ceramics or polymers for instance. According to the aforementioned, one can define shape-memory alloys (SMAs) as a type of smart material with thermo-mechanical coupling in metallic alloys. SMAs are capable to return to their original shape under certain environmental conditions. The uniqueness and relevance of SMAs lies in the highest actuation energy density compared with other smart materials, as shown in Figure 1.

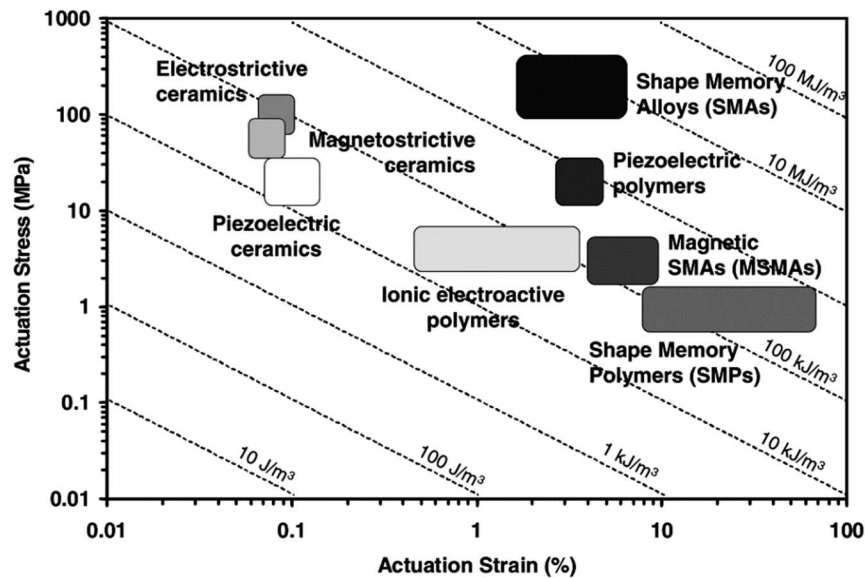


Figure 1. Actuation energy density diagram indicating typical ranges of actuation stress, actuation strain, and the actuation energy densities of different active materials [1].

Nitinol is a SMA with an equiatomic composition in Nickel – Titanium system. The material was named after its components (NiTi) and the Naval Ordnance Laboratory (NOL), where it was developed [2]. The recoverable strain for Nitinol reaches 8 % [1], which is higher compared to other SMAs (5% for Cu-based and less than 5 % for Fe-based [3]). The purely elastic strain value at the yield point for conventional structural steels is an order of magnitude lower than the recoverable strain of NiTi. Obtaining such

non-trivial properties in SMAs allows solving engineering problems in several areas at a new technological level.

High mechanical strength and relatively low modulus of elasticity are essential characteristics of the NiTi alloy as a biomedical material [4]. These properties make this SMA an excellent material for various implants, such as dental implants, joints, and spine fixators [5]. Other distinctive applications of Nitinol include actuators, fittings, and valves [6]. For some medical devices like coronary stents, dental files, and braces such material is indispensable [7].

1.1.2 Functional properties of NiTi

Functional properties of nitinol are related to the martensite phase transformation, which in turn can be induced by temperature or stress. The phase transformation primarily implies a diffusionless mechanism and occurs also in other systems such as Au – Cd [8], Fe – Mn – Si [9], Cu – Al – Ni [10], etc. The transformation from parent austenite crystal lattice with a higher order of symmetry to martensitic phase takes place by shear distortion of the lattice structure. During this rearrangement, the atoms move from their original position to a distance less than interatomic. The key point of the martensitic phase transformation in SMAs is that the transformation could be reversed by an external stimulus. The thermodynamically favorable condition for the reverse phase transformation is provided by a change in temperature. Martensitic transformation for nitinol is considered thermoelastic, since the deformation can be fully recovered, whilst during the non-thermoelastic transformation only part of the induced deformation will be restored (e.g. Fe – Ni system [11]).

Conventionally, four temperatures are considered to describe the martensitic phase transformation and are hereinafter referred to as transformation temperatures (TTs). Assuming SMA has a phase composition presented only by martensite at ambient temperature, the first crystals of the high-temperature phase are formed at the starting temperature – A_s during the consistent heating as schematically shown in Figure 2. The temperature at which the last crystal of the low-temperature phase is transformed into the austenite phase is the A_f temperature (fraction of austenite = 1). During the cooling process M_s temperature is the temperature of the first martensite crystal formation, and below the

M_f temperature, the phase transition is finished, and the martensite fraction is 1. Conventionally, the transformation during heating ($M \rightarrow A$) and cooling ($A \rightarrow M$) is referred to as forward and reverse respectively.

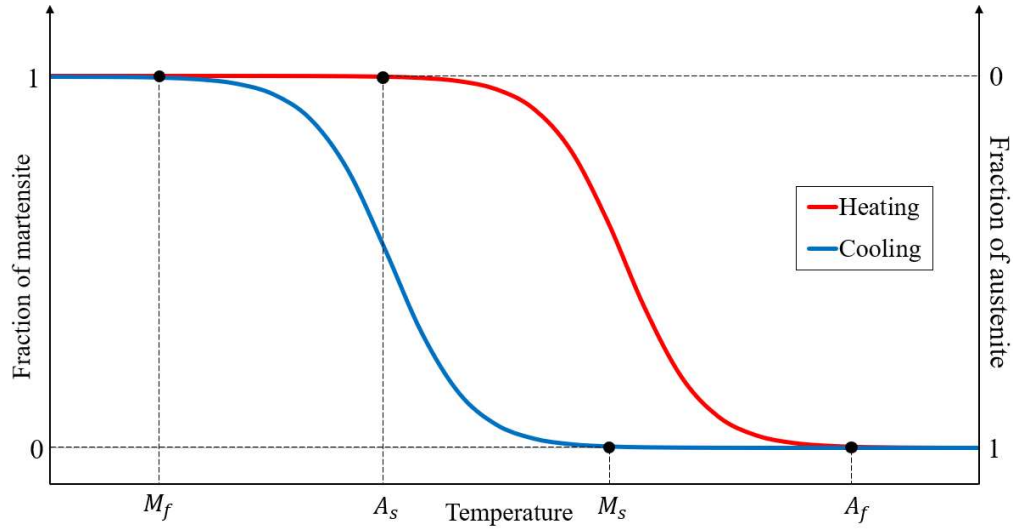


Figure 2. Change in phase fraction during cooling and heating of SMA.

Depending on the SMA's TTs and ambient temperature T_0 , NiTi may exhibit shape memory effect (SME) or superelastic (SE) behavior. Assume that SMA has the TTs such that $M_f > T_0$, corresponding to the case of fully martensitic phase composition. Martensite has a monoclinic crystallographic lattice with a twinned structure, as schematically shown in Figure 3a. During the loading of SMA (first arrow on the scheme), the crystal lattice experiences shear distortion resulting in the detwinning process due to the tendency of strain energy minimization. Induced deformation in the material can be subdivided into purely elastic and residual deformation accommodated by detwinning. After unloading of the material, the pure elastic deformation will be restored as in conventional materials. When material temperature is increased above A_f , the crystal lattice transforms into the austenite structure with a body-centered cubic (BCC) crystallographic lattice. The crystal structure of the austenitic and martensitic phases will be referred to as B19' and B2 respectively according to Strukturbericht designation. During the transition to the BCC lattice (the second arrow in Figure 3a), the macroscopic shape changes from a deformed state to the one that was present at T_0 temperature (in the martensite phase). The process of strain recovery during the temperature increases to $T > A_f$ is considered as a one-way shape memory effect (OWSME). Emphasizing the "One-way" effect associated with the

conservation of the shape state during the cooling stage of the material, when the crystal structure reverts back to the self-accommodated twinned martensite.

On the other hand, if deformation occurs at a temperature T_0 slightly above A_f the mechanical response differs. As the condition $T_0 > A_f$ is satisfied, the thermodynamically favorable phase is the parent B2. In this case, the martensitic phase transformation is induced by the stress but accommodated by the same aforementioned mechanisms. Thus, after the unloading of the material, the reverse transformation occurs without additional external stimulus, since SMA is already at a temperature above A_f (Figure 3b). Since the return of deformation is observed in the isothermal conditions, the effect was classified as the superelastic (SE) or pseudoelastic (PE) behavior. In this dissertation, the SE option is used over PE.

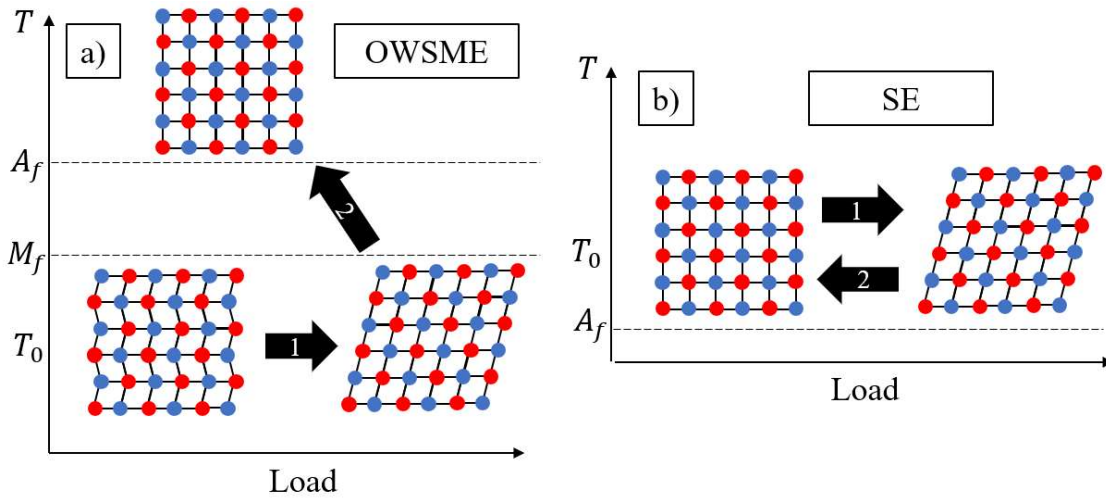


Figure 3. Structural changes in SMA for a) OWSME and b) SE.

The third common thermomechanical response of SMA is a two-way shape memory effect (TWSME). The result of TWSME lies in the reversible change between two shapes during the cooling/heating cycle. In comparison with a basic OWSME where the operational cycle requires a deformation step, the TWSME cycle is achieved solely through the temperature variation. Such a non-intrinsic material behavior could expand various applications, especially for actuators, however, the implementation of this response is highly complicated. To achieve TWSME a thermomechanical treatment is required [12]. The procedure of cyclic loading along a constant direction at a constant temperature is referred to as training. The training results in the redistribution of defects and creates an internal stress state inside the material. The aforementioned microstructure changes lead to

the formation of the preferred variants during transformation which in turn leads to two different macroscopic shapes during transformation. Since TWSME is only possible after mechanical treatment, it is not further discussed in the thesis. Thus, the abbreviation SME is used for OWSME hereafter.

If SE and SME are only considered, the possible thermomechanical responses of NiTi are summarized, as schematically shown in Figure 4. Depending on stress conditions and ambient temperature, the material may experience elastic deformation (ED), plastic deformation (PD), SE, SME, and its combinations. The simplest case referred to SME if the stress was induced at a temperature below A_s . As discussed previously in the case of ambient temperature higher than A_f , pure SE is observed. If the temperature during loading is in the range of $A_s < T < A_f$, a mixture of SE and SME appears, meaning partial shape recovery immediately during unloading and full recovery after additional heating. In all three cases, once the stress increases after the complete transformation to the B2 phase, ED and PD will develop in austenite. It should be noted that M_d temperature is a limiting value below which stress-induced martensite formation is possible. If the temperature is higher than M_d the mechanism of deformation refers to the conventional materials, i.e. ED then PD by a dislocation slip.

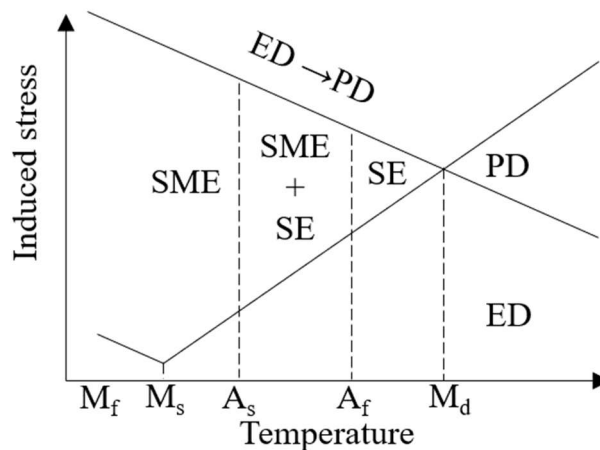


Figure 4. Schematic diagram of the thermomechanical response of NiTi depending on the stress-temperature condition.

1.1.3 NiTi metallurgy basics

The phase diagram of Ni-Ti system is presented in Figure 5. NiTi is an intermetallic alloy with equiatomic composition at equilibrium conditions. The broadest homogeneity

range is observed at an eutectic temperature of 1118 °C. Liquidus temperature is considered as 1310 °C, when solidus for conventionally manufactured NiTi lies at 1270 °C.

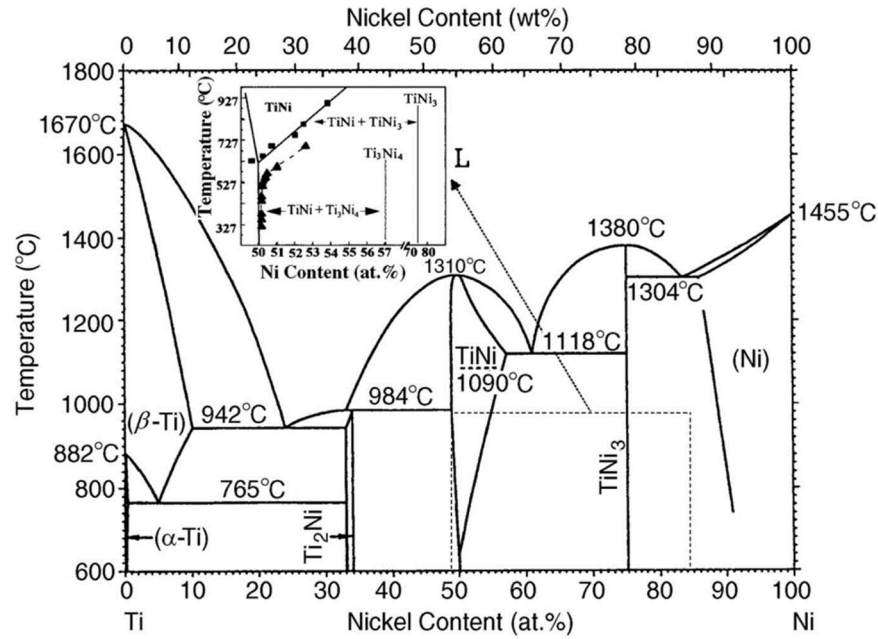


Figure 5. Phase diagram of Ni-Ti system [13].

According to the phase diagram of the Ni-Ti system, the mutual solubility region is narrow especially in the vicinity of ambient temperature so that small variations of alloy composition could lead to another phase formation depending on which element was enriched. As far as the solubility line of NiTi from the Ni-rich side has a significant incline, the supersaturated solution of Ni in the NiTi matrix can be reached. Alloys with a Ni content above the equiatomic composition are considered Ni-rich alloys. Due to the instability of supersaturated solid solution, Ni-rich phases are formed in the NiTi matrix according to the subsequence in Expression (1). Ni_4Ti_3 and Ni_3Ti_2 are metastable intermediate phases when the only Ni_3Ti is equilibrium (Figure 5).



It should be noted that Ni_4Ti_3 and Ni_3Ti_2 metastable phases are observed in the form of precipitations [14,15]. The nucleation of lenticular coherent Ni_4Ti_3 is conventionally achieved during the aging heat treatment and increases the strength of NiTi SMAs [16,17]. The occurrence of these phases within the crystal structure of the material has a significant influence on the phase transition, shifting the transition temperature, and affecting hysteresis and other martensitic transformation features through the rise of coherency stress fields [18,19].

1.1.4 Characterization of NiTi properties

The detection of martensite transformation is a fundamental experiment for the assessment of SMAs' properties. Change of crystal lattice entails a change in various physical properties. In such a way, the transformation can be characterized by temperature dependence of electrical resistivity or Young's modulus (via dynamic mechanical analysis). However, direct measurements of TTs are commonly carried out by the differential scanning calorimetry (DSC) technique due to the most convenient sample preparation. DSC equipment consists of two pans, heaters, and thermometers. Once the NiTi sample is placed in one crucible, the system starts to heat both cells. When the phase transformation occurs, the sample starts to absorb or excrete enthalpy. A typical difference in the heat flow during a single heating/cooling loop is schematically demonstrated in Figure 6 as a dependence on temperature. By scanning a particular temperature range, depending on NiTi composition and heat treatment, all TTs (A_s , A_p , A_f , M_s , M_p , M_f) can be obtained. By integrating the area enclosed between the peak and the baseline, the transformation enthalpy can be calculated. Additionally, the temperature hysteresis effect is common to the transition in NiTi [15,20] and characterized by ΔT . It should be noted that start temperatures of the phase transformation have the lowest dependence on the process conditions such as crucible properties, heating rate, and heaters' settings [21].

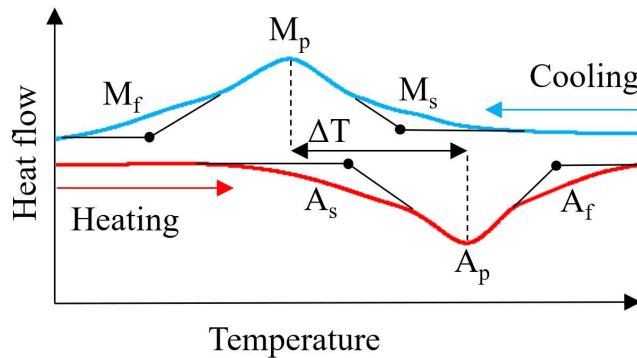


Figure 6. Typical DSC response of heating/cooling cycle of SMA with marked characteristic temperatures.

1.1.5 Ni content dependence

Characteristic temperatures of the phase transformation of NiTi alloy are highly sensitive to its composition. For convenience of results comparison, the two following

agreements should be mentioned. At first, most of the classical works refer to the start of the martensitic phase transformation, nevertheless, all characteristic temperatures are affected. Secondly, for evaluation of the composition change Nickel mass % was utilized. Frenzel et al. [22] demonstrated a strong dependence on the characteristic temperatures from the Ni content. The slope at the Ni-rich side was 83 K / at. % Ni as demonstrated in Figure 7. In this regard, tailoring alloy TTs of NiTi only by direct control of composition is complicated [15].

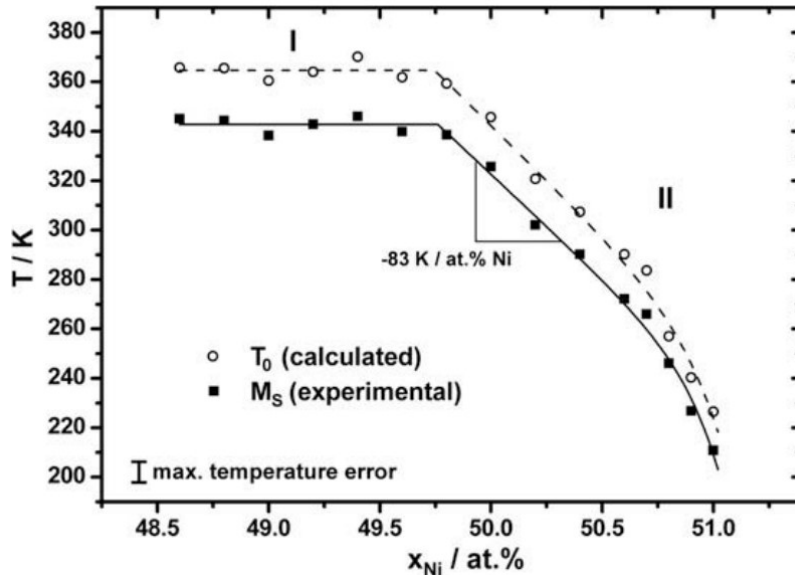


Figure 7. Dependence of experimental M_s and calculated T_0 temperatures from Ni content. [22]

It is worth mentioning that TTs of NiTi alloy vary in a relatively wide temperature range, namely from -60 to +80 °C as was shown. Concerning Ni content NiTi alloys can be subdivided by chemical composition into Ni-rich or Ti-rich with Ni content of 49 to 50 at. % Ni (54 to 55 wt.%) and from 50 to 51 at. % Ni (55 to 56 wt.%) respectively. The chemical composition of the final parts is chosen depending on the desired functional properties at operating temperature, however, Ni-rich alloys are mainly considered for SE behavior, and Ti-rich alloys for SME.

1.2 Additive manufacturing concept

The machining of nitinol is known to be a tedious process due to the strongly pronounced strain-hardening effect, unconventional stress-strain characteristics, and high ductility of the material [23]. Those peculiarities lead to unsuitable cheap formation, poor

surface finish, and increased wear of cutting tools during the milling of NiTi [24]. These limitations restrict the manufacturing of nitinol in the form of rods and plates [25], which require additional manufacturing steps such as cutting [1], welding [26], or drilling [27]. Conventional powder metallurgy and casting are also complicated due to the absorption of impurities [28], the formation of metastable intermetallic phases [25], and the inhomogeneous mixing of the liquid phase [29]. As a result, attempts have been made to manufacture this material using different approaches, such as additive manufacturing (AM).

AM is recognized as a new trend in the production of complex geometric parts [30]. In contradistinction to classical subtractive technologies where the material is removed from the blank to obtain the final shape, the AM approach refers to the subsequent addition of the material in the required places.

Existing AM technologies can be classified by raw material for production. The technologies for polymers belong to the most spread class in the current state of the art. Fused deposition modeling [31] and digital light processing [32] are working with thermoplastic and photosensitive polymers respectively. These technologies became indispensable tools in prototyping workshops. Another class of AM related to the production of ceramic parts. The common method of Stereolithography (SLA) requires a special paste with a mixture of binder and ceramic particles [33]. As a result of consolidation, a green part will be obtained that requires additional operations such as debinding and sintering. Finally, the most applicable AM technologies for metals are direct metal deposition (DMD), electron beam melting (EBM), and laser powder bed fusion (LPBF). All technologies require atomized metal powder with different fractions. For the DMD process powder is supplied from the hopper through the nozzle with a carrier gas directly to the place where it melts by a laser. On the contrary, EBM and LPBF require the formation of a powder bed where an electron beam or a laser beam melts the powder. In this introductory section several disadvantages can be stated to compare AM technologies for metals. Concerning EBM, a special vacuum chamber is required to prevent electron diffraction and dissipation of energy. The resolution factor of DMD is relatively low, and additional machining is often applied. The LPBF process has insufficient performance and cost efficiency for the most of common parts. Thus, each technology has drawbacks and should be wisely applied in industry. As far as nitinol is not a construction material, it is

utilized only due to its functional properties, and the size of most final parts is in the scale of centimeters, the LPBF process is of the highest interest. Further, this technology will be broadly discussed.

1.2.1 Laser Powder Bed Fusion

Laser Powder Bed Fusion (also known as Selective laser melting (SLM)) is an AM technology suitable for manufacturing metal parts with complex geometries with great precision of 100 μm . LPBF is a layer-wise manufacturing technology that requires spherical powder as a raw material. The scheme of the LPBF process (taken from work [34]) is presented in Figure 8. The whole process includes repetitive execution of the following operations. The powder is spread from the supply cylinder (dispenser) onto the building plate attached to the building piston. The excess of the powder after recoating operation is stored in the third reservoir of the installation. The laser selectively melts the powder, providing a metallurgical bonding, and the building plate moves down by a prescribed step. The process is repeated until the entire part is consolidated.

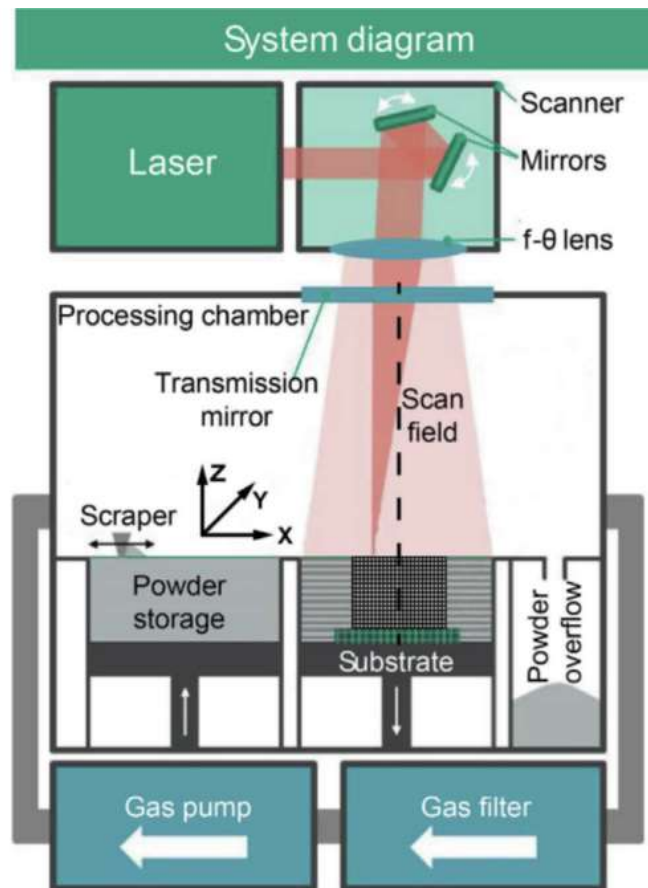


Figure 8. Scheme of LPBF system [34].

A precise laser system provides high accuracy in the manufacturing process. A continuous wave laser with a wavelength of $\sim 1 \mu\text{m}$ is typically used for the LPBF installations. Once the laser beam is focused, it reflects through special mirrors operated by galvo-scanner motors. The mirrors in the scanning head move the laser spot along the building plate area when the F-theta lens provides an optimized focus in the whole scan field. The laser beam enters the airtight camera through a transmission mirror.

A method such as LPBF allows almost unlimited freedom in product shape development. The ability to manufacture almost any geometric shape allows the production of lightweight constructions, topologically optimized parts, structural objects, patient-specific implants, etc. At the same time, a wide area of required research is in demand since such factors as laser irradiation impact, the effect of feedstock material, and the melting regime should be taken into account and carefully considered.

Laser Powder Bed Fusion has opened up new opportunities in the manufacturing of NiTi and overcome the challenges prescribed to conventional approaches [35]. Nevertheless, it should be noted that intermetallic materials such as TiAl, NiAl, NiTi, etc. [36–38] are known to be highly sensitive to the LPBF process parameters therefore optimization and fine-tuning are required for successful consolidation. Many studies have shown that various macro and micro defects can be observed in the printed material [39–43]. Macro defects, primarily caused by the large residual thermal stresses induced by the laser processing with high-temperature gradients include the generation of cracks and delamination from the commercially available base plates. In paper [44] it was demonstrated that preheating of the substrate decreases thermal gradients and preserves crack formation. Micro defects can be subdivided into metallurgical pores, microcracks, and pores caused by a lack of fusion defect [42,43,45,46]. Apart from the abovementioned defects, additional issues related to the LPBF production of nitinol will be discussed further.

1.2.2 LPBF manufacturing of NiTi parts

Different research groups have reported on dense NiTi parts produced via LPBF under different printing conditions, such as laser power, preheating temperature of the substrate, powder fraction, size of the laser spot, etc. [44,47–52]. In this regard, it can be

concluded that the window of possible process conditions can be shifted due to difference in LPBF equipment, raw powders, laser properties, and scanning strategies. It is necessary to develop a suitable approach for optimizing printing parameters. A multi-iteration optimization approach based on printing is straightforward and affordable for widespread and inexpensive materials. However, the above approach is not applicable if it is necessary to obtain the optimal 3D printing conditions for a limited time and a small amount of powder due to the possible high cost of the material. On the other hand, a minimum amount of powder is required to obtain tracks and study the geometry of the melt pool. To date, single-track studies have been performed on materials such as cp-Ti [53], IN625 [54], SS316L[55], Ti6Al4V [56], AlSi10Mg [57], etc. However, comprehensive research dedicated to nitinol has not been reported, despite the high application potential of additively manufactured NiTi parts.

The volumetric energy density (VED) is commonly used to evaluate the energy input from a laser heat source:

$$E_v = \frac{P}{Vht} \quad (2)$$

Where P is laser power, V is the scanning velocity of the laser, h is hatch spacing, and t is the step of the dispenser plate. Despite the prevalence of using Equation (2) to describe the process conditions, VED does not consider factors dependent on the LPBF installation and raw powder. Such parameters are laser beam radius, laser wavelength, the absorptivity of powder, powder size distribution, etc. Different studies showed that the same values of VED do not always result in identical properties of produced parts. Yu Z. [58] reported a difference of 10% relative mass density in samples made with the same VED. However, VED is suitable for energy magnitude evaluation purposes. In such a way it was demonstrated by multiple research groups that NiTi alloy has a relatively narrow window of process parameters. Combined LPBF process conditions reported in the literature are presented in Table 1.

The combination of AM and SMA gives rise to '4D printing', involving consideration of altering the shape and properties over time which gives even new applications of nitinol [59,60]. This field of research will be discussed further.

Table 1. The parameter combinations for the printing of NiTi reported in the literature.

Authors	Powder Composition, % of Ni	Particle size, μm	Laser power, W	Scanning speed, mm/s	Hatch distance, μm	Layer thickness, μm	VED, J/mm^3
Xu et al. [58]	50.7 at. %	36.9	150, 200, 250, 300, 350	1200	50	30	83, 111, 139, 167, 194
Shi et al. [61]	55.92 wt. %	15-53	86.4, ..., 153.6	448, ..., 952	63.2, ..., 96.8	30	31.25, ..., 180.83
Feng et al. [62]	50.9 at. %	15-53	120	800	50, 80, 110, 140, 170	30	29.41, ..., 100
Yu et al. [63]	55.8 wt. %	13-53	199.673 90.978	1357.861 413.671	91.5 120	30	53.57 61.09
Guo et al. [64]	50.2 at. %	15-53	125	600	80	30	86.81
Luo et al. [65]	50.3 at. %	33	150, 210, 270	1200	80	30	52.08, ..., 93.75
Wang et al. [66]	55.64 wt. %	15-53	60, 80, ..., 200	600	80	30	41, 55, ..., 139
Wang et al. [66]	55.64 wt. %	15-53	120	800	40, 50, ..., 110	30	125, ..., 45
Wang et al. [66]	55.64 wt. %	15-53	120	400, 500, ..., 1200	80	30	125, ..., 41
Yang et al. [67]	59.68 wt. %	-	60 (0, 5, ..., 95)	440	110	25	49.59 (0, ..., 78.51)
Xiong et al. [52]	50.4 at. %	15-53	120	500	80	30	100
Zhao et al. [68]	50 at. %	47	100-200	83.3-666.6	80	40	62.5, ..., 750.3
Saedi et al. [69]	50.8 at. %	50	250	1250	120	30	55.5
Saedi et al. [17]	50.8 at. %	25-75	250	1250	120	30	55.5
Moghaddam et al. [70]	50.09 at. %	25-75	250	1250	120	30	55.5
Hamilton et al. [71]	50.9 at. %	18.5	50	80	35, 120	30	173.61, 595.24
Ma et al. [72]	55.7 wt. %	25-45	40, 75, 100, ..., 250	160, ..., 1042	50, ..., 80	30	100, 111
Shishkovsky et al. [44]	55 wt. %	11.4-37.5	50	100, 160	100	60	52.08-83.3
Bormann et al. [74]	56.1 wt. %	D50 = 60	60, 80	171, 133	120	50	60, 70, 84, 100
Dadbakhsh et al. [48]	55.2 wt. %	25-45	40 250	160 1100	60 60	30 30	111 126
Bormann et al. [49]	55.96 wt. %	35-180	56, ..., 100	100, ..., 300	120	50	45, ..., 125
Hoffman et al. [50]	55.96 wt. %	35-75	150	450	120	50	55.56

However, despite all the advantages of the AM approach, LPBF is a complex physicochemical metallurgy process. For successful consolidation, fine-tuning of the process is required due to numerous possible defects. If the energy input is not sufficient during the LPBF process, it will result in low mass density [41,43], mechanical properties [40,75], and poor surface quality [76,77]. If the VED is overestimated it will cause key-hole porosity [45,78], crack generation [79,80], and part buckling due to high residual stresses [81,82]. Additionally, it was found by Haberland et al. that impurity content mainly oxygen and carbon grew with an increase in VED [47].

One of the most important issues in the adaptation of AM to industrial application is understanding of process conditions and properties relationship. Most of the works are dedicated to studying the effect of process parameters on basic mechanical properties such as tensile strength, elongation to fracture, hardness, etc. However, additional properties should be investigated in the case of smart materials 3D printing. As discussed in Section 1.1.2, NiTi alloy may exhibit completely different responses to the external stimuli (load, heating) depending on the TTs. Thus, the relationship of the process condition ~ NiTi functional properties has created a new field for research.

Any domain of material experiences remelting more than once to provide decent metallurgical contact between the adjacent layers. Such a condition causes the appearance of a complex thermal history with multiple cycles of heating/remelting. As far as that influence leads to structural changes, it can be considered as in-situ heat treatment during the LPBF process. In terms of Ni-rich nitinol, excessive Nickel may form precipitation particles, particularly Ni_4Ti_3 once thermodynamically favorable conditions are reached. It is known from pioneer works on the heat treatment and metallurgy of NiTi that the precipitation temperature range can be considered 500 – 1000 K. Complexity of in-situ heat treatment recognition is associated not only with precipitation formation during heating but also with possible dissolving during remelting of the domain.

1.2.3 4D printing concept

The spatial control of TTs by varying the process parameters introduced the 4D printing concept into LPBF manufacturing of nitinol. It was shown by Ma et al. [72] that by changing of hatch distance from 35 μm to 120 μm for different arms of a 3D-printed clamp different stimulus-responses characteristics were achieved in as-built state. It was

demonstrated that strain recovery of an arm manufactured with 120 μm occurs at 60 $^{\circ}\text{C}$ when for the arm obtained with a hatch distance of 35 the shape memory appeared at a temperature of 0 $^{\circ}\text{C}$. It should be noted that other parameters stated in Equation (2) were kept constant. Moreover, it was demonstrated by Moghaddam et al. [83] that hatch distance among other LPBF process parameters has the highest influence on the TTs of the consolidated part. To achieve the superelastic behavior in the as-built state hatch distance was varied from 80 to 180 μm . The sample produced with 80 μm hatch distance resulted in 5.62 % strain recovery and a 98 % recovery ratio with stabilized strain recovery of 5.2 % after 10 loading/unloading cycles.

In conclusion, using the response surface methodology, artificial neural network models like, optimization framework-based models, or machine learning techniques may help tune the TTs of LPBF-printed samples. However, the 4D printing concept has strong limitations in terms of tuning the TTs directly during the LPBF process as far as the optimal window of process parameters for NiTi is quite narrow, and increasing such parameters as the hatch distance may lead to a lack of fusion defects, consequently decreasing the relative density and mechanical properties of the final part.

Apart from the reviewed facts, the mechanism of functional properties altering during the printing of micro-objects with single-track based strategies remains unexplored. Most of the reported findings emphasize the effect of the hatch spacing on the resulting TTs, nevertheless, there have been no studies dedicated to cases when this parameter is not applicable. However, excluding the hatch spacing will shed light on the pure interaction of the main laser influence conditions such as laser power and scanning speed.

1.2.4 LPBF manufacturing of micro-objects

The resolution of the LPBF technology and the limiting factors is an important aspect of the technology, and a significant contribution has been made to this topic. In work [84] Wang et al. formulated rules for manufacturing microporous objects via LPBF. The authors emphasized the importance of taking into account critical inclined angles of overhanging surfaces and adapting a 3D model during slicing to compensate the powder adhesion. The lattice structures with a strut diameter of 300 μm and an inclined angle of 45 $^{\circ}$ were successfully designed and manufactured. Overhanging surfaces with an inclined

angle to the substrate plane of less than 45° are known to be the most important geometric restraint in the LPBF technology. In work [85] authors have demonstrated the optimization procedure of the process parameters for overhanging structures. To prevent possible fabricating defects such as warp or fusion of agglomerates to the surface two methods were proposed: adjusting the part in the building volume and controlling energy density near the overhanging surface. However, the influence of the feature size factor on the critical incline level was not revealed. Yadroitsev et al. [86] carried out a study on the technological regimes for filter element manufacturing with a minimum wall thickness of $120\ \mu\text{m}$ from 316L powder. The authors reported results on parametric analysis of the process parameters for manufacturing thin walls from another grade of austenitic stainless steel Inco 904L using the same equipment. The minimum achieved wall thickness was $140\ \mu\text{m}$ when prescribed 3D model had a $100\ \mu\text{m}$ size. As far as the LPBF resolution is considered, the laser unit and scanning head are known to be the most influential components in the apparatus. Qu et al. [87] reported research on the manufacturing of TPMS structures using a μ LPBF machine with a special scanning head. However, the minimum feature size was set not less than $100\ \mu\text{m}$ despite the possible higher resolution. As was shown by Caprio et al. [88] utilization of pulsed lasers provides a smaller melt pool over the same levels of energy density in comparison with CW lasers which leads to an increase in the width of a single track, as a consequence a decrease in the resolution. Wu et al. in the paper [89] postulated guidelines on the optimization of thin wall manufacturing for LPBF. The authors reported experimental data on the minimum wall thicknesses for the Ti6Al4V, AlSi10Mg, and Inconel 718.

Several works were dedicated to the investigation of the feasibility of printing stents for coronary vessels from Co-Cr [90], titanium [91], steel [92], and NiTi [93], which previously were made using laser cutting methods from hollow tubes [94]. It was demonstrated that resolution, surface finish, and layer bonding dramatically impact the stent performance [90,92,93]. In terms of Nickel-Titanium alloy, both superelasticity and shape memory effect are used for stents to decrease their volume during placement with subsequent extension under temperature influence and to impart a constant load on the walls of the vessel respectively. Furthermore, for intermetallic alloys such as NiTi [4,24,35,45], TiAl [36,37], NiAl [95], etc. application of LPBF technology can remarkably reduce the cost of the parts with complex geometries due to the poor machining of the

material associated with high ductility accompanied by a strongly pronounced strain hardening effect [25].

In terms of comparison between the technologies of traditional laser cutting and LPBF for manufacturing, the following can be stated. The raw material for the LPBF technology can be recycled multiple times which dramatically reduces waste. In the work [96] authors showed that even after the twentieth print the properties of the powder hardly changed and showed high resistance to multiple reuses. The LPBF technology gives rise to a new approach in design through topology optimization [97,98]. The main objective of topology optimization is finding the optimal design or shape of a part by minimizing the desired parameter (i.e. mass) with prescribed constraints. Thus, with the AM approach more ideal design can be built when the design of the final part for laser cutting is constrained by the shape of the blank. Finally, AM provides a straightforward approach to the manufacturing of patient-specific devices [91,99]. However, manufacturing of NiTi micro-objects by LPBF technology cannot be considered an easy task since many requirements are demanded. Resolution factors, an adaptation of design for LPBF, mechanical properties, phase transformation temperatures, and the superelastic response of the material after LPBF, are the main issues for consideration.

It should be noted that a significant increase in LPBF resolution can be achieved by the utilization of powder with micron or even submicron particles, laser optics with a smaller beam diameter, and thinner layer thickness. The combination of those factors gave rise to a new direction in metal AM, namely Micro Laser Powder Bed Fusion (μ LPBF) [100].

1.3 Mesoscale simulation of the melt pool during LPBF

LPBF is a complex metallurgical process with different multiphysical phenomena such as the interaction of a laser beam with powder (i.e., reflection, absorption, scattering), phase transitions in powder and substrate, thermal effects, surface tension effects, convective heat flows, etc. All these phenomena are the result of local remelting of the powder deposited on the substrate due to the absorption of laser energy. For better understanding and prediction of the process outcomes numerical simulations are widely used. Depending on the effect taken into account, the scale of the simulation varies. The

most common problems under consideration at the current state of the art are presented in Table 2.

Table 2. Problems of LPBF simulations and its scales.

Simulation	Problem	Scale
Residual thermal stresses	Thermal-mechanical	Part $\sim 10^{-2}$ – 10^{-1} m
Microstructure	Directional solidification	Grain $\sim 10^{-5}$ – 10^{-3} m
Heat absorption	Ray tracing	Particle $\sim 10^{-6}$ – 10^{-4} m
Temperature distribution	Heat conduction	Melt pool $\sim 10^{-6}$ – 10^{-5} m
Flow behavior	Fluid dynamics	Melt pool flows $\sim 10^{-7}$ – 10^{-6} m

To predict the temperature field during the LPBF process, finite element (FE) modeling is considered a powerful tool. A FE model of the LPBF process considering metal gasification pressure and heat dissipation was proposed in [101]. A model for predicting the penetration depth of the bead into the substrate, and a proposal for a new heat source with consideration of laser reflections, were reported in [102]. The FE model for LPBF, considering the powder layer's shrinkage during the powder-to-solid transition, was established in [103]. Despite these advances in the numerical modeling of the LPBF process, research on the thermal behavior and melt pool formation of nickel–titanium alloy has been presented only for other manufacturing technologies. The authors of [104] studied the melt pool formation in the DMD of pre-alloyed nitinol powder and developed an FE model to investigate the temperature gradient and solidification rate during cladding. The authors of [105] demonstrated wire-arc-based additive manufacturing of NiTi thin-wall structures with laser marking treatment to decrease the melt pool instability and simulated temperature distributions on the titanium substrate during the process. In [106], a FE model of laser welding was used for two nitinol sheets, using Goldak's heat source and a neural network to select the coefficients for the heat source. However, the presence of a powder bed distinguishes the LPBF process from laser welding and greatly affects the results of modeling. Thus, high-fidelity simulations of NiTi melt pool formation during LPBF are still limited at the present state of the art.

1.4 Applications of SMA

The choice of material for a specific application is always a complex problem that is connected with materials science, engineering, solid mechanics, and economics. One of

the well-established techniques for material selection is the Ashby approach [107]. The method is based on the calculation of the performance indices with respect to the material function, the optimization objective, and environmental constraints [108]. In comparison with common materials, smart materials are primarily utilized due to their functional properties. Thus, in the case of SMA selection, it is necessary to take into account the phase transformation temperature, the specific work released during the phase transition, the maximum reversible deformation, thermal hysteresis, etc.

As was mentioned in Section 1.1.5, the SMAs of Ni-Ti system have transformation in a relatively low temperature range from -60 to +80 °C. Applications with requirements of higher activation temperatures have stimulated the development of new high-temperature shape memory alloys (HTSMAs). All HTSMAs were divided into 3 groups according to the transformation temperatures, namely, group I with a range of 100 – 400 °C, group II had a 400 – 700 °C range, and group III with the highest possible temperatures above 700 °C [109]. Group I of HTSMA has the highest diversification of alloys: NiTi-based (NiTiHf, NiTiZr), copper-based (CuAlNi, CuAlNb), nickel-based (NiAl, NiMn), titanium-based (TiNb), and uranium (UNb) [110]. However, only NiTiPd and NiTiPt have a high recovery, superelasticity, and the most commercial readiness and the present state of the art. Group II involves TiPd and TiAu alloys, both containing high-cost raw materials and utilized only in special applications. Group III of HTSMA (TiPtIr, TaRu, NbRu) is mostly in the research state with unsolved problems related to oxidation and microstructural stability.

NiTi SMAs play a special role due to the combination of the following properties. High mechanical properties, excellent wear and corrosion resistance along with the shape memory effect of NiTi alloys predetermine their applications for a wide range of engineering and biomedical devices [25,111–115]. The combination of the shape memory effect, pseudoelasticity, and impressive possibilities of structure design due to additive manufacturing methods promises a wide area for further research concerning nitinol materials, allowing for new approaches and applications [112]. Depending on the application certain functional properties of NiTi will be of interest. The biocompatibility of these alloys expands the application area to medicine as bone implants and various types of medical instruments [116,117].

1.5 Thesis objectives

The present thesis aims to develop physical mechanisms of change in material properties of nitinol under the laser influence during high-resolution Laser Powder Bed Fusion based on an original single track scanning strategy. Furthermore, the thesis expands the existing knowledge about the technology for manufacturing micro devices made of intermetallic NiTi alloy. The following objectives are stated in this work:

- 1) Carry out experiments on the melt pool characterization of nitinol during LPBF,
- 2) Experimentally obtain data on the thermophysical properties of NiTi required for high-fidelity LPBF simulations,
- 3) Experimentally obtain data on the mechanical properties, TTs, SME, thickness, phase composition of single-track based thin walls,
- 4) Carry out simulations of the melt pool with validation using the obtained experimental data,
- 5) Carry out simulations of single-track based thin walls for investigation of functional properties altering over the different regimes of laser influence,
- 6) Achieve suitable LPBF resolution for SAF manufacturing from NiTi powder,
- 7) Characterize obtained SAF and carry out simulation of the SAF consolidation process.

Chapter 2. Materials and methodology

This chapter covers methodology used in the present research. The chapter is divided into three parts: 1) raw powder analysis and manufacturing of samples, 2) characterization methods applied onto obtained samples, and 3) physical model used for the numerical study of the LPBF process. First two parts are related to experimental work when the last corresponding to the description of simulation procedures.

2.1 Materials and equipment

2.1.1 Powder analysis

The NiTi powder with a Ni content of 55.9 wt.% was produced by NiTiMet Co., Ltd. (Moscow, Russia). The powder was obtained by the electrode induction-melting gas atomization (EIGA) technique. Oxygen content of 0.03 wt. % was measured by the inert gas fusion method.

The morphology and chemical composition of particles were studied using a Scanning Electron Microscope (SEM) Quattro S (Thermo Fisher Scientific, Waltham, MA, USA). Elemental analysis and mapping of the obtained samples were performed with Quantax XFlash 6 (Bruker, Billerica, MA, USA) energy dispersive analysis (EDX) attachment. Powder flowability was measured as the time required for 100 g of powder to flow through a standardized 4 mm diameter Hall funnel.

The laser diffraction method was employed for the particle size analysis. The raw powder was investigated with Analysette 22 (Fritsch, Germany). NiTi powder was distributed in solution with surface-active substance and continuously supplied to the device.

2.1.2 LPBF installation

The experiments were performed on TruPrint 1000 (Trumpf, Germany) LPBF machine equipped with a CW ytterbium fiber laser (wavelength of 1070 nm). The laser beam profile yielded Gaussian power density distribution (TEM₀₀), with a spot size diameter of 55 μm and a maximum laser power of 200 W. The chamber was filled with argon to prevent the nitinol samples from assimilating hydrogen, nitrogen, and oxygen; the

oxygen content in the chamber was less than 0.01%. A NiTi sheet with a thickness of 4 mm was used for an in-house built substrate. Macro defects, primarily caused by large residual thermal stresses induced by laser processing with high-temperature gradients include the generation of cracks and delamination from the commercially available base plates. It is noted that sufficient bonding and metallurgical contact has not been achieved with any commercially available building plates. It has been demonstrated that the utilization of a titanium substrate leads to delamination due to the formation of a brittle Ti_2Ni phase in the NiTi/Ti interface [118]. Therefore, a nitinol base plate was adopted to guarantee the necessary bonding for consolidation.

The data files for Trumpf 1000 installation were prepared with Materialise Magics slicing software (Materialise, Belgium). All single track-based objects were made from a triangulated planes by assigning such part as a support to a dummy part.

2.2 Characterization methods

2.2.1 Differential scanning calorimetry

DSC measurements were carried out on the 823E Module (Mettler Toledo, Switzerland) with a liquid nitrogen cooling system. Melting points and enthalpies of indium and zinc were used for the temperature and heat capacity calibration.

Samples weighing 8–10 mg were cut from the central part of the plate and placed in 40 μ L aluminum pans. Calorimetry was performed in the range from $-100^{\circ}C$ to $100^{\circ}C$ with a rate of $10^{\circ}/min$ under an argon atmosphere. Before the actual cycle, the samples were heated up to $100^{\circ}C$ to ensure a fully austenitic phase at the start of measurements.

2.2.2 Microstructural studies

The samples were mounted in resin and polished using TechPress and MetPrep (Allied, East Rancho Dominguez, CA, USA) equipment. To visualize the contrast, the samples were slightly etched with an acidic solution of $HF + HNO_3 + H_2O$ in the following proportions: 5% + 15% + 80%, respectively. The same Scanning Electron Microscope Quattro S was utilized as in Section 2.1.1.

2.2.3 *X-Ray diffraction analysis*

The phase composition was investigated via X-ray diffraction (XRD) analysis using the Difrey 401 diffractometer (Scientific Instruments, Russia). The measurements were carried out at room temperature using an X-ray tube with Cu-K α radiation (wavelength 0.1504 nm), and Bragg-Brentano focusing. The phase composition of the samples was identified using the 1999 PDF2 X-ray database and BaseDiffract (ver. 2.01).

2.2.4 *Mechanical tests*

Mechanical tests were performed on a dual-column testing system 5969 (Instron, England). A static load cell with a capacity of 1 kN was chosen to increase the accuracy of load measurements. Pneumatic side action tensile grips with a maximum load of 2 kN were utilized with rough jaw faces. The methods for static analysis were designed with Bluehill universal testing software. All tests were run at room temperature of 23 °C with a strain rate of 0.5 mm/min. A Digital Image Correlation (DIC) system with two high-resolution cameras was used. Plates were painted to ensure sufficient quality of speckle pattern on the plates. The frames were captured at each increase in the load by 100 N or every 3 seconds resulting in 500 – 1000 points. The analysis was performed in the Vic 3D software (Correlated Solutions, USA).

2.2.5 *Pendant drop tensiometry*

Pendant drop tensiometry was performed in a modified vacuum furnace. The experiments were carried out in a 10⁻³ Pa vacuum near the melting point (1330 °C). NiTi powder (described in Section 3.1) was used as the raw material for the melt formation. The drop of melt was formed in a graphite dropper with a needle diameter of 0.4 mm. For the surface tension measurements, the liquid was slowly squeezed until the pendant drop reached a critical size with a subsequent fixation on a high-speed SSD camera CP70-2-M/C-1000 (Optronis, Germany). To control the temperature of the melt a thermal camera PI 1M (Optris, Germany) was used. A detailed description of the setup is presented in the work [119]. The profile of the pendant drop was fitted with the DropShape software (Open Science Ltd., Russia).

Solidified NiTi melt in the graphite dropper was cut and mounted into the resin, ground, and polished. The NiTi – graphite interface was investigated using Tescan Vega 3 SEM with EDS detector.

2.3 Simulation procedure

KiSSAM (Kintech Simulation Software for Additive Manufacturing) was developed and implemented by members of Kintech Lab LLC (Russia). A more detailed description of the solver can be found in the paper [120]. The present section intends to highlight the basic methods and equations that are solved during the simulation. The results of the dissertation assisted in the multicomponent evaporation model implementation (Section 4.6). All rights to KiSSAM Solver belong to Kintech Lab.

The software is designed for high-performance and high-fidelity modeling of metal powder bed fusion (PBF) additive manufacturing processes at the mesoscale level. The software utilizes a high-performance code implemented on the CUDA GPU, allowing for fast simulations on NVidia GPU workstations. Simulation of a few millimeters' laser track corresponding to 1-2 hours of calculations on a workstation.

The main part of KiSSAM is a hydrodynamic solver based on the Boltzmann Thermal Lattice Method. It incorporates Volume of Fluid free surface tracking and phase transition between solid and liquid states. Several important phenomena are taken into account during the simulation:

1. Surface tension of liquid in the melt pool and wetting of the powder/substrate by the melt. For the surface tension, a value at the melting point and a temperature coefficient are introduced as input parameters,
2. Marangoni convection due to the temperature gradient,
3. Recoil pressure and mass losses during evaporation,
4. Energy deposition by ray tracing with multiple reflections of the laser beam.

Heat transfer is modeled across the entire simulation domain considering conduction, radiation, convection in the melt pool, and evaporation from the surface of the liquid.

A simulation starts with specifications of the substrate, the powder, and the heat source (power and scanning speed for the laser beam). The laser beam melts the powder or

substrate, and the software calculates the fluid dynamics inside the melt pool, temperature distributions in the liquid and solid. Various diagnostics of solidified melt geometry, temperature history, and other parameters can be obtained.

Solid and liquid phases are modeled with the Volume of Fluid method. In a rectangular grid, the material distribution is characterized with filling fraction φ such that:

$\varphi = 1$ Solid cell,

$0 < \varphi < 1$ Interface cell,

$\varphi = 0$ Void cell.

The surface of the metal is an isosurface $\varphi = 0.5$. A material heated above the melting temperature transforms to fluid. In the fluid material, fluid dynamics are calculated with the Lattice Boltzmann Method (LBM). In LBM, the fluid motion is described with streaming and collision of discrete particle distribution functions (PDF). Fluid density and velocity are found as weighted sums of PDFs. When fluid cools near the solidus temperature, it solidifies. Solid material contains identifiers (ID) with the type of solid: substrate, powder, or solidified melt.

Boundary conditions are implemented for PDFs that come from void cells. Curvature is estimated from the filling fraction, and Laplace pressure is included. The temperature gradients generate the Marangoni convection, which is included as a tangential force on the surface. Evaporation is modeled, and the recoil pressure is included.

Ray tracing is implemented for the laser beam. The surface normal is estimated, and the reflection is calculated. The absorption coefficient controls energy deposition.

Heat transfer is modeled with a second distribution function in LBM. The heat transfer is modeled in fluid, interface, and solid cells. On the material/void surface radiation heat loss is implemented. Convective cooling is implemented with the Whitaker model.

2.3.1 *Fluid dynamics in the melt pool*

For the simulation, three types of grids are used: Melt pool Grid, Global Geometry Grid, and Tractile Mesh. The melt pool Grid is the smallest grid which covers the melt pool region only. The melt pool is always enclosed by the rectangular melt pool grid. In the simulation, the computational contains cubic cells with size of $\Delta r \times \Delta r \times \Delta r$ each. The grid is adaptive, and it follows the liquid melt domain (Melt pool Grid) and is divided into equal

cubic cells with $\Delta x = \Delta y = \Delta z = \Delta r$. Each cell has a type that defines its phase: Solid, Fluid, or Void. Some Fluid cells can be also Interface sub-type. Interface cells separate Fluid and Void cells and guarantee they cannot be adjacent.

In each Fluid and Interface cell, the lattice Boltzmann equation (LBE) is solved for a discrete set of distribution functions (DFs) f_i . The LBM with the D3Q27 model and single-relaxation time BGK scheme used as in [121]:

$$f_i(\vec{x} + \vec{c}_i \Delta t, t + \Delta t) = f_i(\vec{x}, t) - \frac{f_i(\vec{x}, t) - f_i^{eq}(\rho, \vec{u})}{\tau_f} \quad (3)$$

The equilibrium distribution is given by Equation (4) in the polynomial form.

$$f_i^{eq}(\rho, \vec{u}) = \omega_i \rho \left(1 + \frac{\vec{c}_i \vec{u}}{c_s^2} + \frac{(\vec{c}_i \vec{u})^2 \vec{x}_i}{2c_s^4} - \frac{\vec{u} \vec{u}}{2c_s^2} \right) \quad (4)$$

where the mass density $\rho(\vec{x}, t)$ and momentum density $\rho(\vec{x}, t) \vec{u}(\vec{x}, t)$ from Equation (4) are as follows:

$$\rho(\vec{x}, t) = \sum_i f_i \quad (5)$$

$$\rho(\vec{x}, t) \vec{u}(\vec{x}, t) = \sum_i \vec{c}_i f_i \quad (6)$$

where ω_i are the constant weights defined in the LBM, $c_s^2 = c^2/3$, with $c = \Delta x / \Delta t$ is the lattice step, and the fluid viscosity is $\mu = \frac{\tau_f - 1/2}{3}$. In the dimensionless units, $\Delta x = \Delta t = 1$, $c_s^2 = 1/3$, and the value of μ gives the unit conversions system.

The basic LBM algorithm consists of two steps, corresponding to the first and second terms in (3). The streaming step copies each DF f_i from one cell to its neighbor in the \vec{c}_i direction. The collision step locally computes the macro variables and updates f_i .

2.3.2 Heat conduction

The governing equation for heat transfer and energy distribution in the enthalpy formulation is given in Equation (10). The double distribution approach is implemented for solid and fluid cells, consequently, 27 LBEs are solved additionally.

$$h_i(\vec{x} + \vec{c}_i \Delta t, t + \Delta t) = h_i(\vec{x}, t) - \frac{h_i(\vec{x}, t) - h_i^{eq}(\rho, \vec{u})}{\tau_h} + Q_i \quad (7)$$

where Q_i is the source term and the equilibrium distribution is

$$h_i^{ea}(\rho, \vec{u}) = \omega_i H \left(1 + \frac{\vec{c}_i \vec{u}}{c_s^2} + \frac{(\vec{c}_i \vec{u})^2 \vec{x}_i}{2c_s^4} - \frac{\vec{u} \vec{u}}{2c_s^2} \right) \quad (8)$$

where $H = \sum_i h_i$ is the local energy density when thermal diffusivity is $k = \frac{\tau_h - 1/2}{3}$.

$$H(T) = \begin{cases} E_s & \text{if } T \leq T_s \\ E_s + L_f \frac{T - T_s}{T_l - T_s} & \text{if } T_s < T \leq T_l \\ E_s + L + E_l & \text{if } T > T_l \end{cases} \quad (9)$$

The heat conduction Equation (10) is used for the solid domain:

$$\frac{\partial H(T)}{\partial t} = \nabla(\alpha(T)H(T)) \quad (10)$$

where $\alpha(T)$ is the temperature dependence of thermal diffusivity coupled with thermal conductivity by the expression: $\alpha(T) = \frac{k(T)}{\rho c_p(T)}$. According to experimental data, the density of NiTi alloy has a weak temperature dependence [122], therefore, the density of a solid and a liquid without its temperature dependence is taken into account for simulation.

The mesh in the domain around the melt pool is adaptive. Cells in the mesh with coordinates (x_1, y, z) and (x_2, y, z) can be merged if the maximum temperature difference between cells (x_1, y_a, z_a) and (x_2, y_a, z_a) for any y_a, z_a is less than 10 K. The cell is split if the temperature difference between neighboring cells is higher than 10 K. The same criteria were introduced for all coordinates.

2.3.3 Marangoni effect

High-temperature gradients along the liquid metal surface lead to Marangoni convection. The surface tension stabilizes the liquid metal surface, while the Marangoni effect and the gasification recoil force cause the liquid metal surface to appear concave. The difference between the Marangoni effect and the gasification recoil force is that the tangential movement of the liquid metal surface caused by the Marangoni effect causes the molten metal in the central region to accumulate, forming a liquid surface morphology that resembles a crater. This tangential Marangoni force acts along the surface tension gradient, and the following Equation (11) should be satisfied for the force \vec{F} :

$$\vec{F} \vec{\tau} = \nabla(\gamma(\vec{x}, T)) \vec{\tau} \cdot \Delta S \quad (11)$$

where $\vec{\tau}$ is the unit tangential vector, $\gamma(\vec{x}, T)$ is the temperature-dependent surface tension, and ΔS is the unit surface area that is equal to 1 in the arbitrary units. It should be noted that the recoil pressure and the Laplace pressure are included in the pressure drop at the fluid/gas interface boundary condition, while the Marangoni effect acts as a shear force. The force \vec{F} for Equation (12) is given as follows:

$$\vec{F}(\vec{x}) = \nabla(\gamma(\vec{x}, T)) - (\nabla(\gamma(\vec{x}, T)) \cdot \vec{n})\vec{n} \quad (12)$$

where \vec{n} is the unit normal vector and the surface tension gradient $\nabla\gamma$ is calculated with a finite difference scheme.

2.3.4 Evaporation solver

The evaporation solver follows the Knight [123] and Klassen [124] evaporation models to estimate the energy loss due to vaporization, the force generated by recoil pressure, and the mass carried away by the vapor. In this model, the additional pressure P_v , mass loss M_v , and energy loss J_v are introduced at the surface of the fluid with temperature T_{surf} :

$$P_v = \max\left(\frac{P_{sat}(T_{surf})}{2}\left(1 + \frac{1 - \psi}{2}\left(1 + \frac{\rho_{Kn}}{\rho_{surf}}\frac{T_{Kn}}{T_{surf}}\right)\right) - P_{atm}, 0\right) \quad (13)$$

where ψ is the evaporation coefficient, ρ_{surf} and ρ_{Kn} are the vapor density near the surface and across the Knudsen layer, T_{Kn} and T_{surf} are the temperatures of vapor on the surface of the fluid domain and across the Knudsen layer. P_{sat} is the saturated pressure of vapor and P_{atm} is the atmospheric pressure. The energy loss J_v during vaporization is given by Equation (14):

$$J_v = M_v(L_{vap}(T_{surf}) + E(T_{surf})/\rho) \quad (14)$$

where $L^{vap}(T)$ is the latent heat of vaporization, $E(T)/\rho$ is enthalpy density at temperature T (see Equation (9)). Mass loss M_v is defined from the jet j as follows:

$$M_v = -\psi j \cdot \Delta t \Delta x^2 \quad (15)$$

where Δt and Δx are space and time steps (equals to 1 in LBM units). The jet j and the evaporation coefficient are given by Equations (16) and (17) respectively:

$$j = P_{sat}(T_{surf})\left(\frac{m_a}{2\pi k_B T_{surf}}\right)^{1/2} \quad (16)$$

$$\psi = (2\pi\xi)^{1/2} M \frac{\rho_{Kn}}{\rho_{surf}} \left(\frac{T_{Kn}}{T_{surf}} \right)^{1/2} \quad (17)$$

where m_a is the vapor atomic mass, and k_B is the Boltzmann constant. The ratio of $\frac{\rho_{Kn}}{\rho_{surf}}$

and $\left(\frac{T_{Kn}}{T_{surf}} \right)^{1/2}$ calculated as follows:

$$\left(\frac{T_{Kn}}{T_{surf}} \right)^{1/2} = \left(1 + \pi \left(\frac{(\xi - 1)M_{Kn}}{2(\xi + 1)} \right)^2 \right)^{1/2} - \frac{\sqrt{\pi}(\xi - 1)M_{Kn}}{2(\xi + 1)} \quad (18)$$

$$\begin{aligned} \frac{\rho_{Kn}}{\rho_{surf}} = \left(\frac{T_{Kn}}{T_{surf}} \right)^{1/2} & \left(\frac{1}{2} (M_{Kn}^2 + 1) \exp(M_{Kn}^2) \operatorname{erfc}(M_{Kn}) - \frac{M_{Kn}}{\sqrt{\pi}} \right) \\ & + \frac{T_{surf}}{2T_{Kn}} \left(1 - \sqrt{\pi} M_{Kn} \exp(M_{Kn}^2) \operatorname{erfc}(M_{Kn}) \right) \end{aligned} \quad (19)$$

M is the Mach number for evaporated material near the surface, $M_{Kn} = M \sqrt{\frac{\xi}{2}}$, and ξ is the vapor adiabatic index (monoatomic with $\xi = 5/3$ in the case of NiTi).

The temperature dependence of the saturated vapor pressure is calculated with the Antoine equation [125] given by (20). The approximation provides not less than 5 % accuracy for the calculation of saturated pressure for pure components.

$$\log_{10} P^{sat}(T) = A - \frac{B}{T} \quad (20)$$

$$L^{vap} = \frac{B}{T} \quad (21)$$

Both coefficients for Ni and Ti can be found in Table 7. Both equations (20) and (21) are given in a simplified form as the other coefficients of Antoine equations are zero for Ni and Ti components.

Chapter 3. Manufacturing of NiTi via Laser Powder Bed Fusion

3.1 NiTi powder characteristics

In various works devoted to LPBF technology, it has been shown that a well-chosen initial powder material is the basis for successful consolidation with minimum defects [41,126–129]. The most important properties of the powder are particle morphology, chemical composition, and microstructure [126]. In terms of high-resolution manufacturing, these factors will be fundamental for achieving repeatability. Thus, the initial powder was studied by laser particle sizer, SEM with EDS detector, and Hall funnel (Section 2.1.1).

The results of the granulometric analysis are presented in Figure 9 as a histogram with an unimodal normal distribution. The found percentiles of the equivalent diameter are $d_{10} = 15.1 \mu\text{m}$; $d_{50} = 27.8 \mu\text{m}$; $d_{90} = 45.0 \mu\text{m}$. The Particle Size Distribution (PSD) fits the 15-45 μm fraction which is optimal for the LPBF process. The width of the PSD is characterized by a standard deviation near the mean value or span given in Equation (22):

$$\text{span} = \frac{d_{90} - d_{10}}{d_{50}} = 1.076 \quad (22)$$

For the LPBF process, the finer particle content and span value play an important role. A wider PSD will increase the theoretical density of the powder as far as finer particles will fill the voids of the granular material, however, a high content of finer particles will deteriorate flowability due to the formation of agglomerates and increased inter-particle friction [130]. During recoating operation, the homogeneity of the powder bed is directly affected by the flowability of the powder while inhomogeneity may lead to a lack of fusion defect when regimes with low energy input are applied [131]. The density and consequently thermal conductivity of the powder bed are dependent on the span value [132]. The optimal span value (~ 1) will result in dense packaging and a higher tap density of the powder bed promoting densification without the balling effect that occurs due to the Plateau-Rayleigh capillary instability [102].

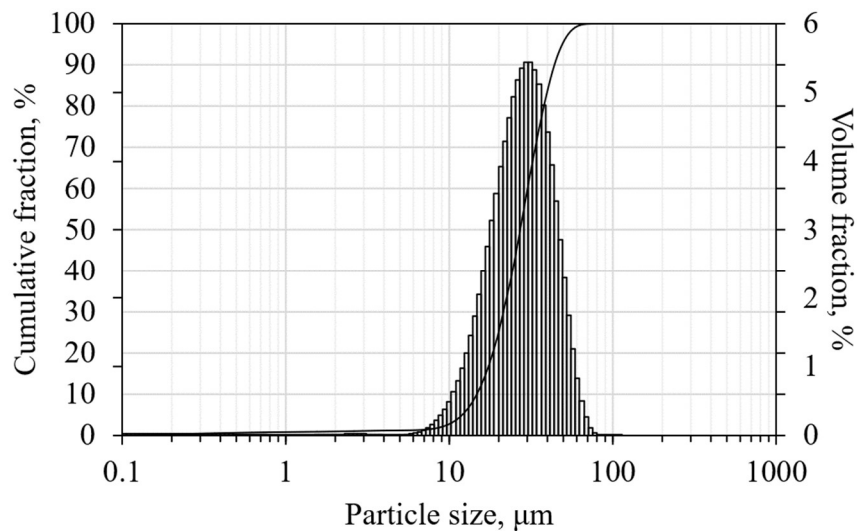


Figure 9. Particle size distribution histogram with cumulative curve.

The morphology and sphericity of the powder particles were characterized using SEM and powder particles shown in Figure 10a. The microstructure of the powder is represented by micro dendrites (Figure 10b) inherent to the Electrode Induction-melting Gas Atomization (EIGA) method. The results of EDS analysis correspond to the Ni-rich chemical composition of the powder and prove the uniform distribution of the elements in each particle, as demonstrated in Figure 10c, d.

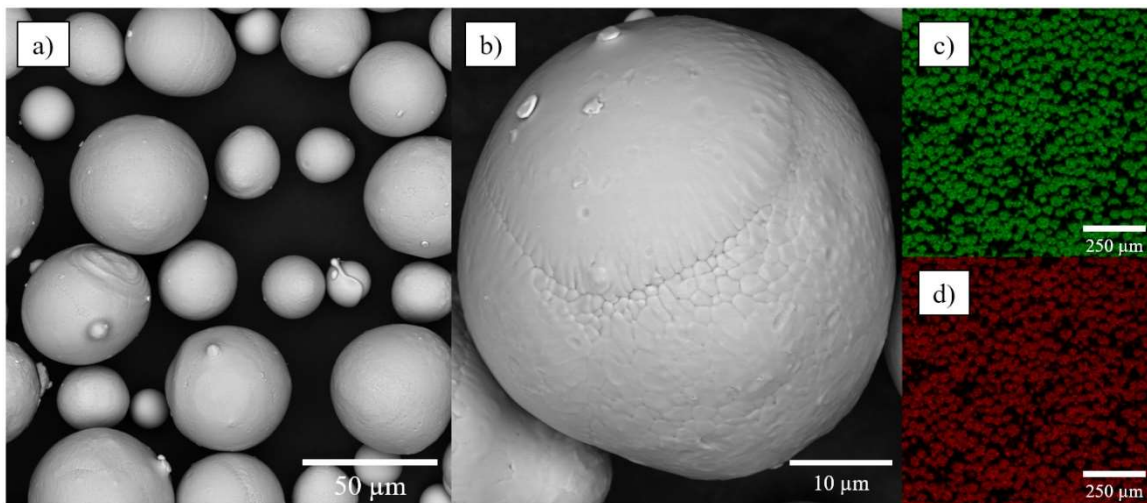


Figure 10. Results of the SEM powder analysis: a) SEM image of powder; b) powder particle with dendritic fragments under high magnification; c) Ni K α 1; d) Ti K α 1.

As was discussed in Section 1.1.5, a slight difference in chemical composition significantly affects the functional properties of the final parts due to the dependence of TTs on the Ni content. In this regard, additional measurements of the elemental weight ratio were performed with inductively coupled plasma mass spectrometry (ICP-MS), since

EDS accuracy is limited. The chemical composition was found to be 55.9/44.1 wt.% (Ni/Ti). It should be noted that the window of process parameters or the melting regime was not considerably affected by the chemical composition as was demonstrated by Xue et al. [133]. The authors studied two powders with 50.8 and 50.1 at. % of Ni which are often used in industrial applications.

The measured time required to flow 100 g of powder through the Hall funnel was 38.1 ± 1.1 s. Relatively high flowability characteristics of the powder are explained with a mean sphericity of 0.91, unimodal PSD, and optimal span. The “satellite” defect represented by smaller particles attached to the surface of the larger ones took place but was not pronounced.

3.2 Single track analysis

The substrate was lowered by 50 μm ; then it was filled with powder via a recoating cycle without changing its z position. Extra powder feeding was applied to ensure complete coverage of the substrate with powder, as well as homogeneous powder distribution on the surface. The obtained powder layer was scanned with the laser according to the prepared executive file, resulting in single tracks. The set of parameters chosen for this study is presented in Table 3.

Table 3. The combinations of parameters used in the experiments.

Laser Power (W)		Scanning Speed (mm/s)				
50	450	350	300	200	150	100
77	600	550	450	350	250	150
100	900	700	600	400	300	200
150	1350	1150	900	600	450	300

After the LPBF procedure, the single tracks with the substrate were cut with a GX-320L electrical discharge machine (CHMER EDM, Taichung, China) to obtain cross-sections of printed single tracks. For each combination of parameters, four unique locations of every single track were examined. All samples were studied with an Axioscope A1 optical microscope (Zeiss, Oberkochen, Germany) at the next stage.

Investigation of the optimal combination of process parameters is crucial for manufacturing high-quality parts using LPBF. Linear energy density E_l , as given by Equation (23), was used for the evaluation of energy input during a single laser scan.

$$E_l = \frac{P}{V} \quad (23)$$

where P is the laser power and V is the scanning speed.

A common single-track deposit cross-section is presented in Figure 11a. The primary geometric parameters of the melt pool are depth, width, and depth-to-width aspect ratio [56]. These parameters are strongly dependent on the process conditions and linear energy density. Insufficient penetration depth could result in poor metallurgical contact of the deposit with the substrate (the previous layer), or even lead to no contact at all (Figure 11b). Thus, the solidified bead could be displaced by the recoating blade during the formation of the next powder layer, leading to disturbance of the layer-by-layer consolidation. On the other hand, an excessive depth of the melt pool leads to the appearance of a keyhole defect. During the melting of the powder by a laser beam, intense convective flows occur in the melt pool due to the Marangoni effect: the surface tension gradient caused by a temperature gradient creates a flow from the center of the melt pool with higher temperature to its edges. Gas bubbles can be captured in the melt pool during the convection mixing of the liquid phase; the probability of their ejection decreases with an increase in the depth of the melt pool since the lifetime of the liquid phase is in milliseconds. The micrograph of the longitudinal cross-section with pores caused by this phenomenon is presented in Figure 11c.

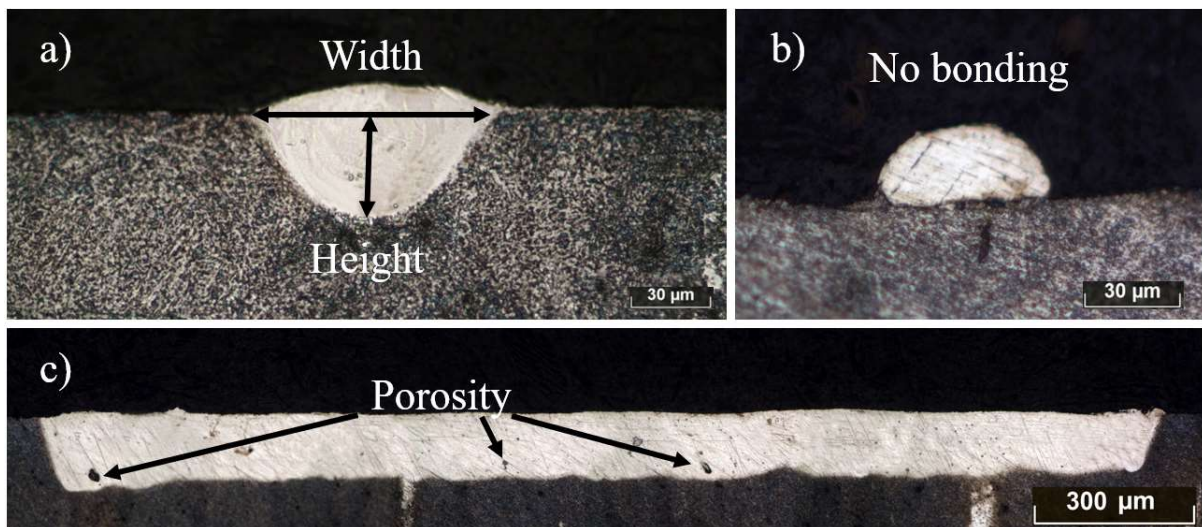


Figure 11. Cross-sections of NiTi single-track deposits: (a) common shape of the melt pool for the LPBF process; (b) no bonding defect; (c) appearance of the pores during keyhole mode in the longitudinal cross-section.

3.2.1 Width of the melt pool

The dependence of the melt pool dimensions for different E_l levels was observed using various combinations of laser powers and scanning speeds. Top-view micrographs of the single tracks (Figure 12) provide information on the single tracks' morphology and width. Images presented on the same scale clearly show that with a decrease in scanning speed, the width of the single tracks increased.

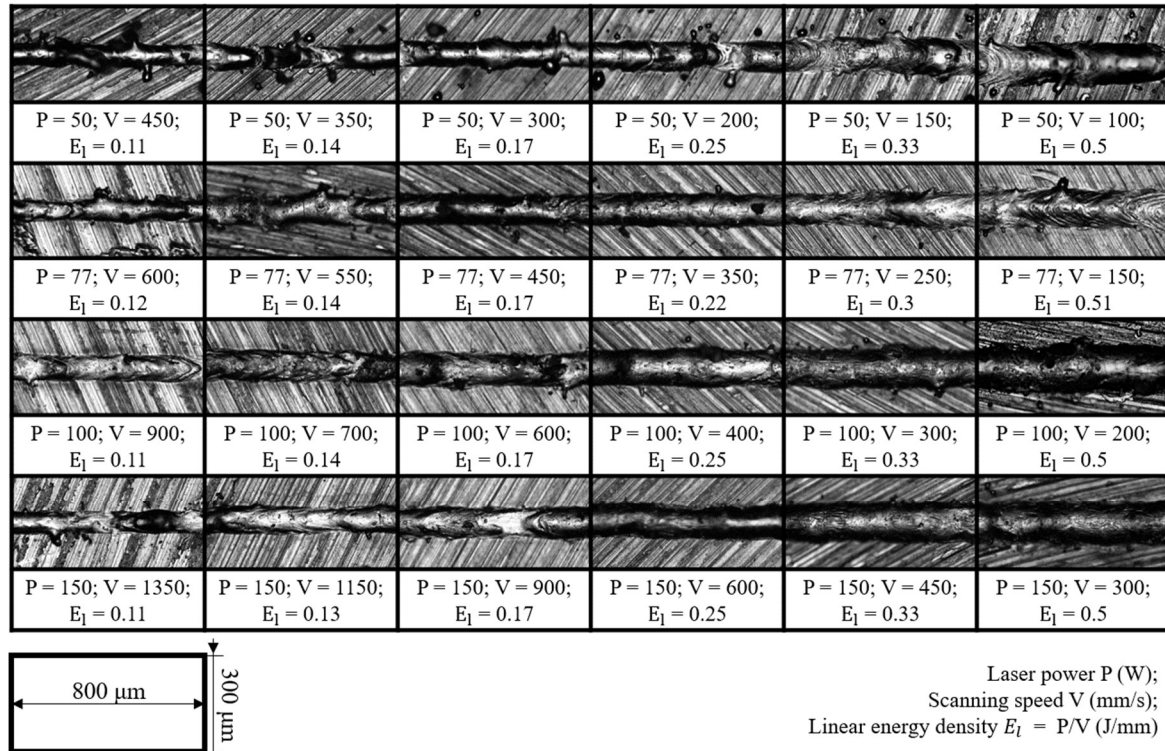


Figure 12. Micrographs of the single tracks' top view.

The single tracks made with laser powers from 77 W to 150 W and an E_l greater than 0.17 showed the most stable and continuous weld beads. The single track deposits obtained with a laser power of 50 W demonstrated humping behavior, and some unmelted powder particles attached to the beads could also be observed. In the case of higher speeds for all levels of laser power, the single tracks' morphology resulted in wavy cylinders due to the Plateau–Rayleigh capillary instability phenomenon, as shown in [102]. With a further increase in scanning speed, the single track beads become discontinuous, commonly known as a balling effect [134]; however, in the chosen range of scanning speeds, such defects were not observed. Additionally, the surface roughness of the final part is greatly affected by the morphology of the single tracks. With an increase in linear energy density,

the growth of the above-surface layer was observed. The excessive height of the beads complicates the formation of a homogeneous powder bed at the subsequent layers; as a result, tracks with a large above-surface layer will be remelted many times, increasing the curvature of the surface. In [135], the authors showed that both discontinuity and overheating of single tracks led to an increase in the surface roughness of the final parts.

With increasing laser power, an increase in the width of the single tracks was observed for the same levels of linear energy density. The smallest width of 58 μm was observed at $P = 50 \text{ W}$ and $V = 450 \text{ mm/s}$, which is close to the laser beam diameter. The regimes with the highest E_l level of 0.5 J/mm resulted in a significant expansion in the melt pool dimensions, up to three times the laser spot diameter. Measurements of the single beads' width are essential before printing 3D objects, in order to avoid multiple remelting of the same powder volume and guarantee the necessary overlap between adjacent tracks. Such an analysis was presented for NiTi intermetallic powder in [43,47,136], where Realizer SLM 100 (SLM Solutions, Germany), Aconity3D Midi (Aconity3D, Germany), and Phenix PXM (now 3D Systems, USA) installations were used, respectively, all with a laser spot size of 80 μm . The reported results of the single tracks' width measurements show the same tendencies; however, the values are higher than those obtained in this work. In [136], the width of the melt pool was described with a regression model as a function of laser power and scanning speed. The coefficients in regression Equation (24) are in good agreement with the present study, with a 2–5% difference—except for the laser power factor which is reduced by 23%. The installations used for the experiments had ytterbium fiber lasers yielded a Gaussian power density distribution (TEM00) and a wavelength of 1070 nm. The intermetallic nitinol powders had the same particle size distribution of 25–75 μm . There was a significant difference in the laser spot diameter, which was 55 μm . To take into account the factor of the laser spot size, Equation (25) was proposed. Results from the literature and the experimentally obtained values correlate with the derived equation having a 5% error. Equation (25) can be used for the melt pool width calculation in order to evaluate the correct hatch spacing parameters (from Equation (2)), with consideration of ~20% overlapping between adjacent tracks.

$$\omega = 10^{-6}(0.5727 \cdot P + 32.743)V^{-0.432} \quad (24)$$

$$\omega = 10^{-6}((0.0108 \cdot r_b + 0.1435)P + 32.7)V^{-0.4} \quad (25)$$

where ω is melt pool width (μm), P is laser power (W), V is scanning speed (mm/s), and r_b is laser beam diameter (μm).

3.2.2 *Depth of the melt pool*

During laser welding, the optimal mode is the complete filling of the end surfaces with the liquid phase, i.e., the size of the melt pool is comparable with the size of the joint. On the contrary, for the LPBF process, the appearance of a large melt pool is highly undesirable due to the appearance of a keyhole defect, as described above. With a change in the energy input, the depth and width change, along with the shape itself. From the presented micrographs of the single tracks' cross-sections in Figure 13, the change in the geometry of the melt pool is visible. The bottom edges of the deposits are more spherical in cases of low values of linear energy density, and sharper with higher E_l values. In the case of lower linear energy density, the surface tension forces of the liquid squeeze the surface due to the system's tendency to minimize the surface energy, forming a cylindrical bead with moderate penetration into the substrate. On the other hand, a laser beam with a high laser irradiation intensity and a low scanning speed penetrates the material's depth significantly, increasing the depth-to-width ratio and resulting in a narrow and deep melt pool.

Figure 14 depicts the depth-to-width ratios for the experimentally obtained single tracks as a function of scanning speed for all laser power levels. The investigated regimes were divided into conduction mode and keyhole mode from the cross-sectional images and aspect ratios. The combinations of the process parameters with a laser power of 150 W, 100 W, and 77 W, and scanning speeds less than 600 mm/s, 300 mm/s, and 250 mm/s, respectively, were considered as keyhole mode regimes, with a depth-to-width ratio greater than 1; in the case of a lower aspect ratio, the melt pool formation occurs in a conductive mode.

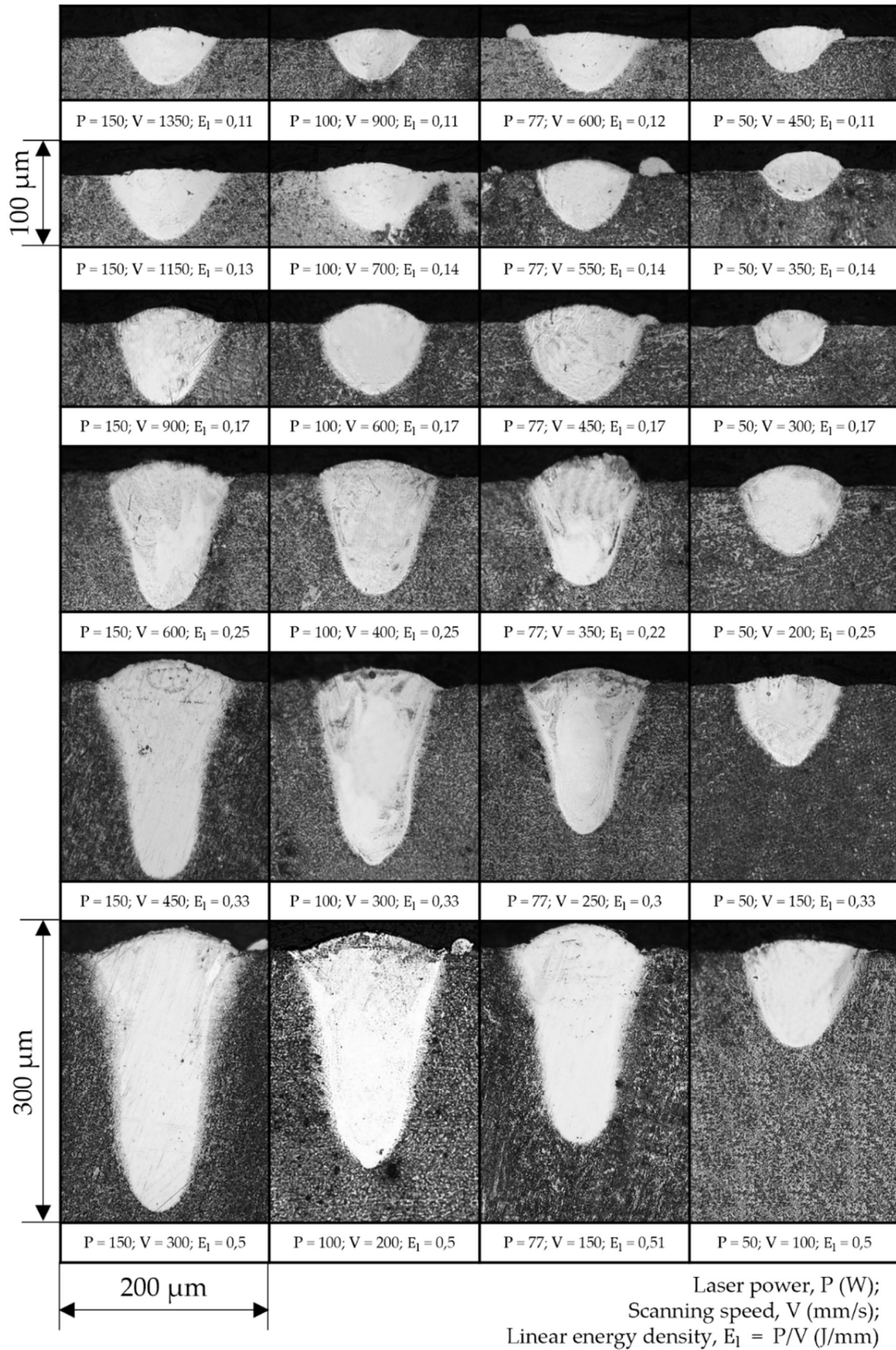


Figure 13. Cross-sections of single-track deposits for all combinations of parameters.

The authors of [55] studied the transition from conduction mode to keyhole mode and proposed Equation (26) for the evaluation of the laser speed threshold below which keyhole mode appears. However, the experimentally obtained threshold of the scanning speed was higher than calculated using the analytical expression.

$$V = \frac{4\alpha}{r_b} \left(\frac{\pi^{\frac{3}{2}} k T_b r_b}{A \cdot P} \right)^{-2} \quad (26)$$

where V is scanning speed threshold, α is thermal diffusivity, r_b is laser beam diameter, T_b is boiling point, A is absorptivity, and P is laser power.

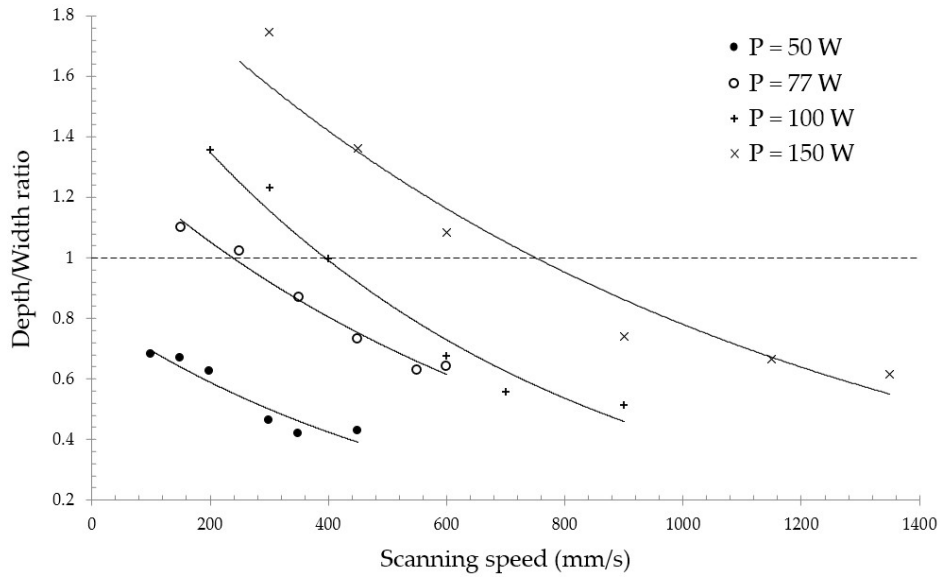


Figure 14. The depth-to-width ratio for the experimentally obtained single tracks.

3.3 Single Track-Based Thin Walls

For optimization of the process parameters for the LPBF process, a two-stage procedure well-established approach is used, consisting of printing single tracks and volumetric samples. Once single tracks were obtained, the hatch distance parameter can be evaluated. In the second step, the mass density is determined for a different combination of laser power and scanning speed with hydrostatic, metallographic, or Micro-CT methods. Finally, for the selection of the process parameters, the part design and application should be taken into account. In the following, we propose an approach for the optimization of process parameters for the high-resolution LPBF consisting of studying thin walls consolidated in the vertical direction and with different inclined angles. The walls were

printed with 4 incline angles: 90°, 45°, 35°, and 25° as shown in Figure 15. The walls were placed on the platform with columnar supports; a stiffener was added to the back to avoid accidental deformation or strains due to the relaxation of thermal stresses. All samples had a width of 5 mm and a height of 6 mm.

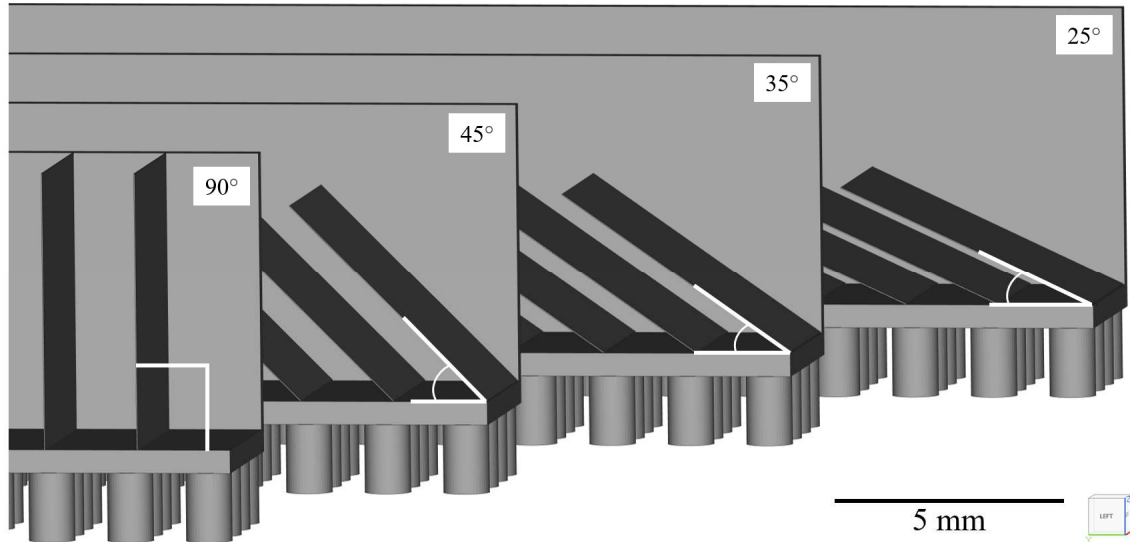


Figure 15. The samples of thin walls in Materialise Magics software.

The variables factors of the experiment were laser power and scanning speed with the levels presented in Table 4. Based on the results of granulometric analysis (Section 3.1) the building plate step was kept at 20 μm . The window of the process parameters was chosen according to the 3.2 Section.

Table 4. The window of process parameters used for the optimization procedure.

Sample Name	Laser Power, W	Scanning Speed, mm/s	Linear Energy Density, J/mm
P50V200	50	200	0.25
P50V400	50	400	0.13
P50V600	50	600	0.08
P50V800	50	800	0.06
P50V1000	50	1000	0.05
P100V350	100	350	0.29
P100V600	100	600	0.17
P100V850	100	850	0.12
P100V1100	100	1100	0.09
P100V1350	100	1350	0.07
P150V500	150	500	0.30
P150V800	150	800	0.19
P150V1100	150	1100	0.14
P150V1400	150	1400	0.11
P150V1700	150	1700	0.09

Several scanning strategies can be employed for the manufacturing of micro-objects via the LPBF process. The first scanning strategy refers to layer-wise scanning of a powder bed with a single laser passage. The second mode which widely used for the strut-based lattice structures based on the generation of multiple perimeter contours [137] along the border of the 3D model. The third type is the conventional generation of the contours with subsequent hatching. It should be noted that despite the highest resolution achievable with the first mode, most of the build processors and commercial LPBF equipment do not switch to such a scanning strategy when the corresponding feature size of an object is comparable with the width of a single track. Wu et al. [17] found the possibility of switching from the raster mode to the single-bead mode on the EOS equipment. The adopted slicer algorithm used in this study enables gradual change of the scanning mode from the raster to the multiple contours' generation and finally to the single vectors. In this study, we consider samples produced with the first type of scanning strategy. Optical microscopy (OM) of cross-sections for thin walls consolidated with regimes given in Table 4 are presented in Figure 16. The samples were analyzed over the entire height with a panoramic tool of Thixomet software. Figure 16 shows a representative 2 mm long section from the central part of thin walls. Samples with a lack of fusion defect are highlighted in red. The cross-sections are subdivided by the inclined angle to the base plate; however, all images are presented horizontally.

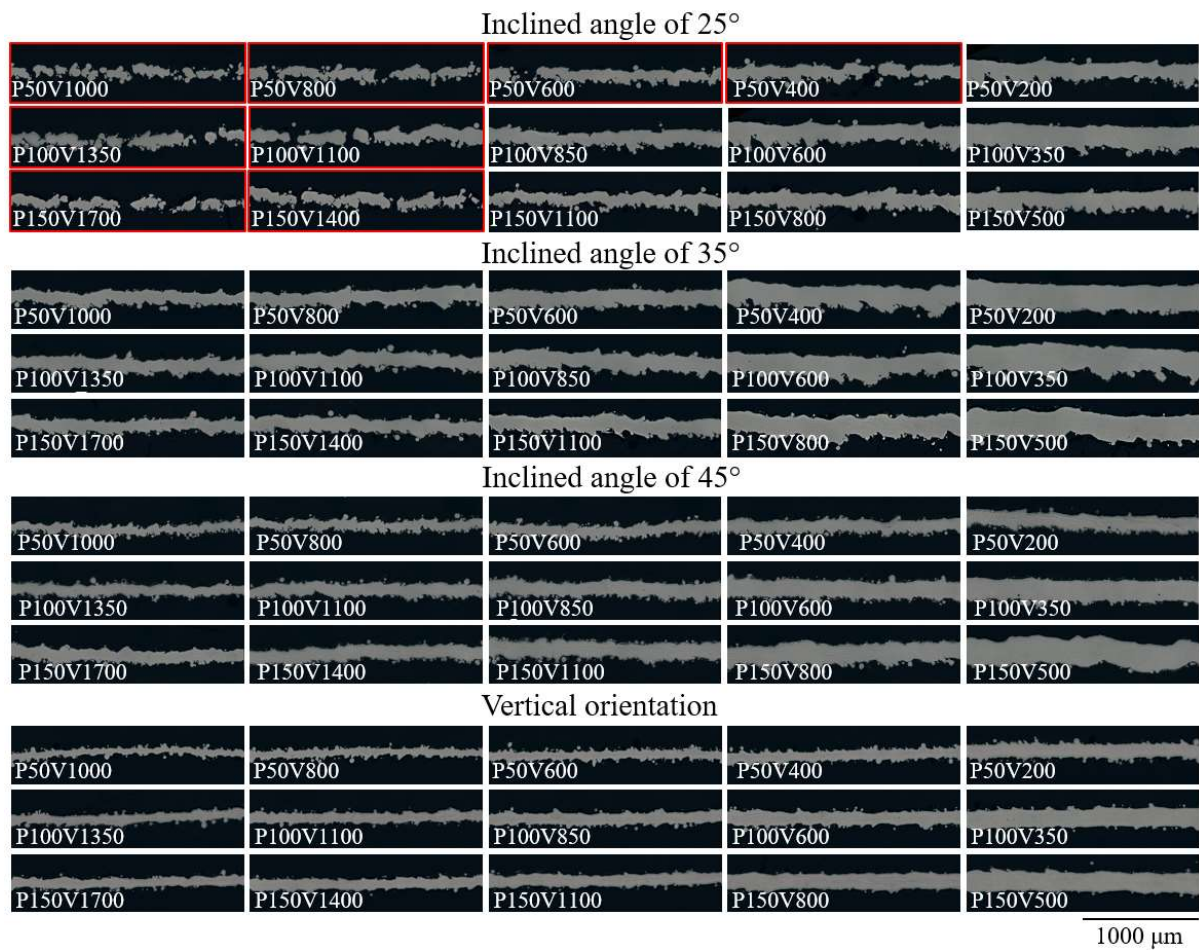


Figure 16. OM of cross-sections for single track based thin walls. Samples with lack of fusion defect are highlighted with red.

In Figure 17 experimental measurements of the thicknesses for vertical walls are presented and compared with the width of single tracks adopted from the work [45]. The minimum wall thickness of $54 \pm 10 \mu\text{m}$ achieved with a linear energy density of 0.05 J/mm is comparable with the laser beam diameter of $55 \mu\text{m}$. The corresponding single track width of $58 \pm 10 \mu\text{m}$ was achieved with the energy input of 0.11 J/mm . The width/thickness dependences on the linear energy density demonstrate a similar trend and have a logarithmic fit with $R^2 > 0.8$. However, the same laser energy input provided greater wall dimensions than the width of the relevant melt pool. Apparently, the phenomenological explanation relates to the difference in the substrates' properties. For the single track experiment, the NiTi base plate was considered as a substrate therefore the heat was evenly distributed from the powder bed to the dense material. For single track-based walls, the substrate was the previous layer of a thin wall surrounded by powder. It is known that the powder bed has an order of magnitude lower thermal conductivity and half of the density

of the bulk material. Thus, the melt pool width may increase due to restrained heat dissipation into the substrate, therefore, augmented heat accumulation by the surrounding powder in case of wall consolidation. Besides the above-mentioned statement, the powder adhesion may increase the average thickness of the wall by the median size of powder particles. The results comply with the experimental findings in works [17,41].

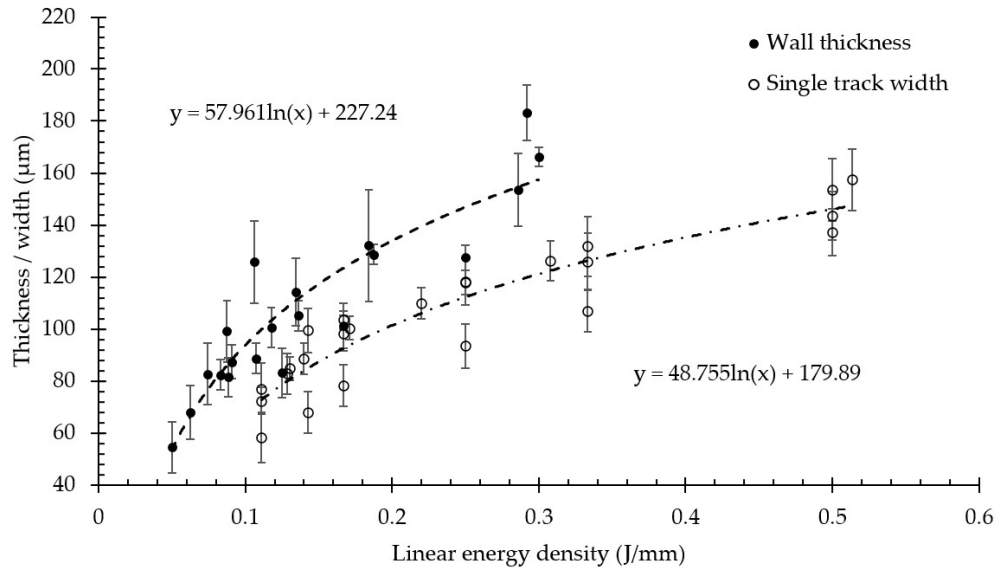


Figure 17. Dependence of wall thickness and width of single tracks on linear energy density for vertical samples.

Figure 18 shows the wall thickness with a standard deviation measured from samples with inclined angles of 25°, 35°, and 45°. The minimum wall thickness of $61 \pm 6 \mu\text{m}$ was achieved for the P150V1700 sample. For each regime, the linear energy density value is marked with a square marker and a dashed line. It is seen that in the case of inclined walls, the thickness also correlates with the linear energy density and the minimum value is comparable to vertical specimens. Thus, the minimum wall thickness has a weak dependence on the angle of inclination and is mostly controlled by the melt pool geometry.

However, the linear energy density is hard to use as a parameter for the evaluation of the thickness for several reasons. It was shown that the laser power strongly affects the threshold of linear energy density at which the transition from the conductive welding mode to the keyhole occurs. The linear energy density of 0.30–0.40 J/mm was considered as a threshold value based on the experimental melt pool formation analysis and simulation results of the temperature fields during LPBF [45]. Therefore, in the present window of technological parameters, the curves have no singularities commonly associated with rapid

changes in the melt pool geometries from the conductive mode welding into a deep keyhole. However, the effect of laser power on the pool stability and formation conditions appears even below the threshold value to a lower extent. It is worth mentioning that for the laser power of 50 W the specimens with a 35° inclined angle have a higher value of the wall thickness, for a laser power of 100 W the difference between the thickness of samples with different incline angles is negligible, and for a laser power of 150 W the thickness for the sample with a 45° inclined angle have a smaller thickness.

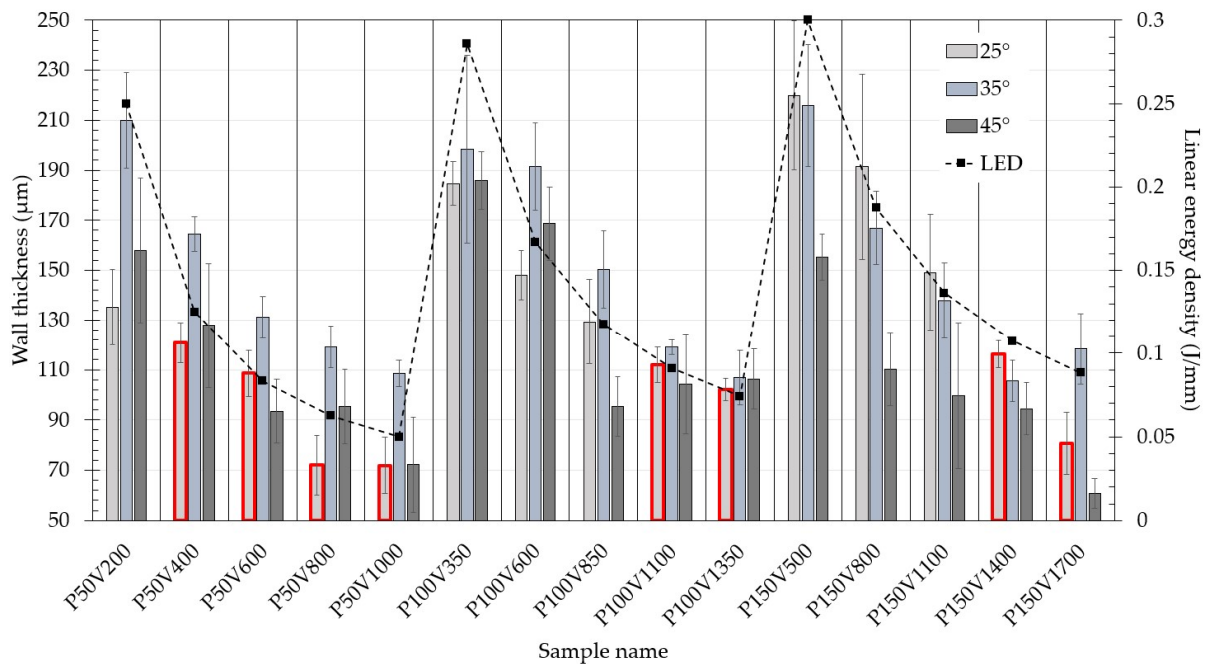


Figure 18. Dependence of wall thickness on linear energy density for inclined walls.

The bars highlighted in red (see Figure 18) represent walls with a lack of fusion defect. Commonly, a lack of fusion defect is associated with pores filled with unmelted particles and is mostly controlled by the overlapping of the adjacent tracks. The lack of fusion defect in the case of single track consolidation leads to the discontinuous structure shown in Figure 19a. Discontinuous element with open pores significantly decreases the mechanical properties of a micro object. The condition of the defect appearance is an interplay among the melt pool size and inclined angle which in turn result in different overlapping of the adjacent tracks. It can be seen that all samples with defects have the lowest inclined angle of 25° and a low linear energy density. A simple model can be used to evaluate the limits of both factors. Two adjacent layers are considered in a plane perpendicular to the laser scanning vector. In each layer, a melt pool represented by a

parabolic shape and overlapping is estimated. We consider the following assumptions: the shape of the melt pool corresponds to the shape obtained during the scanning of the powder bed on the bulk substrate, the melt pool's upper surface is flat, and the formation of the tracks is stable. As input parameters, layer thickness (t), inclined angle (α), height (h), and width (w) of the melt pool are considered. The dimensions in Figure 19b represent the experimentally measured data on the single tracks for the P150V1400 from [45]. In this case, ($t \tan \alpha$) parameter can be used for the single track consolidation as an analog of hatch distance. Accordingly, for samples P150V1400, P150V1100, and P150V800 calculated overlapping areas are 8.8, 17.7, and 29.7% respectively. In prescribed process parameters matrix, samples with overlapping areas below 10% resulted in a lack of fusion defect. However, more experimental data on the melt pool geometry is required to formulate limitations for inclined object manufacturing based on this model.

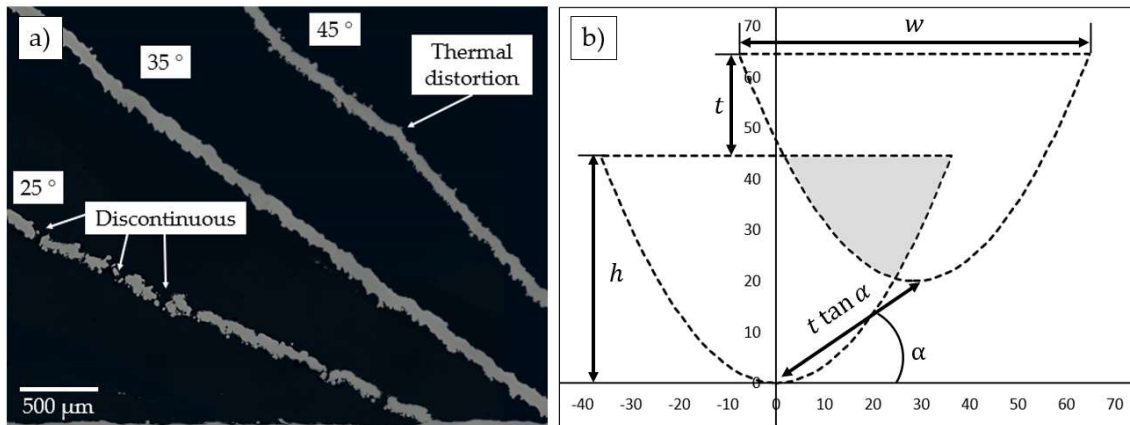


Figure 19. a) OM of walls with different inclined angles; b) schematic representation of the overlapping between adjacent tracks during single track manufacturing of inclined objects.

3.3.1 Samples manufacturing for mechanical testing

Samples of thin walls for mechanical tests were manufactured via a single-track based scanning strategy. All thin walls were placed in cassette assemblies as shown in Figure 20. Additional wall stiffeners prevent possible deformations of samples due to scrapper interaction and residual stress release. All samples were marked by 200 μm deep extrusion of a single surface 3D model. During printing of thin walls local cracks of stiffeners and burr formation on the top surface of samples were observed. However, the final samples were cut from the cassette, thus the effect of the abovementioned defects was

excluded. It is worth noting that no visible defects were detected in the central part of samples.

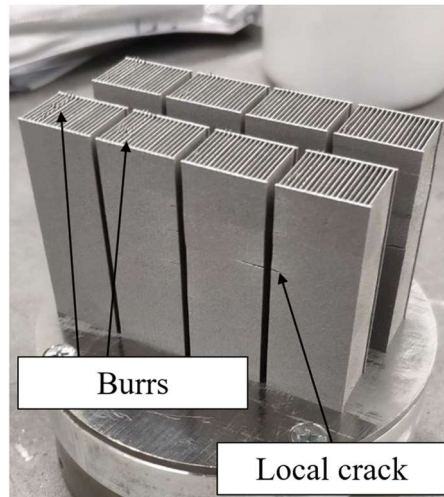


Figure 20. Cassette assemblies of thin walls in z orientation.

The samples were cut in a flat dog-bone form for mechanical tests according to drawings in Figure 21a. The distance between shoulders could be reduced due to the utilization of a non-contact deformation measurement system that does not require additional gauge length as in the case of physical extensometer placement. The transition from reduced to the grip section was designed with a rounding radius to minimize local stresses. For mounting of samples special envelope was 3D printed from 316L (Figure 21b).

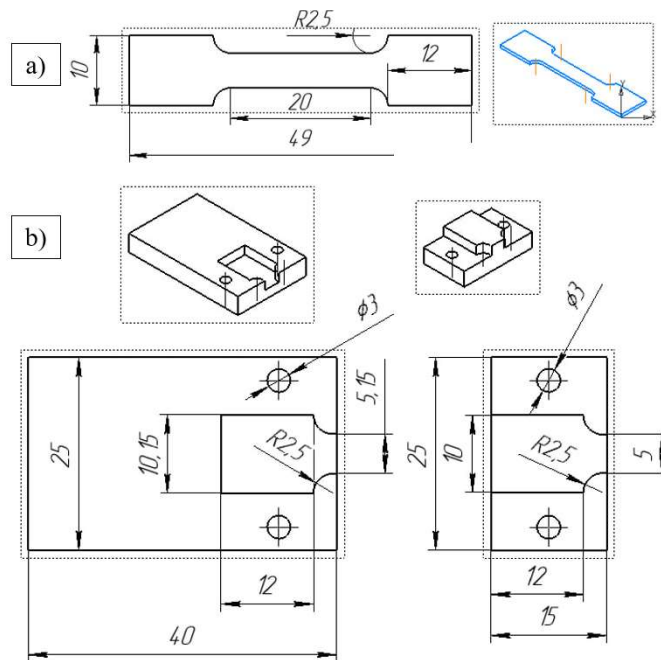


Figure 21. Drawing of a) flat dog-bone sample, b) mounting for mechanical tests.

3.3.2 Microstructure of thin-walled samples

Figure 22 shows the results of microstructural analysis for representative samples manufactured vertically with different laser energy inputs. All thin-walled samples demonstrate an elongated grain structure along the building direction (marked with BD and arrow). It is known that for the laser-based consolidation of material, the transition between columnar and equiaxed structures are dependent on the variation in the thermal gradient and the solidification rate velocity [140]. Consequently, for some process conditions such transition should exist, however, a strong texture was observed for all samples despite the wide range variation of the laser power and scanning speed. Observed texture and grain morphology is explained by the limited heat sink for the prescribed type of laser-based manufacturing. In comparison with the volumetric part when the scanning strategy involve contours and hatching regions, the heat from the melt pool dissipate to the whole volume of previous layer which represented with solid remelted metal. For the thin-walled part, heat sink has a single direction for heat transfer which governing the crystallization.

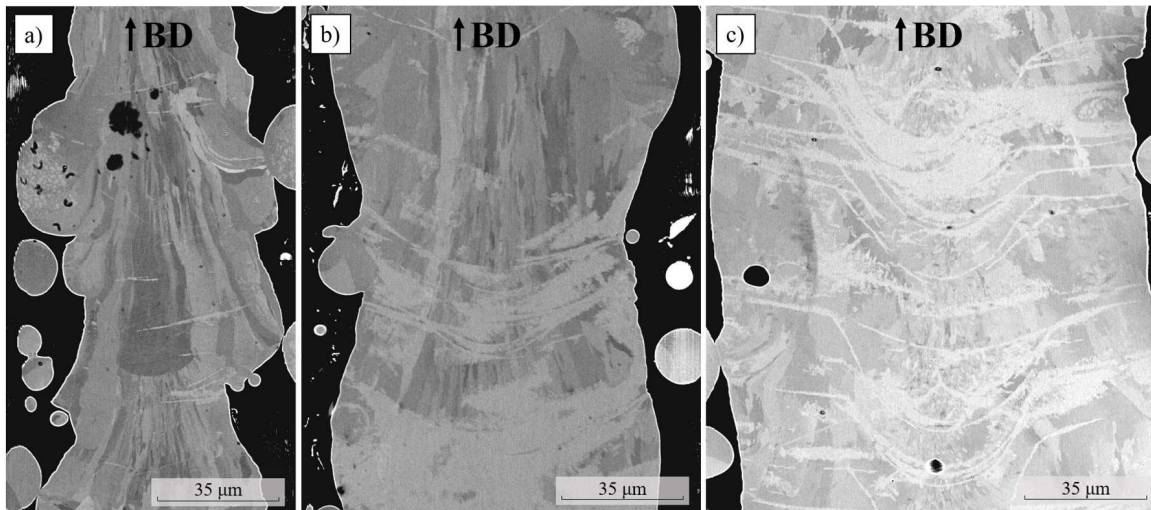


Figure 22. SEM images of thin wall samples' microstructure for regimes: a) P50V600, b) P100V850, c) P150V500.

The boundaries of solidified melt pools have different morphologies for all three cases. In the case of low LED (Figure 22a), the melt pool boundaries are straight and perpendicular to BD. Such morphology appeared during crystallization of a relatively small volume of liquid and short lifetime of the melt pool accompanied by low wetting condition. For the P100V850 regime (Figure 22b), melt pool shape corresponding to conventional conductive mode of melting. The wall thickness fluctuations have significantly lower

period in comparison with the P50V600 sample due to multiple remelting of previous layers. Finally, for high LED (Figure 22c) the morphology of the melt pool is represented with keyhole shape. As far as central part of the keyhole is deeper, the core of the wall will be remelted more times in comparison to the edges. Such feature of the melting regime may introduce inhomogeneity to the microstructure, TTs, phase composition. Interestingly, melt pool boundaries are more distinct for the P150V500 regime, and the distance between some adjacent boundaries is close to the step of the build platform.

3.4 Static mechanical testing of thin wall samples

Samples described in Section 3.3.1 were subjected to mechanical uniaxial tensile tests. To investigate the effect of the process parameters (linear energy density) on the mechanical response, higher strains are of interest. Therefore, static uniaxial tensile tests until fracture were performed at first to analyze the maximum strain that can be subjected to thin wall samples.

The results of the calculated Lagrangian strain field (ϵ_{11}) on top of the images from the cameras are shown in Figure 23. Such fields were analyzed for both test (until fracture and single cycle) to precisely measure the deformation.

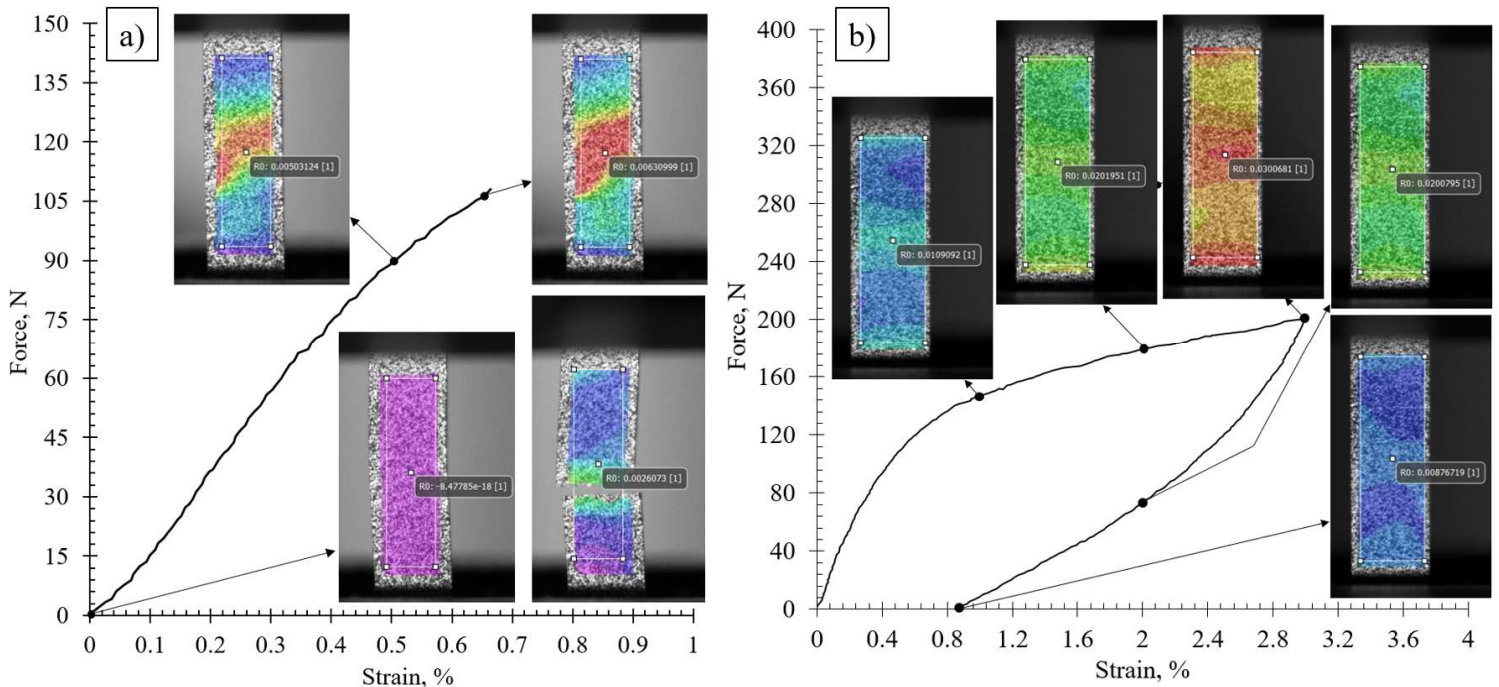


Figure 23. Stress-strain curves with corresponding DIC images for sample a) P50V600 [until fracture] and b) P100V850 [single cycle loop]

3.4.1 Static uniaxial tensile tests until fracture

According to the results of static mechanical tests until fracture, all samples can be divided on the low ($< 1\%$ strain) and high ($> 2\%$) elongation to fracture cases. Those groups are henceforth referred to as LE (low elongation) and HE (high elongation). After the tests, SEM fractographs were obtained for all samples to determine fracture mechanisms. Typical fracture surfaces for both cases are given in Figure 24.

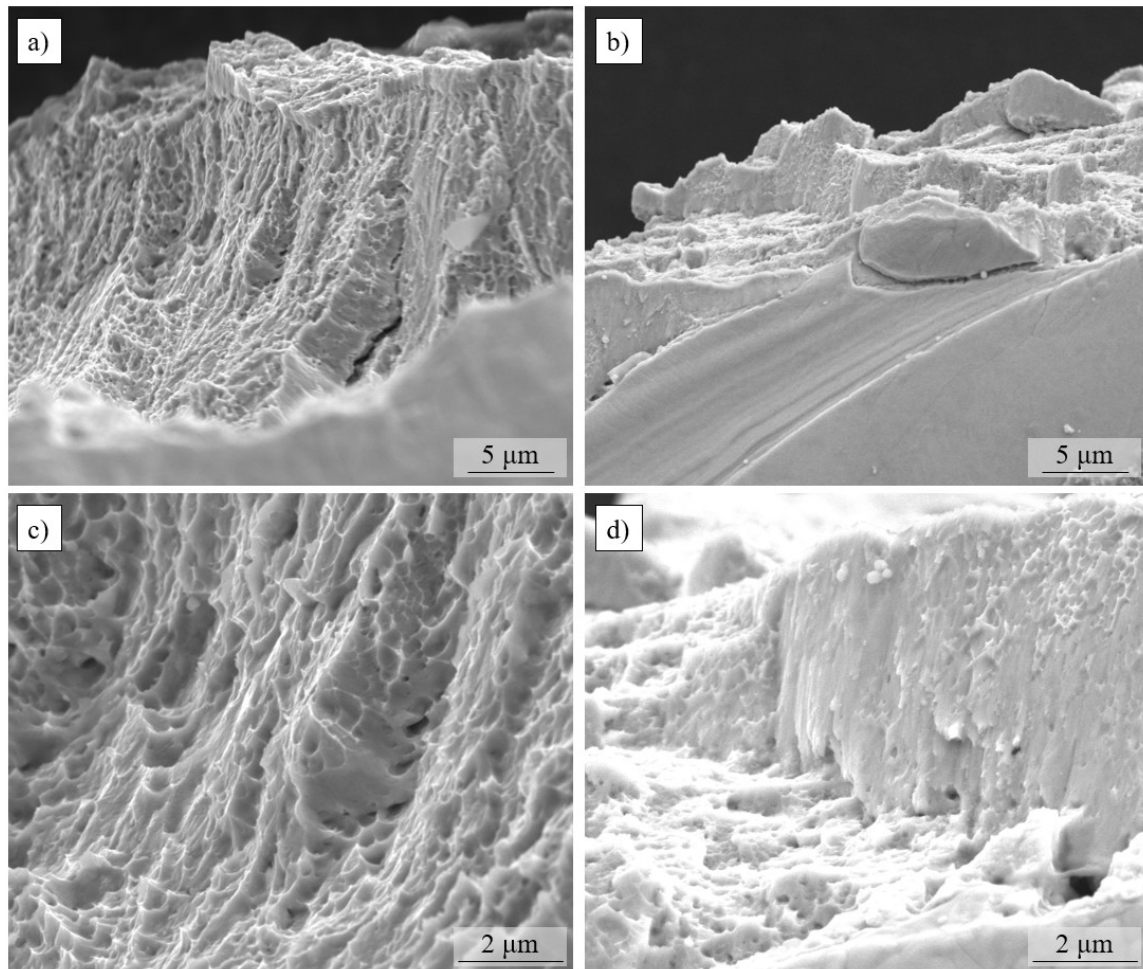


Figure 24. SEM images of fracture surface for samples P100V350 (a,c) and P100V1350 (b,d) with magnification of 10k (a,b) and 30k (c,d).

The representative HE sample manufactured with the P100V350 regime (Figure 24a,c) demonstrates cup and cone fracture. The surface is represented with lots of dimples, and overall increased roughness. This morphology indicates fracture due to void growth to coalescence [141]. The fracture had a ductile mechanism with extensive plasticity. Ductile fracture is common for NiTi processed in conventional conditions such as cold working or

aging [142]. The fracture surface of the LE sample consolidated with the P100V1350 regime is demonstrated in Figure 24b,d. A mix of flat and slant morphology occurred as a consequence of the prevailed plane stress during loading conditions. Partially, dimples are also presented for the LE case (Figure 24d). However, the flat regions occurrence during deformation indicates the crack initiation and propagation. Any defect in the metal structure serves as the nucleation core of the crack. In terms of the LE group of specimens, the lack of fusion pores is referred to the aforementioned defects. When a sufficient number of pores is presented in the volume, coalescence between the nearest is influenced by the crack propagation [141]. Such behavior is considered as the multiple void interaction mechanism. Thus, it is noted that LE samples demonstrate brittle fracture with low resistance to crack growth.

For the SME analysis, one-cycle loading tests were performed. Due to the brittle fracture for some samples, high deformation conditions cannot be achieved in the whole window of the process parameters. Therefore, a maximum strain of 3 % was utilized for the one cycle of loading-unloading. The reverse movement of the load cell was switched manually with precise control of deformation. The actual deformation value was provided by immediate analysis of the last frames captured by DIC.

3.4.2 Single loading cycle uniaxial tensile tests

Results of mechanical tests are presented in Figure 25(a-c) with division by laser power. Firstly, various levels of stress plateau (associated with the stress of reorienting martensite by twinning) were achieved. This difference is attributed to a change in the thickness of thin wall-based samples. As far as the thickness is controlled by linear energy density this effect is considered size-dependent and is not analyzed further. Secondly, a noticeable difference was observed in reversible/irreversible deformation ratio. Such a response is only connected with material properties and, therefore, can be considered as an indicator of technological parameters' influence.

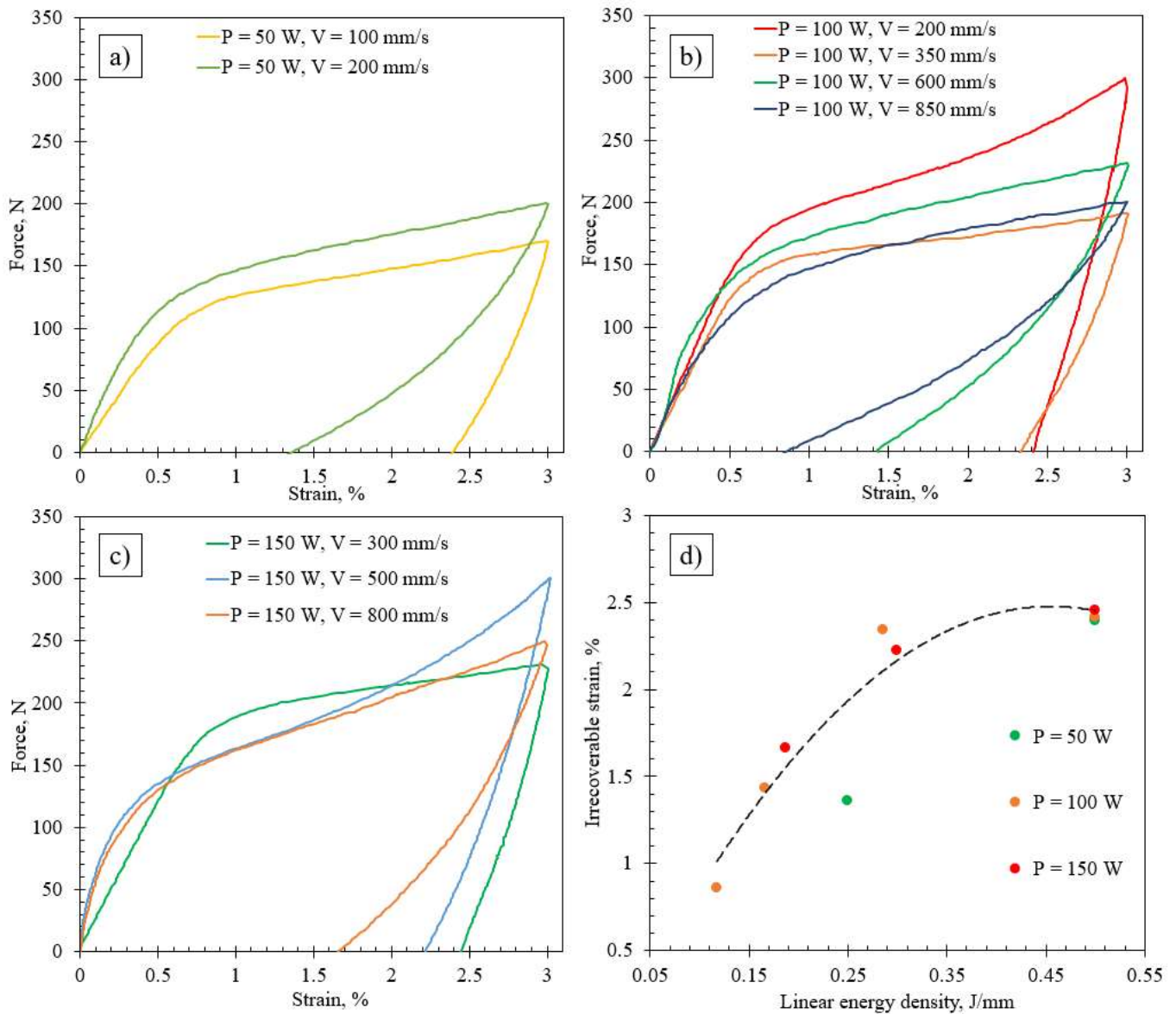


Figure 25. Results of mechanical tests with one cycle of loading-unloading up to 3 %.

For each group of samples manufactured with different laser power dependencies of irrecoverable strain is visible. Increasing linear energy density led to a growth of irrecoverable strain as demonstrated in Figure 25(d). After 0.35 J/mm the value reached saturation point at ~ 2.5 %. This is attributed to the increase of austenite finish temperature above the room temperature at which the test was conducted. Thus, for all samples with LED above 0.35 J/mm only purely elastic deformation was recovered. According to the segmentation of mechanical response (Figure 4) the samples manufactured with LED above 0.35 J/mm are considered as purely in the SME domain, when all samples below the prescribed LED value are in mixed SME + SE region. Based on the received irrecoverable

strain values, the recovery ratio was calculated in accordance with Equation (27). All characteristics describing the mechanical response of the material consolidated with different laser processing conditions are presented in Table 5.

$$Recovery\ ratio = \frac{\epsilon_{recovered}}{\epsilon_{total}} \cdot 100\% \quad (27)$$

The highest recovery ratio of 68 % was obtained for the sample P100V850. Complete recovery after the deformation is necessary for the correct and stable functioning of the material. In this regard, obtaining a high recovery ratio is considered as one of the important technological challenges related to LPBF manufacturing of NiTi: Saedi et al. in the work [16] reported a value of 95 % after heat treatment with solutionizing and aging, Haberland et al. received the same level of recovery ratio after multiple loading cycles [47], Moghaddam et al. reported the highest recovery ratio of 98 % that was achieved without heat treatment [83]. It should be noted that in the present research recovery ratio is considered only as one of the indicators to describe the material properties, however, found dependencies from process conditions can be used to maximize the recovery ratio for devices manufactured with high-resolution LPBF.

Table 5. Mechanical properties of NiTi thin wall samples.

P, W	V, mm/s	E_l , J/mm	ϵ_{rec} , %	ϵ_{irrec} , %	Recovery ratio, %
50	100	0.50	0.66	2.34	22
50	200	0.25	1.64	1.36	55
100	200	0.50	0.54	2.46	18
100	350	0.29	0.56	2.44	19
100	600	0.17	1.50	1.50	50
100	850	0.12	2.05	0.95	68
150	300	0.50	0.46	2.54	15
150	500	0.30	0.78	2.22	26
150	800	0.19	1.27	1.73	42

The sample with the lowest LED of 0.12 J/mm had the minimum irrecoverable strain of 0.86 %. It is noted that a further decrease in LED could result in SE response of samples, however, poor ultimate tensile strength will limit the application of such consolidated part. In this regard, when SE response of NiTi is desirable, the optimal LPBF regime presents a compromise between the tendency to increase the energy input to ensure sufficient UTS from one side and decrease LED to reduce irrecoverable strain after cyclic loading.

3.5 Characteristic temperatures of phase transformation

The phase transformation temperatures were determined using the DSC analysis for both the raw powder and single track-based thin walls (Section 3.3). Before the analysis plates were grinded with 2500 grit SiC sandpaper to remove the thermal response of residual powder.

The results of the DSC analysis for all samples are presented in Figure 26. All samples demonstrate one-step phase transformation indicating the absence of an intermediate R phase. Both martensite and austenite peaks are shifting to lower temperatures in the case of equal laser power. In the case of a higher laser power (150 W) the temperatures of the phase transformation experience a higher shift than in the case of a low laser power (50 W). Additionally, curves of the samples consolidated with 150 W laser power have the most distinct peaks which is comparable with the effect of the recrystallization and homogenization heat treatments [16].

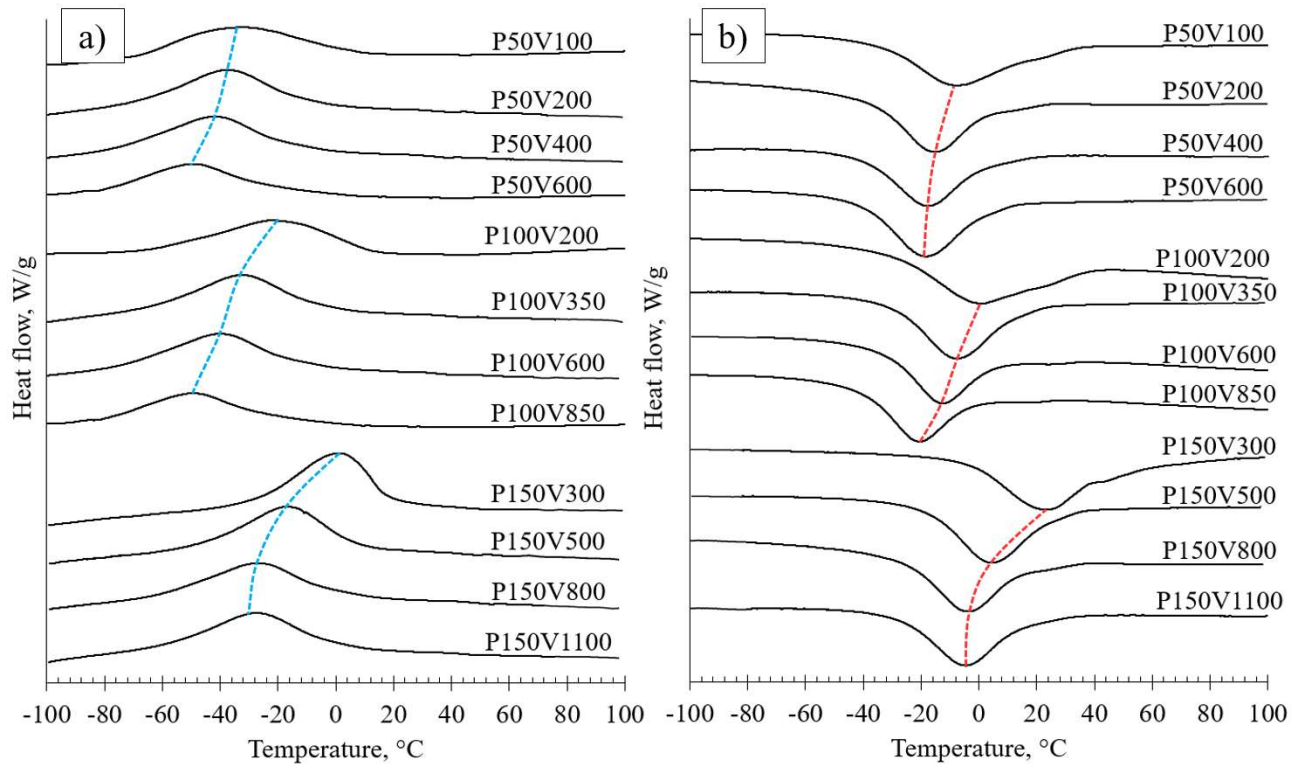


Figure 26. DSC curves of as-built samples with different LPBF regimes a) cooling and b) heating.

The exact temperatures for the start, peak, and finish of the austenite and martensite phase transformations are presented in Table 6. The values were determined according to the scheme in Figure 6.

Table 6. Characteristic temperatures of austenite and martensite transformations.

Sample Name (LPBF Regime)	Transformation Temperatures (°C)						
	M _s	M _p	M _f	A _s	A _p	A _f	ΔT
P50V100	11.7	-37.7	-71.1	-36.2	-9.1	26.5	28.6
P50V200	-9.8	-38.5	-36.5	-36.6	-15.4	5.7	23.1
P50V400	-13.9	-41.5	-76	-40.4	-17.4	5.9	24.1
P50V600	-15	-48.8	-80.7	-40.3	-18.8	5.1	30
P100V200	14.5	-17.6	-64.5	-31.5	-2	41.2	15.6
P100V350	-3	-33	-62.3	-39.2	-7.9	15.3	25.1
P100V600	-10.4	-40.5	-69.9	-33.1	-13	6.8	27.5
P100V850	-16.1	-49.7	-81.7	-42.3	-20.9	-1.8	28.8
P150V300	20	1	-31	-4.5	23	43	22
P150V500	14	-17	-58	-19.5	4	29.5	21
P150V800	9.5	-27	-76	-29.5	-4	20	23
P150V1100	9.5	-27.5	-71	-28.9	-5.5	17.1	22

Figure 27 shows the dependence of the onset temperature of martensitic phase transition from the applied linear energy density to the NiTi powder for consolidation. Most of the experimental data can be expressed with a linear regression model. However, some values of M_s have significantly high discrepancy from the trend. Those samples correspond to the regimes with the highest power of 150 W. Such deviation can be attributed to appearance of the secondary mechanism of change in the material properties, i.e. different solidification rates, and *in-situ* heat treatment.

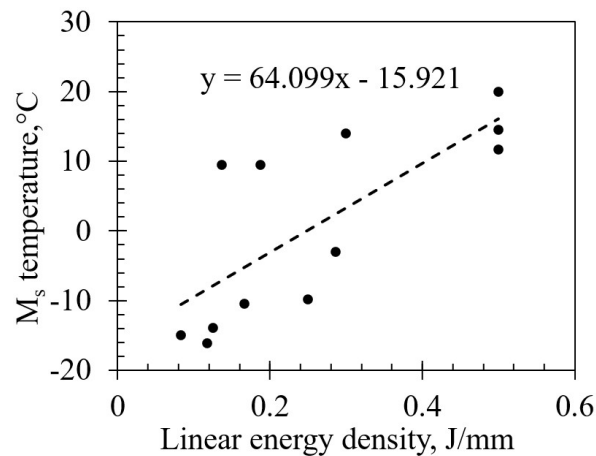


Figure 27. Dependence of the M_s temperature on the linear energy density.

3.6 Phase composition variation

The samples were prepared from plates manufactured as described in Section 3.3. Plates were ground similar to the DSC measurements (Section 3.5). Minimal grain size of

abrasive particles helps to decrease the stresses in the near-surface region which affects the results of XRD analysis [143]. In general, sample preparation is required to prevent the appearance of peaks from the diffraction of the X-rays on the residual powder adhered to the surface.

The X-ray diffractograms of the thin walls' samples consolidated under different process conditions are presented in Figure 28. The initial phase composition after LPBF is represented by the high-temperature phase (B2-austenite) and a small (not more than 20%) amount of a low-temperature phase (B19'-martensite) which aligns with DSC where the room temperature is located at almost the end of forward martensitic transformation (Figure 26). The prevalence of the high-temperature phase was expected as far as Ni-rich NiTi powder was used. The B2-phase peak intensity ratio of the thin walls is typical for a state close to isotropic: very strong $\{110\}$, medium $\{200\}$, and medium-strong $\{211\}$. The most intense peaks marked on the XRD spectra with red dashed lines of the B19' phase corresponding to the following lattice planes: $(11\bar{1})$, (111) , and (200) . The phase composition slightly changes with linear energy density for each laser power value. These observations correlate with the changes in the temperatures of martensitic transformation (Table 6). Peaks associated with precipitation by Ni_4Ti_3 were not observed. However, in the case of extremely high cooling rates that are inherent to the LPBF, two phase evolutions can be considered. The first is related to the complete suppression of secondary phase formation by the kinetics of the process. The second possible phase evolution refers to the formation of submicron precipitates. However, fine-sized precipitates are complicated to identify through XRD analysis due to the overlay of peaks by B2 and B19' phases as well as the overall low intensity to background ratio [144].

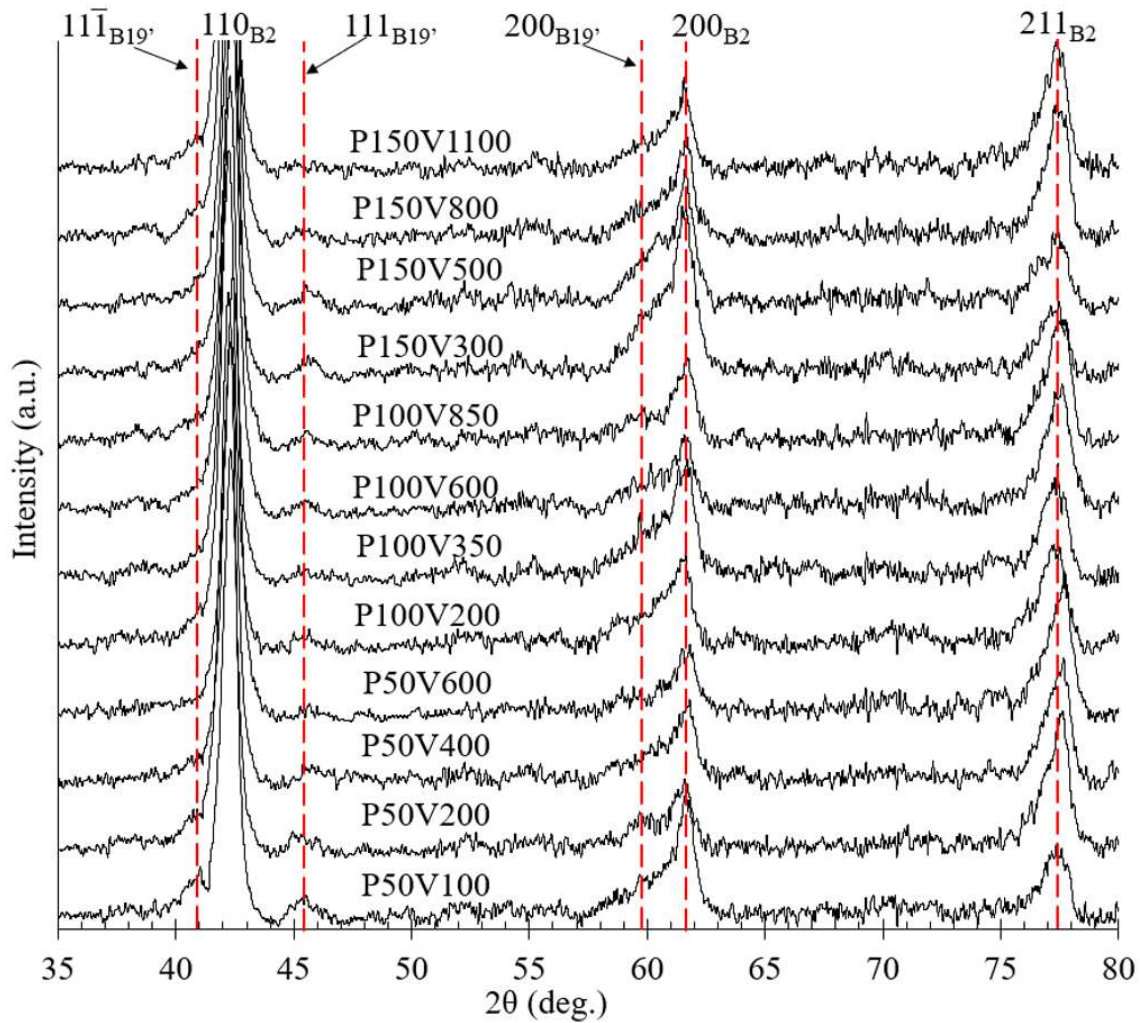


Figure 28. XRD patterns for as-built samples consolidated under different process conditions.

It is worth mentioning that the $\langle 100 \rangle$ family is an easy direction of heat transfer, and correspondingly easy-growth direction for grains, in the BCC system [145]. The strong effect of crystallographic texture was not observed on XRD patterns with a change in laser energy input. The texture formation with an increasing energy density during LPBF was previously observed for volumetric sample consolidation [146,147]. Thus, the strongly pronounced texture is more likely to appear when many adjacent tracks are introduced to the scanning strategy.

Assuming the material is a two-phase mixture, the phases' volume fractions can be estimated. For the quantitative evaluation of the ratio between the martensitic and austenitic phases, an evaluation of relative integrated intensity was performed for the X-ray diagrams [148]. The volume fraction of martensite was calculated by Equation (28) for each plate

consolidated with different regimes. The normalized intensity of each peak by background and width is given by Equation (29).

$$V^{B19'} = \frac{\sum I_0^{B19'}}{\sum (I_0^{B19'} + I_0^{B2})} \quad (28)$$

$$I_0 = \frac{(I_{peak} - I_{back})B_{hkl}}{I_{back}} \quad (29)$$

where, $V^{B1'}$ – is a volume fraction of martensite and austenite respectively, I_0 – normalized intensity, I_{peak} – intensity of peak, B_{hkl} – width of peak at half of intensity, I_{back} – intensity of background noise.

It should be noted that all peaks (both austenitic and martensitic) from the X-ray diagram (Figure 28) were used for the calculation. Results of the volume fraction evaluation are presented with a histogram in Figure 29. The obtained values depicts the ratio between the integral intensity of peaks corresponding to B19' and all peaks taken into account. Considering an estimation error, it was concluded that the martensite volume fraction reduces with an increase in scanning speed for each level of laser power. The aforementioned result is related to the issue of receiving the required functional properties in the as-built state.

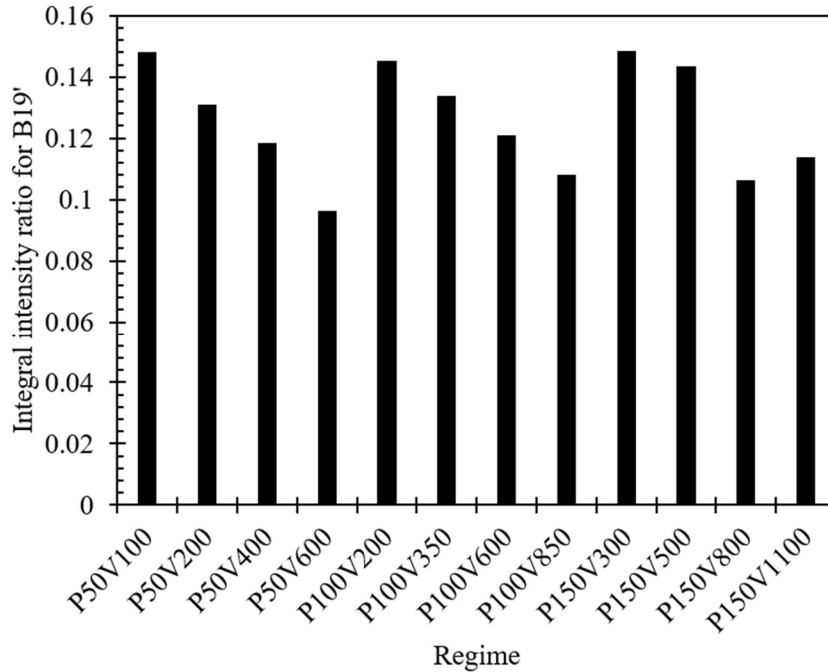


Figure 29. Change in integral intensity ratio for B19' with relation to the consolidation regimes.

3.7 High-resolution LPBF 4D printing concept

A demonstration of 4D printing feasibility via high-resolution LPBF was implemented with the following experiment. A 3D object with thin-walled parts was designed as shown in Figure 30a. For the closest reproduction of samples' process conditions investigated in Section 3.3-3.6, a relatively simple design was considered. However, significantly more complex geometries can be obtained with high-resolution LPBF as discussed in Chapter 5. The vertically oriented walls had several interconnections to increase the rigidity of the structure and prevent possible warpage due to the thermal stresses. All six walls were consolidated with different regimes, namely P150V300, P150V500, P100V200, P100V350, P50V100, and P50V200 (clockwise). The printed sample is shown in Figure 30b.

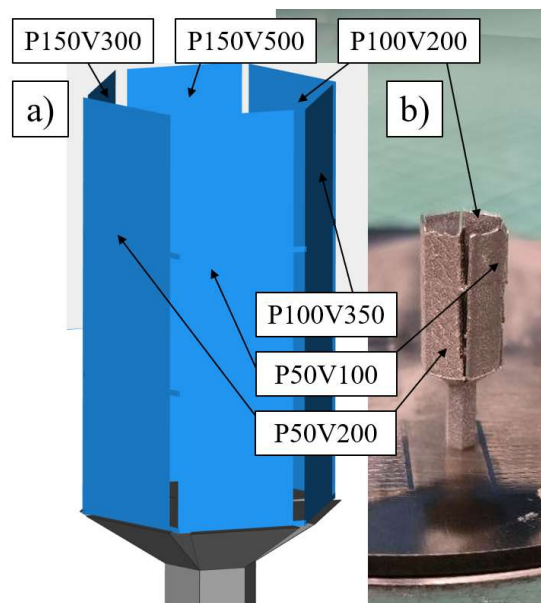


Figure 30. a) design of thin-walled structure, b) consolidated sample on the NiTi substrate.

For further research, a setup consisting of a camera from DIC system (Section 3.4), an infrared camera, and a flat heater was used. High-resolution cameras were focused slightly above the flat surface that was heated up to 120 °C. For temperature monitoring Fluke Ti450 (USA) thermographic camera was installed. The device works in the temperature range from -20 °C and 1500 °C with a precision of 2 °C, and a thermal sensitivity ≤ 0.03 °C. To ensure fully martensitic phase composition the sample was cooled in liquid nitrogen. In the next step, all thin walls were deformed to an equal radius of curvature (5 mm). The cooling was repeated between each thin wall to prevent SME

activation. Finally, the deformed sample was placed on the heater where the temperature and shape recovery were monitored simultaneously.

The analysis of SME activation is presented in Figure 31. Once the sample was placed on the heater, it had a brightness temperature of $-12\text{ }^{\circ}\text{C}$ in the initial state (Figure 31a). Plates printed with a low linear energy density experienced shape recovery first without a significant difference between each wall. A relatively narrow temperature range for complete shape recovery is associated with decreased temperature hysteresis demonstrated in Section 3.5. Mean brightness temperatures recorded for the samples P150V500, P100V350, and P50V200 were close to their A_f values (Figure 31b). However, an insignificant stepwise recovery process can be noticed. Such a behavior is attributed to possible inhomogeneity in the start and end of the laser track due to the finite rate of power gain or attenuation. At the next stage, SME was executed sequentially in plates consolidated with P100V200 and P50V100 respectively. The temperature of the structure once recovery finished was significantly higher than for low linear energy density samples (Figure 31c). At last, SME appeared in a thin wall printed with the P150V300 regime. For samples manufactured with increased linear energy density irrecoverable strain is visible (Figure 31d), even after heating up to $100\text{ }^{\circ}\text{C}$. It should be noted that the thickness of the walls is controlled by the width of the melt pool in the prescribed scanning strategy (Figure 17). Therefore, bending thicker plates onto the same radius of curvature can lead to plastic deformation.

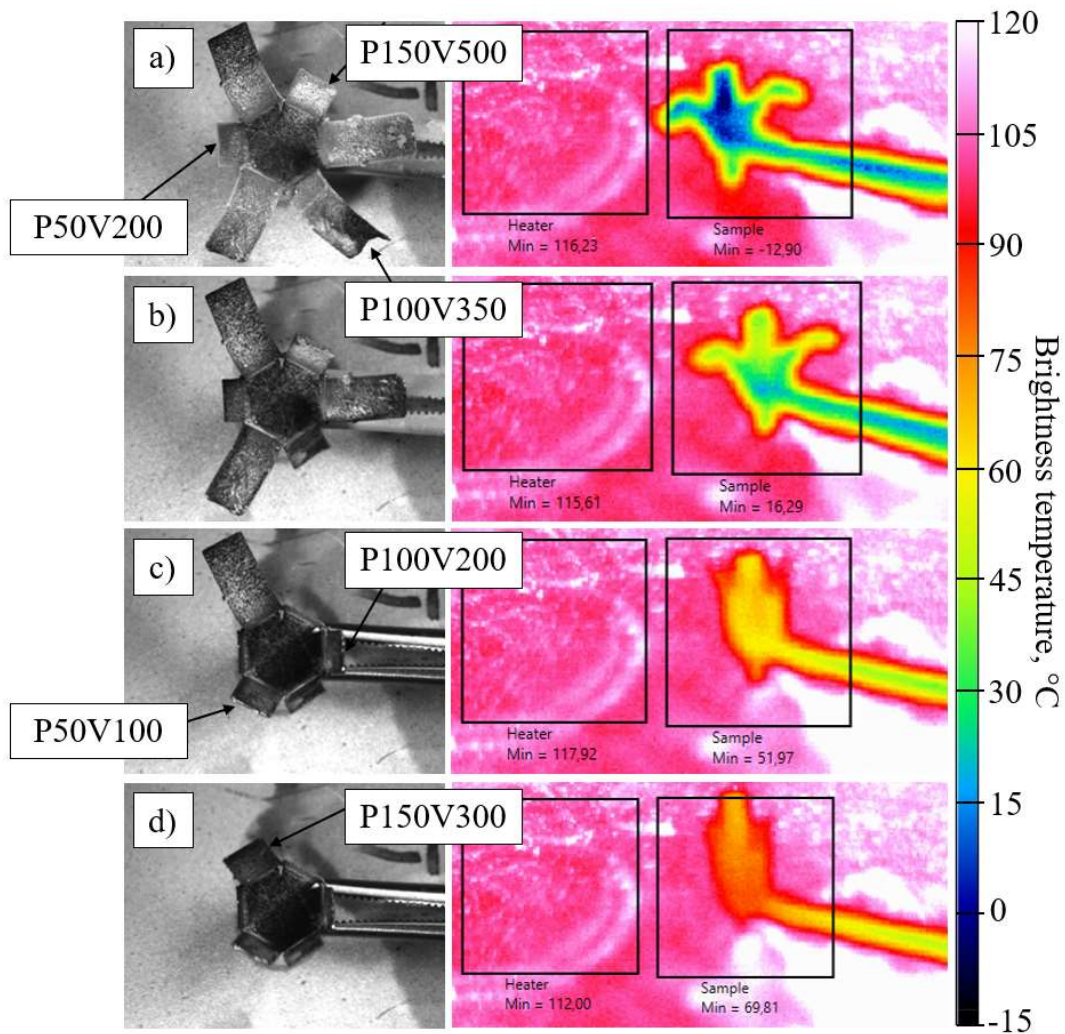


Figure 31. Multistage SME activation: a) initial state, b) shape recovery of samples manufactured with low linear energy density, c) activation of SME for samples P100V200 and P50V100, d) final state (P150V300 with irrecoverable strain).

Obtained observations are in good compliance with the results of Sections 3.4-3.5. The multistage nature of SME activation indicates successful *in-situ* tailoring of NiTi properties during LPBF. A distinctive peculiarity of this experiment from existing works [72,83,149] is the absence of hatching in the scanning strategy. Thus, the pure effect of laser influence is revealed without remelting by adjacent tracks.

Chapter 4. Simulation of the melt pool during LPBF

All simulations in the following chapter were performed in KiSSAM software with a high fidelity physical model based on a high-performance LBM hydrodynamic solver [120]. The program code does not have any calibration and empirical parameters and takes into account all important physical effects in LPBF, such as surface tension, Marangoni convection, powder wetting, laser energy deposition with multiple reflections, strong evaporation with recoil pressure, fusion/solidification and others. A more detailed description of the solver can be found in Section 2.3 and the paper [120]. The results of the dissertation assisted in the multicomponent evaporation model implementation (Section 4.6). All rights to KiSSAM software belong to Kintech Lab.

4.1 Thermophysical properties of NiTi for LPBF simulation

The thermophysical properties of NiTi alloy were extensively investigated with various technique with an emphasis on the requirements for mesoscale melt pool simulation during LPBF. All thermophysical properties utilized for simulation in the following chapter are summarized in Table 7.

Table 7. Summarized thermophysical properties for the melt pool simulation.

Property	Value	Units	Reference
Density of powder	3.53	$\frac{g}{cm^3}$	Section 3.1
Density of liquid	6.05	$\frac{g}{cm^3}$	[122]
Density of solid	6.45	$\frac{g}{cm^3}$	[122]
Solidus temperature	1513	K	[150]
Liquidus temperature	1583	K	[150]
Absorption coefficient	0.32	-	Drude's theory estimation [43]
Melting latent heat	370	$\frac{kJ}{kg}$	[151]
Dynamic viscosity	7.24	$mPa \cdot s$	[151]
Thermal diffusivity solid	$0.0095 \cdot T + 0.9769$	$\frac{W}{m \cdot K}$	Section 4.1.3
Thermal conductivity liquid	26.5	$\frac{W}{m \cdot K}$	[152]
Specific heat capacity solid	490	$\frac{J}{kg \cdot K}$	Section 3.5

Specific heat liquid	510	$\frac{J}{kg \cdot K}$	[152]
Surface tension near the melting point	1.53	$\frac{N}{m}$	Pendant drop tensiometry (Section 4.1.1)
Surface tension temperature coefficient	2.80E-04	$\frac{N}{m \cdot K}$	Coexistence theory calculation [153]
Coefficient of Antoine equation for Ni	6.667, 20765	-	Thermodynamic Properties database [125]
Coefficient of Antoine equation for Ti	6.358, 22747	-	Thermodynamic Properties database [125]
Laser spot size	55	μm	Machine specification (Section LPBF installation2.1.2)

In the following sections, measurements of surface tension for NiTi melt are performed for the mesoscale simulation of the NiTi melt pool. The effect of surface tension on the calculation results are presented in Section 4.4. Additionally, thermal diffusivity of the solid NiTi sample manufactured via LPBF was carried out.

4.1.1 Surface tension measurements of NiTi melt

In Figure 32a, a typical drop formed during the pendant drop experiment is presented. The drop had a mirror surface without any visible films of contaminations. The surface tension of the melt is balanced by the gravitational deformation of the drop. A pendant drop obeys the Young-Laplace equation that can be expressed in a system of differential equations in cylindrical coordinates. Thus, the resulting profile of a pendant drop is dependent on a single dimensionless variable β (Bond number):

$$\beta = \frac{\Delta\rho g R_0^2}{\gamma} \quad (30)$$

where $\Delta\rho$ is the density difference between two fluids, g is the acceleration of gravity, R_0 is the radius of the drop at the apex, and γ is surface tension. The Bond number together with the drop radius was directly calculated by fitting a solution to the detected profile of the drop (Figure 32a). Afterward, the surface tension was obtained from Equation (30). In Figure 32b a typical thermal profile is shown. The temperature during the experiment was controlled by thermal data averaged inside the drop contour. In Figure 32c results of the conducted experimental measurements on surface tension and temperature are presented as a dependence of time.

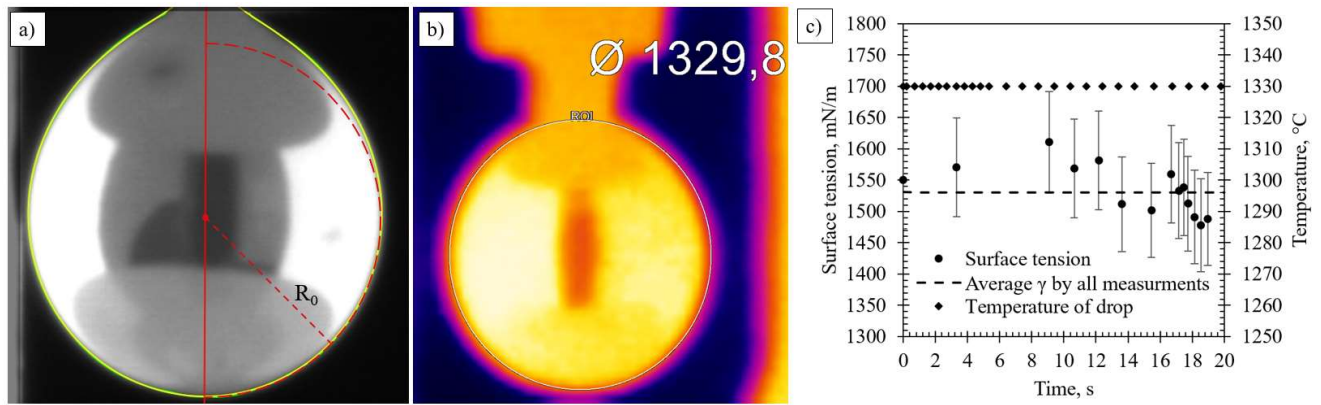


Figure 32. a) a typical image of a NiTi drop with a defined profile (green), an axis of symmetry (red), and a fitted profile (yellow) b) thermal imaging of a drop, c) surface tension of NiTi melt at constant temperature.

The accuracy of the measurements depends on the image quality and the drop shape. The first factor relates to the corresponding size of each pixel. The second factor is connected with the Worthington number or ratio between the actual drop volume and the theoretical maximum [154]. In the case of a low Worthington number, the interface is only slightly perturbed by the gravitation, therefore the sensitivity of measurement is reduced. Thus, the volume of the drop was gradually increased with simultaneous recording of the process. The images with the maximum sustainable volume before the detachment from the graphite dispenser were used for the analysis.

Several attempts were made to calculate the surface tension for liquid NiTi alloy via a thermodynamic approach. In paper [155] surface tension was calculated with quasi-chemical approximation and compound formation models. In the paper [153] authors used the coexistence theory. It was demonstrated that Ni-Ti system has a high deviation from the ideal solution according to both thermodynamic models. Combined data from the literature and the conducted experiment is presented in Table 8.

Table 8. Surface tension of equiatomic liquid NiTi obtained by different methods.

T, K	Surface tension mN/m	Methodology	Reference
1873	1774	Quasi-chemical approximation	[155]
1873	1792	Compound formation model	[155]
1873	1661	Ideal solution	[155]
1973	1670	Coexistence theory	[153]
1923	1682	Coexistence theory	[153]
1873	1695	Coexistence theory	[153]
1603	1530 ± 39	Pendant drop tensiometry	This work

4.1.2 Graphite crucible and NiTi melt interaction

The problem with experimental measurements is the strong chemical activity of nitinol. A rapid increase in temperature while shooting is a way to measure the drop's shape change in the reactive system NiTi-graphite. Classical long-time isothermal measurements lead to the formation of titanium carbide and dispersion of the melt drop onto the dropper. Therefore, in our experiment, we quickly raised the temperature up to a melting point and determined surface tension values. A formed barrier layer of TiC prevents further active penetration of carbon into the melt. A longer exposure leads to carbide formation inside the melt demonstrated via EDX analysis (Figure 33a). The melt between the graphite elements of the dropper was for several minutes, it can be seen the formation of carbide inside the melt (Figure 33b). Therefore, the experiment was carried out for a short time near the melting temperature. Indeed, the EDX spectra reveal a significant amount of oxygen near the surface, the influence of which is practically impossible to avoid in the case of titanium alloys and pure titanium melts. Thus, we obtained a surface tension value at 1603 K of 1530 ± 39 mN/m, which is the surface tension in the presence of oxygen with a partial pressure of 10^{-3} Pa or less. At the same time, no signs of solid phase or layer on the drop surface were found in the experiment at high temperatures. Thus, the relatively low value of the surface tension compared to the calculated one is explained by the oxygen adsorption.

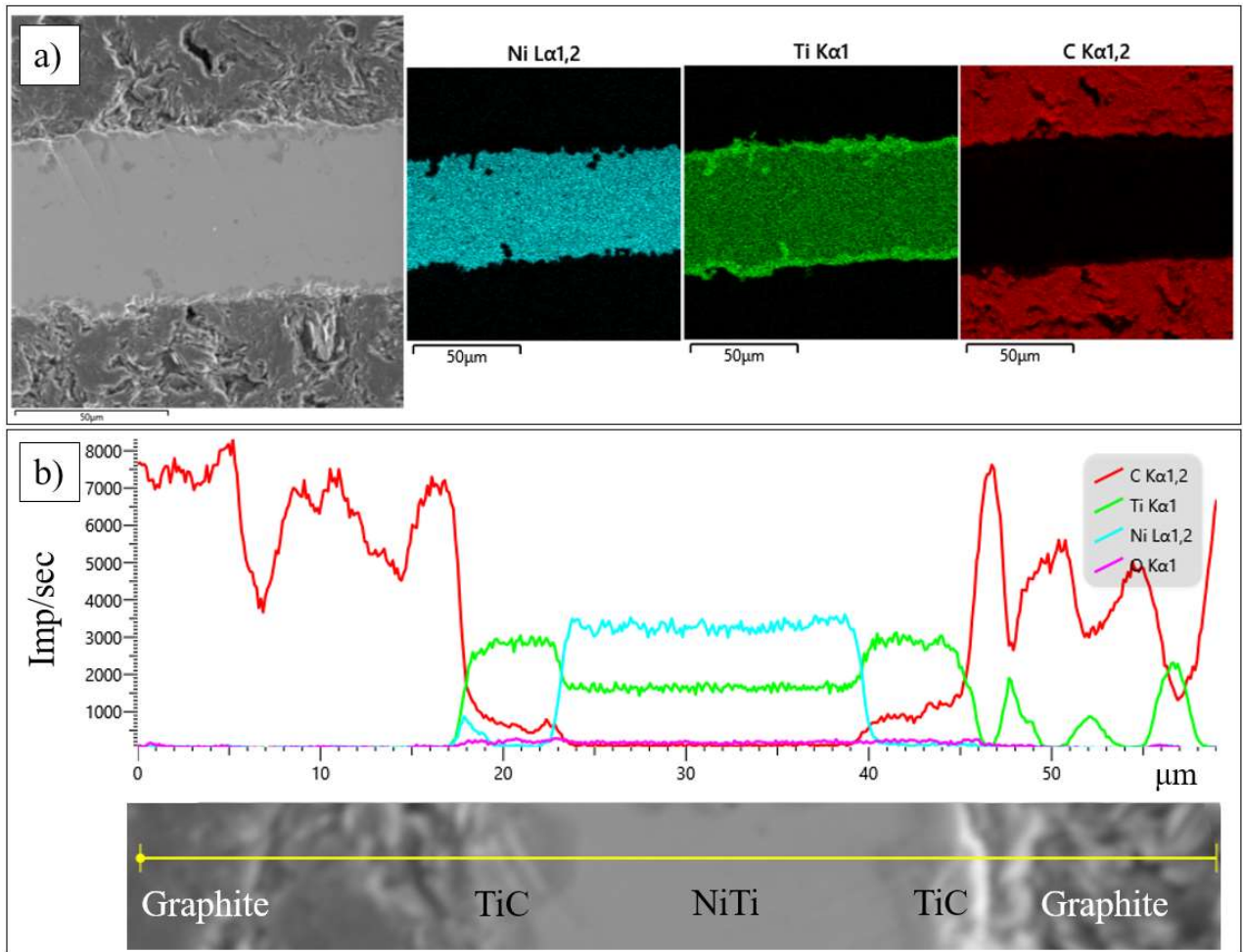


Figure 33. Analysis of solidified melt in the graphite: a) SEM image and chemical mapping, b) distribution of the elements along the marked line perpendicular to the channel

4.1.3 Thermal diffusivity

For the experimental measurements of thermal diffusivity, dense samples were manufactured from NiTi powder described in Section 3.1. The samples were consolidated in the form of a cylinder with a diameter of 12.7 mm and a height of 1.35 mm. For statistics, 3 samples were analyzed.

$$\alpha(T) = \frac{k(T)}{\rho C_p(T)} \quad (31)$$

The thermal diffusivity was measured with Laser Flash Analysis 447 NanoFlash (Netzsch, Germany). The method was proposed by Parker [156] The following conditions are assumed:

- fully homogenous material after the LPBF process
- homogenous energy input from the xenon lamp
- a short pulse assumption (pulse in the form of Dirac delta function)

For the processing of experimental data, the Cowan model was used [157]. The model provides more accurate results by taking into account heat losses by radiation and convection on the surfaces of the sample.

$$\alpha = 0.1388 \frac{d^2}{t_{0.5}} \quad (32)$$

For the analysis, the samples were placed in a special holder. From the one side, the sample experiences xenon lamp pulses while from the other side a detector (InSb non-contact infrared thermometer) measures the temperature. The measurements were conducted in the temperature range of 25 – 150 °C with step of 25 °C. For each temperature level, 5 measurements (shots) were made with a 7 second delay between each flash. The results of thermal diffusivity measurements are presented in Figure 34.

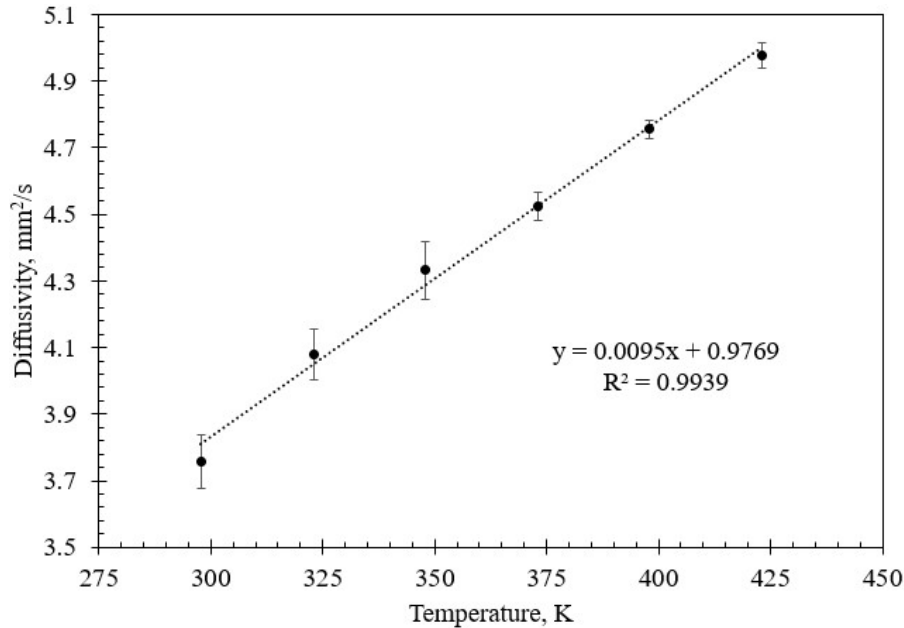


Figure 34. Temperature dependence of thermal diffusivity for consolidated NiTi.

The heat conduction in metals is provided by electric and phonon mechanisms. Although the electron contribution prevails, the phonon carriers, which refer to the lattice thermal conduction, are always present. The temperature dependence of thermal diffusivity is an indicator to infer the extent of phonon conductivity. With consideration of marked standard deviation, the temperature dependence is linear for the investigated range. Also,

linear temperature dependence of electric resistivity was previously demonstrated by Shishkovsky for the sintered samples from Ni₅₅Ti₄₅ powder [158] in a close temperature range. Thus, heat transfer through free electrons is considered the dominant mechanism for the studied temperature range. Found temperature dependence in $\left(\frac{mm^2}{s}\right)$ is $\alpha(T) = 0.0095T + 0.9769$ with R² of 0.9939.

4.2 Powder layer simulation

For the powder deposition simulation “PowDEM” script was used. The powder generator creates spheres randomly distributed on the substrate. The radii of spheres are generated according to the prescribed PSD. Each sphere is represented in a data array with coordinates of center and radius. Once the powder bed is formed on a flat substrate, the recoating blade begins to move along the x-axis (as in most slicers). After the operation particles are redistributed in a unique manner. All particles have no intersections and are meshed with assigned element sizes. As a result, an output file with *.vdb extension is created for further simulation.

4.2.1 Layer thickness during LPBF

One of the most important aspects of the powder bed simulation for the LPBF process relates to the correct choice of layer thickness. Most of the LPBF machines operate with a 20-40 μm step of the building plate. However, due to the significant shrinkage of the powder after consolidation, the layer thickness obviously differs from the step of the building plate. For the evaluation of layer thickness, we assume an increase of the powder density to the value of the solid state after melting. The number of layers during the LPBF process is indicated with i . Thus, after the first iteration of the recoating and melting process ($i = 1$) the layer thickness (t_{layer}) is equal to the step of the building platform (t_{step}) which is constant over the whole procedure:

$$t_{layer}^{i=1} = t_{step} \quad (33)$$

During the second recoating operation, the powder bed will be formed on the top of the melted powder layer that was shrinking by a factor $f = \frac{\rho_{powder}}{\rho_{solid}}$ if the complete shrinkage is considered. Therefore, additional thickness for i^{th} layer will be $(1 - f)t_{layer}^{i-1}$.

Thus, the layer thickness for the second and the third layer will be given by Equation (34) and Equation (35) respectively:

$$t_{layer}^{i=2} = t_{step} + (1 - f)t_{layer}^{i=1} = t_{step} + (1 - f)t_{step} \quad (34)$$

$$t_{layer}^{i=3} = t_{step} + (1 - f)t_{layer}^{i=2} = t_{step} + (1 - f)t_{step} + (1 - f)^2 t_{step} \quad (35)$$

If the number of layers is large then the layer thickness of i^{th} layer in Equations (33) - (35) can be considered as a sum of infinitely geometric series with the coefficient t_{step} and the common ratio $(1 - f)$. In this case, the layer thickness of the i^{th} layer can be found by Equation (36):

$$t_{layer}^i = t_{step} \frac{(1 - f)^i - 1}{(1 - f) - 1} \quad (36)$$

For any metallic powder, we assume that $f = \frac{\rho_{powder}}{\rho_{solid}} < 1$. Thus, the geometric series converges to an absolute value since the common ratio is less than 1. The converged value is the stationary layer thickness during the LPBF process as given by Equation (37):

$$t_{layer}^{stationary} = \lim_{i \rightarrow \infty} t_{step} \frac{(1 - f)^i - 1}{(1 - f) - 1} = \frac{t_{step}}{f} = \frac{t_{step}}{\frac{\rho_{powder}}{\rho_{solid}}} \quad (37)$$

4.2.2 Generated layer analysis

As was derived in Equation (37), the stationary layer thickness during LPBF is from the density of the powder bed formed during recoating $t_{layer}^{stationary} = f \left(\frac{\rho_{powder}}{\rho_{solid}} \right)$. Riener et al. [159] experimentally investigated the powder density of layers formed in the LPBF machine. The authors found that for the spherical gas-atomized powder with the characteristic listed in Table 9, layer density was 44.2 %. Based on the close properties of utilized NiTi powder as compared to the data from [159], the layer density was chosen in accordance with Riener's experimental results.

Table 9. Comparison of powders for layer density analysis.

Reference	Reiner et al. [159]	NiTi powder (Section 3.1)
Bulk density, %	52	53
Tap density, %	61	60.7
Hausner ratio	1.173	1.145
d10, μm	19	17.4
d90, μm	61	57.7
Flowability	50° (Avalanche method)	18.5s/50 g (Hall method)

where Hausner ratio = $\frac{\text{Tap density}}{\text{Bulk density}}$.

For the simulation of the powder layer, the experimentally obtained PSD was used (Section 3.1, Figure 9) for the powder bed simulation. The 3D rendered results of generated layers are presented in Figure 35a,b.

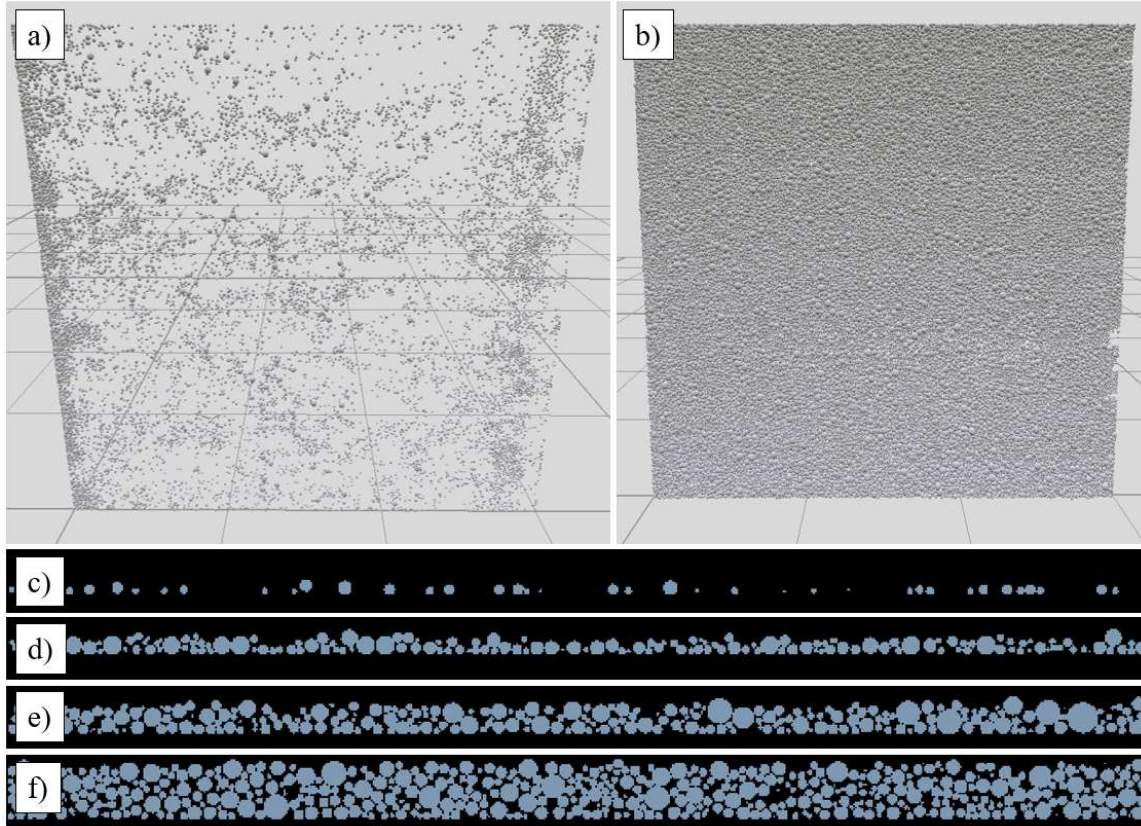


Figure 35. Generated powder bed: isometry of a) 30 μm , b) 45 μm ; cross-sections of c) 30 μm , d) 45 μm , e) 60 μm , f) 100 μm .

PSD of the formed powder bed with 45 μm layer thickness was calculated for various z positions with a 5 μm step. The resulting distributions are given in Figure 36 as a volume fraction dependence from specified particle sizes. All particles with a size below d_{50} were placed in the lower part of the powder layer. The most uniform PSD close to the Gaussian form was detected at 17.5 μm which is below the middle height. Finally, the highest z positions of 37.5 and 42.5 μm include only coarser particles close to d_{90} . Thus, after recoating blade movement the granular system was redistributed from random positions and rearranged itself. As far as PSD of raw powder had relatively a narrow span (Section 3.1), an increase in layer density due to the filling of voids by finer particles was observed only at lower heights.

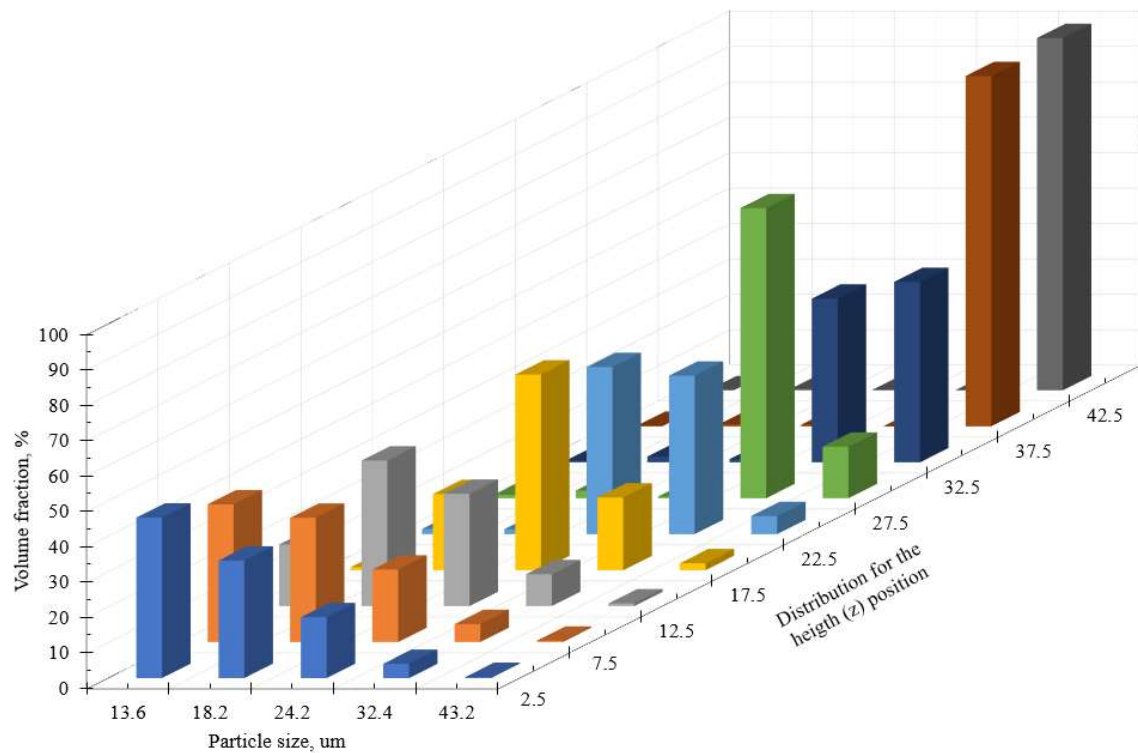


Figure 36. Particle size distribution along the z-axis.

4.3 Single tracks calculations and experimental convergence

Cross-sections of the single tracks had both sharp and spherical shapes indicating the appearance of both keyhole and conductive mode melting. The process conditions of the experiment described in Section 3.2 were used for the mesoscale simulations.

Calculated morphologies of the melt pools are presented in Figure 37 as a temperature field with isothermal surfaces, where purple represents a solidified metal, and blue is a domain without melting. The simulated shapes of the melt pool are compared with experimentally obtained cross-sections of the single tracks described in Section 3.2. The morphology of the resulting single track is highly sensitive to the enthalpy of the process. It is noted, that the correct depth and width of the melt pool can be simulated when the overall shape may differ [101].

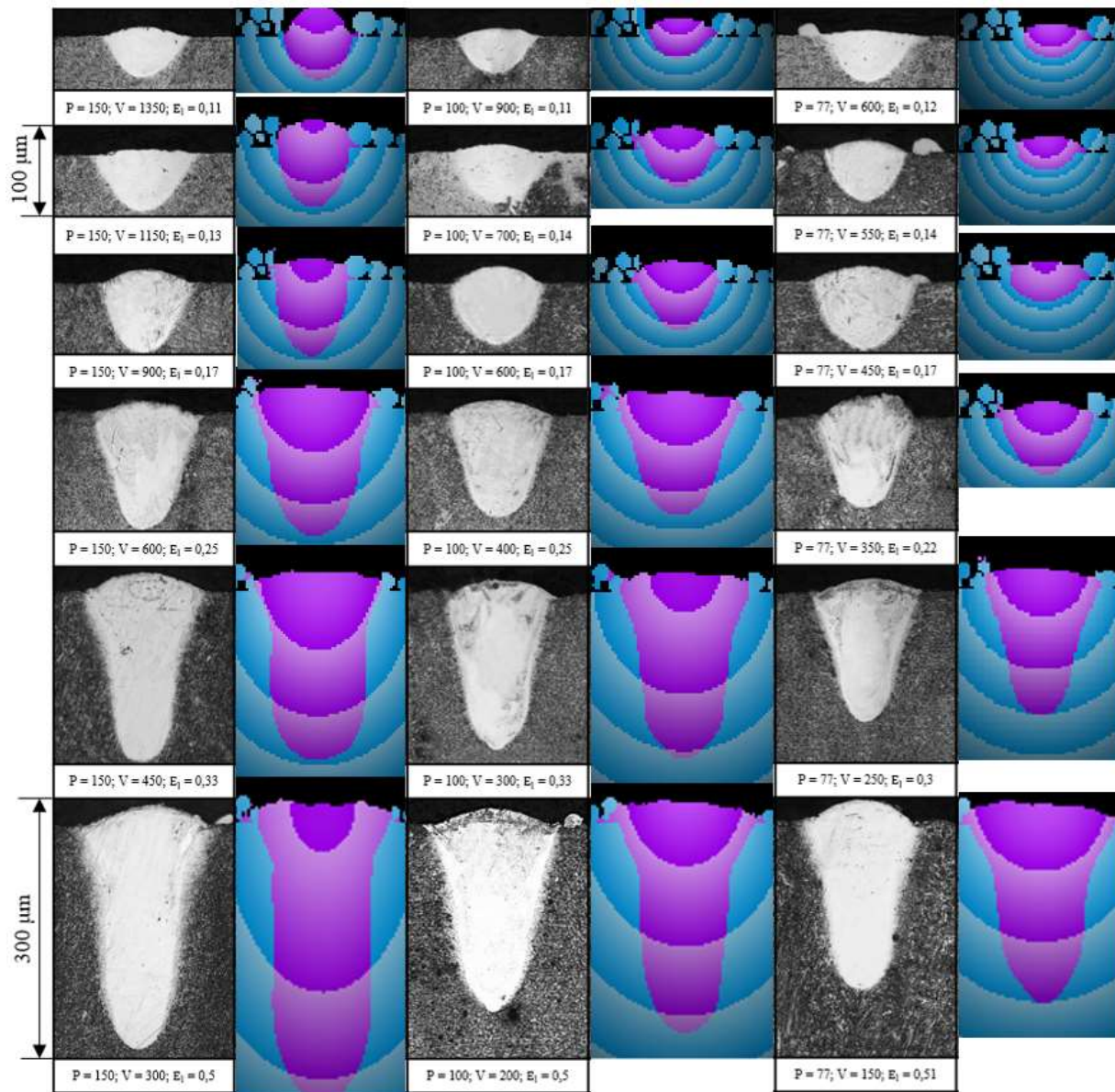


Figure 37. Calculated and experimentally obtained the transverse melt pool's shape.

The resulting melt pool shapes are divided into conductive and keyhole modes according to their experimentally measured depth-to-width aspect ratio. From the evolution of the melt pool shape and temperature field, it can be seen that a necessary condition for the appearance of keyhole mode is an increase in the temperature at the center of the laser's influence, up to the boiling point. This phenomenon is associated with the fluid dynamics effects arising in the melt pool. The surface tension of metal tends to minimize the surface area of liquid metal, and the surface tension temperature dependence is inversely proportional for liquid metals. As discussed, due to thermal gradients caused by non-uniform power density distribution on the surface, the fluid will transfer from the laser

beam's center to the edges of the melt pool. In addition, the gasification recoil force acts along the normal vector to the surface of the melt pool, pushing the liquid into the depth [160]. This force is proportional to the temperature and increases exponentially. As a result of the superposition of the stated forces, the morphology of the depression zone is formed. At high temperatures, the pressure force prevails over the Marangoni effect, causing the melt pool to be sharp and deep. The opposite is observed at lower temperatures, where the surface tension effect dominates, making the melt pool more spherical and wider [101].

Morphologies of single tracks were compared in Figure 38. It was observed that the deformation of the upper surface is higher in the case of a lower linear energy density. Such morphology was also obtained in the experiment due to the retraining of the powder to the melt pool. However, the morphology of simulated single tracks for a high linear energy density ($E_l \geq 0.3$) was represented by a ripple pattern inherent to the welding process. On the contrary, the upper surface of experimentally obtained single tracks had even higher curvature compared to lower linear energy density. The aforementioned difference is prescribed to the pronounced effect of powder denudation. Matthews et al. [161] showed that the mechanism of denudation zone formation during LPBF for the high ambient pressure is connected with Bernoulli-effect-driven gas flow. During the vaporization of metal at the center of the laser's influence, a metal jet appears. This vapor flow causes an inward ambient gas flow, entraining the closest particles into the melt pool. Thus, with an increase in energy input the denudation zone growth and introduces more material to the liquid. Since the simulation assumed zero displacement condition for the powder bed, only the particles that were in direct contact with the liquid domain were introduced into the melt pool. Such a behavior is valid for the conductive mode melting ($E_l \leq 0.17$) due to the following reasons. Firstly, the overall gas convection is significantly lower in the absence of a vapor jet due to the decrease in the temperature gradient. Secondly, the powder has a lower possibility to entrain into the melt pool as the lifetime of the liquid is shorter before it solidifies.

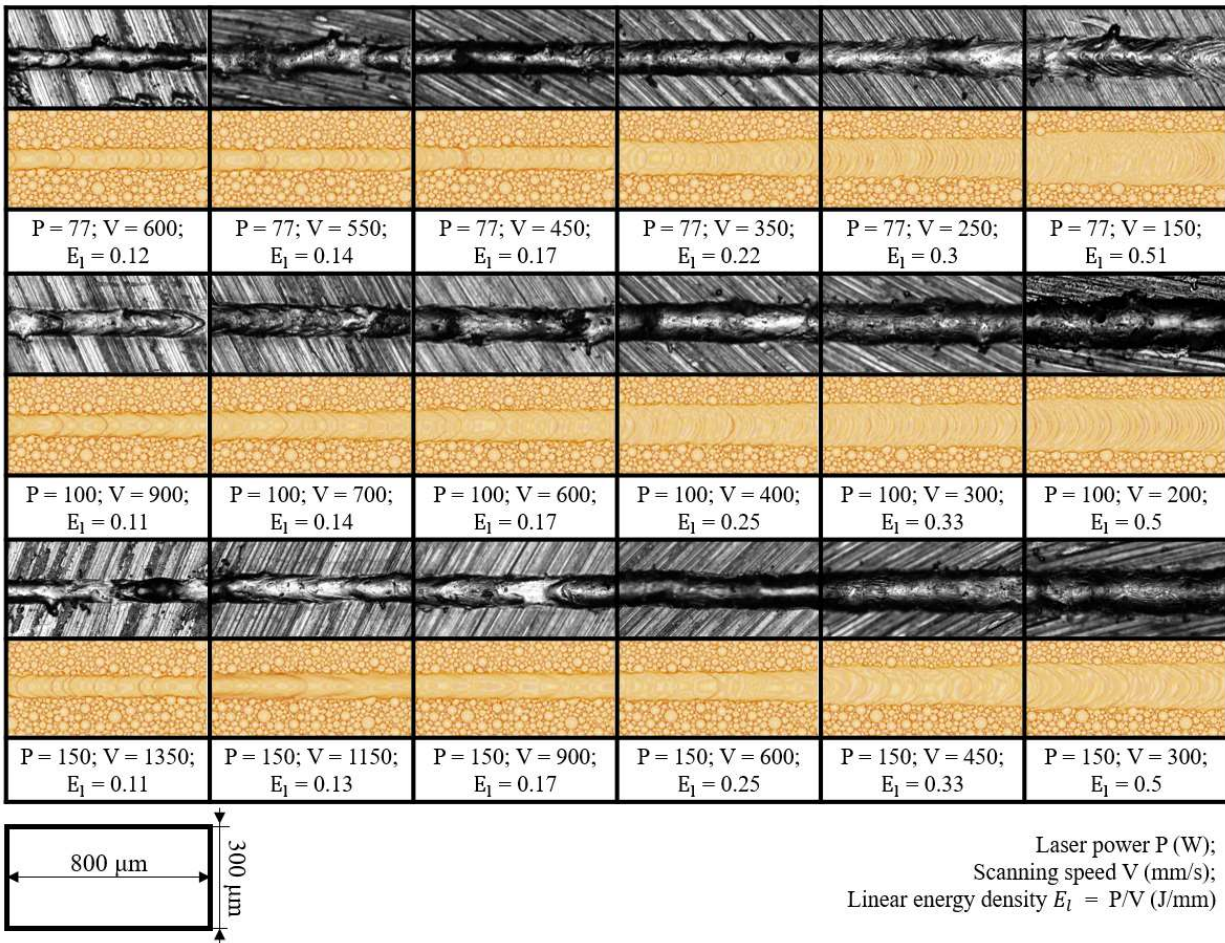


Figure 38. Calculated morphology and experimentally obtained top views of single tracks.

In the production of parts via the LPBF method, an insufficient energy input leads to defects—represented as closed pores with remaining powder—due to lack of fusion, which strongly impairs the mechanical performance of a part [43]. On the other hand, an excessive energy input will lead to the formation of spherical pores due to the solidification of the melt pool with captured gas bubbles [42]. In addition to the aforementioned defects, the following constraints must also be considered for the manufacturing of NiTi via LPBF. Firstly, the increase in energy density input is undesirable due to the increase in pick-up of impurities during consolidation from the surrounding atmosphere [47]. It should be noted that despite the process being carried out in an airtight chamber filled with inert gas, the pick-up of oxygen, nitrogen, and carbon cannot be fully avoided. As a matter of fact, an increase in the content of impurities above 500 ppm is unacceptable for medical applications, according to the established ASTM F2063-05 standard. Secondly, the metal vapor jet in the melt pool results in nickel-depleted chemical composition, since the

evaporation temperature of nickel (3186.15 K) is lower than that of titanium (3560.15 K) [162]. Consequently, the martensitic phase transition temperature is shifted to higher values, obstructing the manufacturing of pseudoplastic parts. Furthermore, crack generation has a higher tendency to appear in the case of higher temperature gradients, due to the relatively low thermal conductivity coefficient of nitinol. In [44], pre-heating up to 500 °C was shown to achieve more dense parts and prevent crack formation. The developed model can be used for predicting thermal behavior during LPBF in order to accomplish the above-stated constraints.

The comparison between the simulated and experimentally obtained melt pool dimensions is presented in Figure 39. Despite the overall convergence, several regimes have deviations for the following reasons. Firstly, for intermediate energy inputs (P150V900, P100V700, P77V450) the transition from conductive to keyhole mode is observed. If deposited energy to the material domain is just enough to start evaporation, the deformation of the liquid surface develops. In the depression zone, fewer rays reflect back as it is in the conductive mode, therefore, multiple reflections appear inside the melt pool. As a consequence, the absorption of laser energy in the depression zone significantly increases. As far as this process is concerned, the transition is highly unstable and nonequilibrium, therefore, convergence is hard to achieve. Secondly, the depth of the melt pool was overestimated for regimes with the highest linear energy density input. The deviation is attributed to a lack of data on the temperature dependence of the absorption coefficient for NiTi. As it shown, the utilized absorption coefficient limits the convergence by severe keyhole appearance.

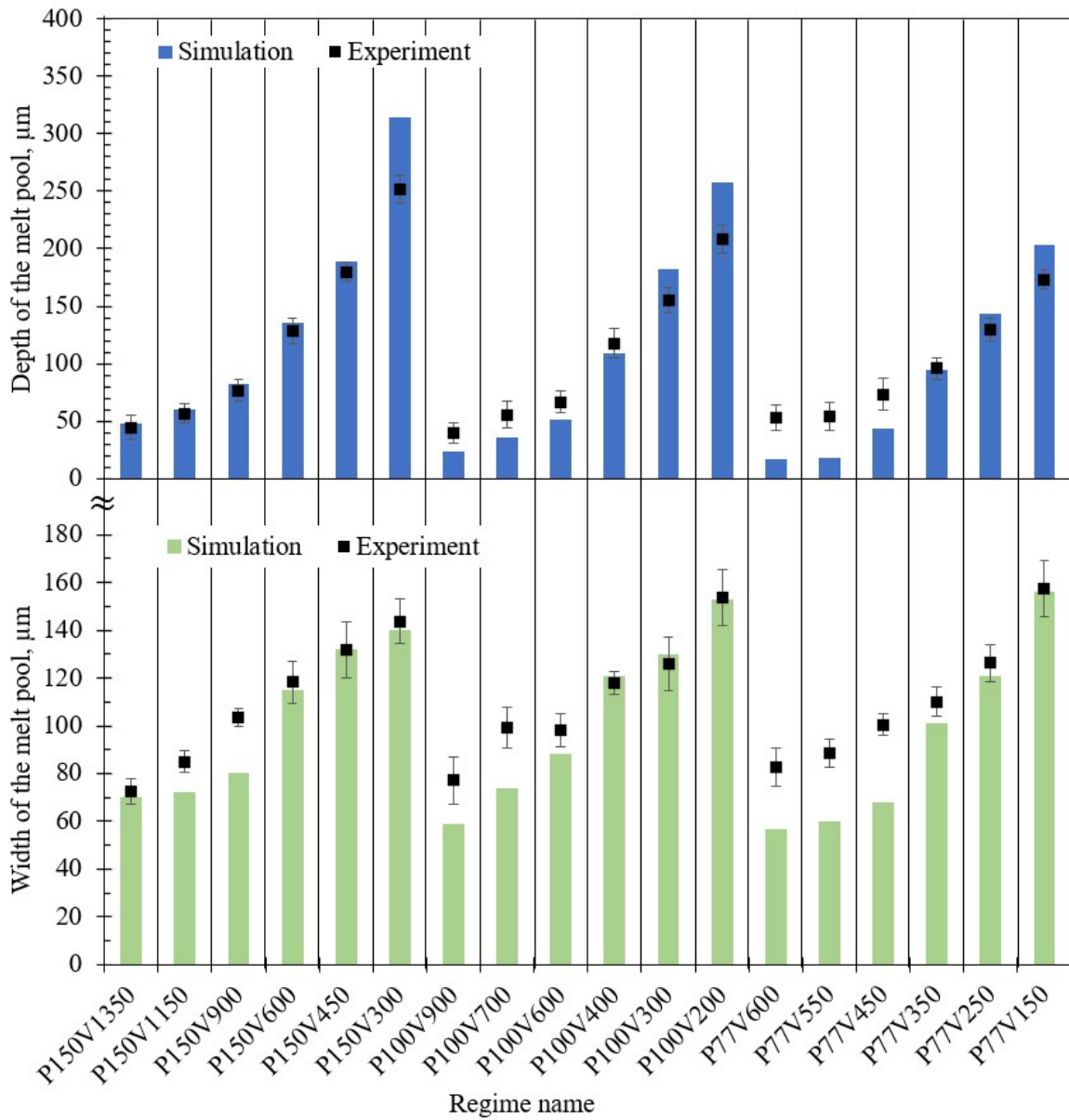


Figure 39. Validation of the model by width and depth of the melt pool for all regimes.

4.4 Effect of the surface tension on the melt pool formation

To evaluate the effect of the surface tension on the melt pool formation, two simulations were carried out. In Figure 40, typical results of the melt pool simulation are depicted for the $\gamma = 2010$ mN/m and $\gamma = 1530$ mN/m. Simulations were conducted in KiSSAM software discussed in Sections 1.3 and 4.3. All other parameters utilized for the model were constants for both cases, involving $\frac{d\gamma}{dT} = -2.6e-4$ N/m/K. It should be noted that the considered values of surface tension refer to the temperature of the conducted

experiment (1603 K). Thus, the reported values of thermodynamic calculations from [153] were extrapolated with above-mentioned temperature coefficient which is consistent with the reported temperature dependence of the surface tension. The graph shows that the vorticity increases slightly in the case of a higher surface tension. However, the overall pattern of color-coded streamlines and morphology of the melt pool were not changed.

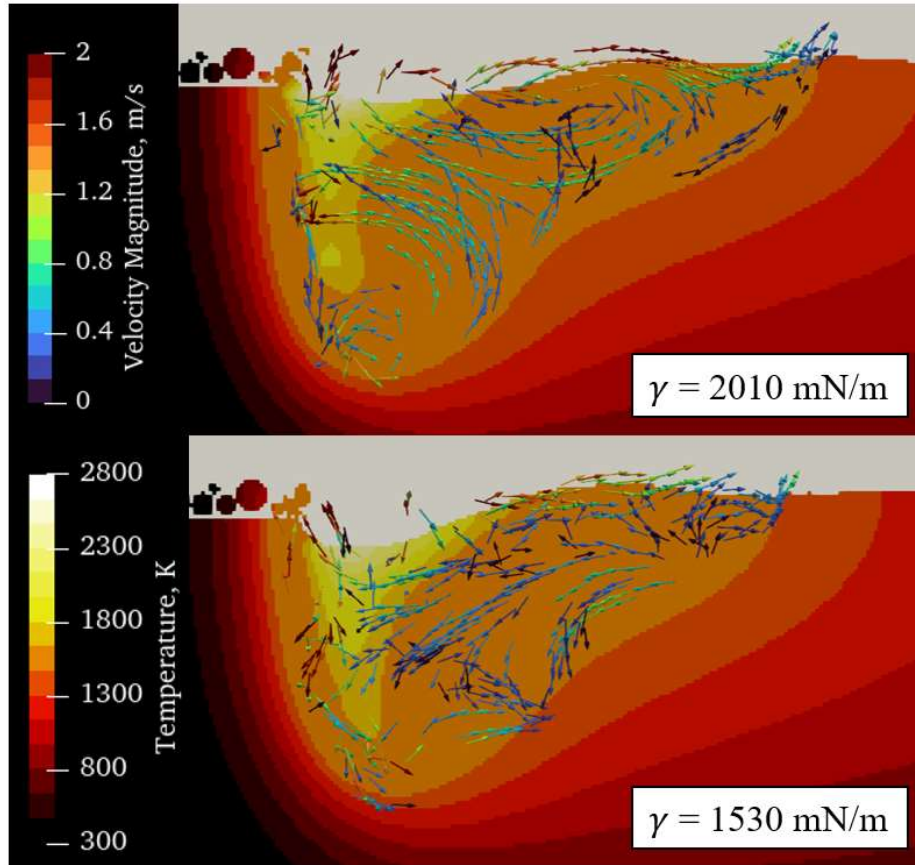


Figure 40. Calculated temperature field with velocity vectors, color-coded by magnitude for different surface tension values at the same time step.

In Figure 41 normalized frequency distributions of the velocity magnitude for the liquid for both calculations are presented. In other time steps the distribution of the velocity magnitude showed the same trend. It is known, that the gradient of temperature or concentration is considered the main driving force of thermo-capillary convection [45]. However, the numerical experiment demonstrated that the increase of surface tension leads to fluid flow acceleration in the liquid domain despite the same $\frac{dy}{dT}$. It is assumed that higher surface tension may result in increased curvature of the surface with a higher specific surface area. As a consequence, the liquid domain experienced a higher tendency for the

development of Marangoni convection. Overall depth and width of the melt pool increased by 2.8 % with an increase in surface tension. Such changes are considered insignificant for the LPBF simulation problem.

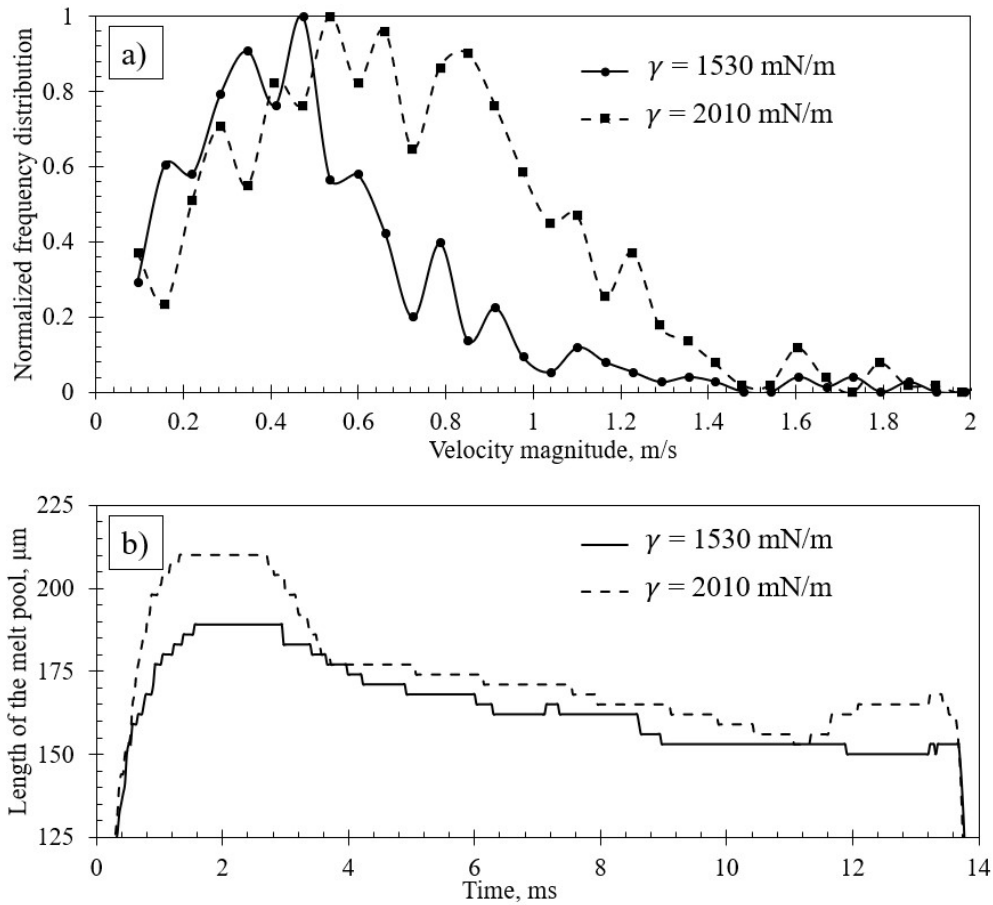


Figure 41. Normalized frequency distribution of velocity magnitude extracted from the velocity field.

4.5 Simulation of thin walls consolidation

Several probes were placed in the domain for thermal history tracking in particular points. For further analysis, a probe with coordinates (1, 1.5, 2) in mm was used. The placement of the probe corresponds to the center of the track in x and y directions, and the substrate height in z direction. Typical thermal history is demonstrated in Figure 42a and Figure 42b for the regimes with high and low linear energy input respectively. Each layer of simulation started with ambient temperature for the whole domain assuming complete cooling during the experiment. The actual measured time between adjacent layers during the consolidation of thin walls was 50 s, which confirms the validity of this assumption.

Each curve represents an immediate temperature growth during laser influence and gradual cooling with the appearance of a distinctive plateau during crystallization at the temperature of solid/liquid phase equilibrium. The material at the probe location was remelted seven times, and during the consolidation of the next layers was in the Heat Affected Zone (HAZ) up to two times.

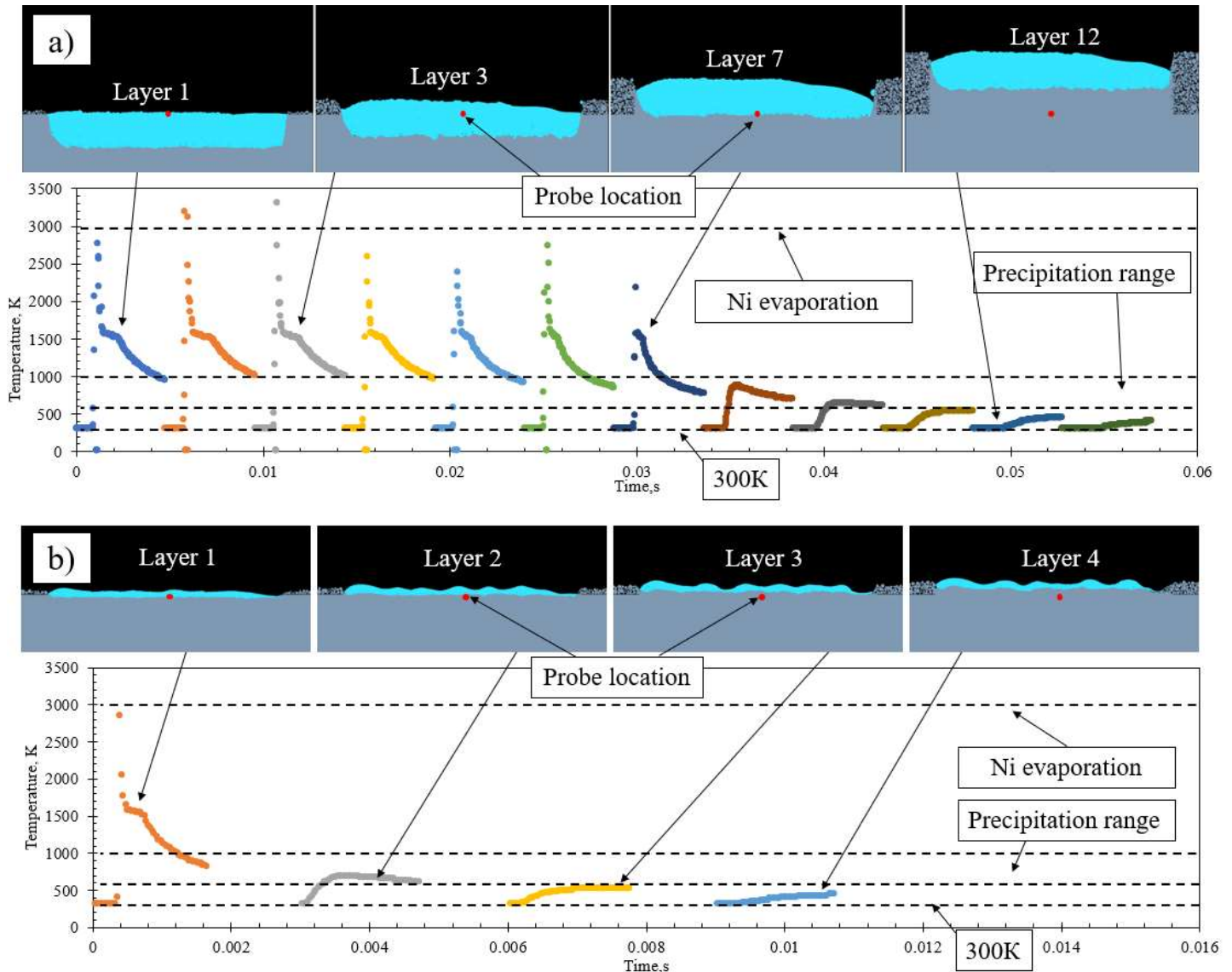


Figure 42. Thermal history analysis for thin wall processed with a) P150V300 regime, and b) P150V1350.

It was demonstrated that the necessary condition of keyhole mode melting is exceeds the boiling point of the Ni. For laser powers of 77 W, 100 W, and 150 W the scanning speed thresholds are 150 mm/s, 300 mm/s, and 600 mm/s, respectively. For the laser power of 50 W, only conduction mode melting was observed in the studied scanning

speed interval—from 450 mm/s to 100 mm/s. The appearance of the keyhole mode resulted in a deeper and sharper melt pool, with an experimentally measured depth-to-width ratio greater than 1.

Based on the experimental investigation of the melt pool dimensions and morphology, along with simulation, it was shown that the optimal process parameters can be ascertained. In this study, the optimal regime of LPBF for NiTi was found $P = 100$ W, $V = 850$ mm/s, and $t = 20$ μm .

4.6 Multicomponent evaporation and Ni depletion

To take into account the difference in evaporation kinetics for Nickel and Titanium in NiTi melt, the multicomponent model should be considered. Partial pressures control the behavior of each individual component in the melt. Activity is widely used for non-ideal solutions to express the partial pressure as given in Equation (38) [163]. It should be noted that a composition of near-equiatomic NiTi phase concentration of Nickel is mainly used. For convenience, all thermodynamic functions are expressed for Nickel, unless otherwise specified.

$$p^{Ni} = a^{Ni} p_S^{Ni} = \gamma^{Ni} \chi^{Ni} p_S^{Ni} \quad (38)$$

where p is partial pressure, a is activity, γ is activity coefficient, χ molar fraction, and p_S is saturated pressure. According to Dalton's law the total pressure of the solution will be equal to the sum of the partial pressures for each component. In order to find the partial pressures for each component experimental data on the activity coefficient can be used. However, due to a lack of experimental data for a wide temperature range, the activity coefficient can be found by thermodynamical calculations of the excess Gibbs free energy. The partial Gibbs free energy for Ni and Ti with respect to Ni molar fraction can be found using expressions (39) and (40) respectively.

$$\Delta G^{Ni} = \Delta G + (1 - \chi^{Ni}) \frac{\partial \Delta G}{\partial \chi^{Ni}} \quad (39)$$

$$\Delta G^{Ti} = \Delta G - \chi^{Ni} \frac{\partial \Delta G}{\partial \chi^{Ni}} \quad (40)$$

The total Gibbs free energy ΔG is calculated using the Redlich-Kister approximation [164] given in Equation (41).

$$\Delta G^{Ni} = \Delta G + (1 - \chi^{Ni}) \frac{\partial \Delta G}{\partial \chi^{Ni}} \quad (41)$$

For the calculation of partial Gibbs free energy mixing parameters was used that were optimized in works by Santhy [165] and Kajikawa [166]. Thus, partial Gibbs free energies for Ni and Ti can be calculated via Equations (42) and (43) respectively.

$$\Delta G^{Ni} = (1 - \chi^{Ni})^2 \left(\sum_{n=0}^i L_{NiTi}^{(n)} (2\chi^{Ni} - 1)^n + 2\chi^{Ni} \left(L_{NiTi}^{(1)} + 2L_{NiTi}^{(2)} (2\chi^{Ni} - 1) \right) \right) \quad (42)$$

$$\Delta G^{Ti} = (\chi^{Ni})^2 \left(\sum_{n=0}^i L_{NiTi}^{(n)} (2\chi^{Ni} - 1)^n - (1 - \chi^{Ni}) \left(L_{NiTi}^{(1)} + 2L_{NiTi}^{(2)} (2\chi^{Ni} - 1) \right) \right) \quad (43)$$

Where $L_{NiTi}^{(n)}$ denotes temperature-dependent mixing parameters for liquid NiTi melt. All mixing parameters for the Redlich-Kister power series are given in Table 10.

Table 10. Utilized sets of mixing parameters.

Mixing parameters	Set 1	Set 2
$L_{NiTi}^{(0)}$	$-153707 + 34.8594T$	$-160490 + 4.74T$
$L_{NiTi}^{(1)}$	$-81824.8 + 25.8099T$	$-73902 + 28.23T$
$L_{NiTi}^{(2)}$	$-10.0779T$	$+16.51T$
Reference	Santhy [165]	Kajikawa [166]

The calculated Gibbs free energies, activity coefficients, and activities are presented in Appendix A as dependences from NiTi alloy composition for various temperatures with a 500K step.

In Figure 43 distributions of Nickel for low and high linear energy regimes. Substrate and powder appeared red on the color-coded map, since the Ni content for the

powder and substrate was set to 55 mass. %. On the other side, the pores caused by a lack of fusion in thin walls are displayed with blue. According to Figure 43a, no change in the Ni/Ti ratio was observed. It is attributed to a fully conductive mode of melting when laser energy input is not enough to exceed the latent heat of vaporization. Thus, only diffusion evaporation may appear, however, due to the short time of melt pool existence such mechanism was not taken into account. The distribution of Ni for high energy density (Figure 43b) is completely different. It can be seen that the last layer has a slightly higher Ni/Ti ratio than the previous layers due to the multiple remelting. Furthermore, some track boundaries can be distinguished as a liquid domain with intensive mixing appearing in the keyhole mode of melting.

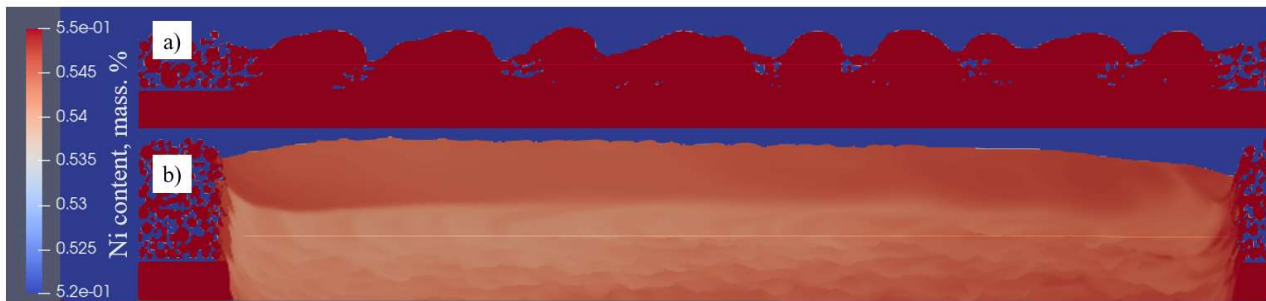


Figure 43. Distribution of Ni in thin wall consolidated with regimes a) P50V1000, b) P150V500

The results of calculated Ni content after thin wall consolidation are presented in Figure 44. A positive deviation from linear energy density is observed for all samples (Figure 44a). However, for a group of samples consolidated with a laser power of 50 W the evaporation dynamics is significantly lower. Such behavior correlates with observation of the melt pools' morphologies (Section 3.2.2, Figure 13). For the cases with higher laser power, an almost similar dependence from the linear energy density is obtained. Thus, according to the simulation results, the evaporation kinetics is dependent not only on LED but also on the laser power.

The resulting Ni content after the LPBF can be calculated by taking into account the initial chemical composition of the NiTi raw powder (Section 3.1) and calculated Ni loss. It is shown that the experimentally measured temperature of the martensite phase transformation (Section 3.5, Table 6) has a linear dependence from calculated Ni concentration after the thin wall simulation (Figure 44b).

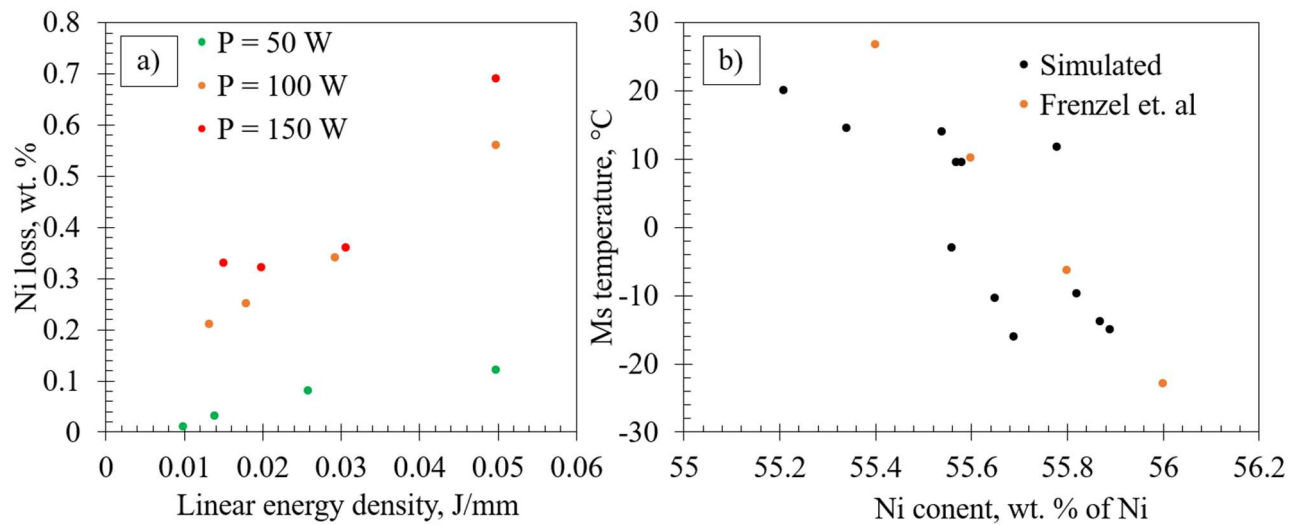


Figure 44. a) dependence of calculated change in Ni content from linear energy density, b) dependence of experimentally measured martensite start transformation temperature from calculated Ni content. Frenzel et. al [22].

The overall trend correlates with pioneer works dedicated to studies of Ni content influence on the martensitic phase transformation provided in works [22,167]. However, there are multiple points that deviate from the linear trend. This is attributed to the effects of the resulting phase composition and microstructure. It should be noted that both effects can be simulated simultaneously and considered for future work to precisely estimate the resulting functional properties of NiTi alloy after the LPBF procedure.

Chapter 5. Endodontic files manufacturing via high-resolution LPBF

The introduction of rotary instruments into the protocol of mechanical root canal preparation has changed the idea of clinical endodontics. During the irrigation and cleaning procedure, the inner walls of the tooth canals undergo an abrasive effect induced by special instruments called files. However, for proper preparation of the irregular-shaped canals with conventional files, endodontists were obliged to significantly expand the canal which resulted in dentin removal. In 2013, a Self-Adjusting File (SAF) made of Nickel-Titanium alloy was introduced, which provided completely new possibilities for minimal invasive endodontic treatments [168,169]. The drawings of SAF are presented in Figure 45a-d. Due to the superelastic properties of the nitinol and the peculiar design of SAF, the shape of the file adapts to the patient's tooth canal, which allows the preparation of irregularly shaped canals [169,170]. At the moment, NiTi files are made by laser cutting of hollow tubes. This chapter describes the possibility of manufacturing SAF using the additive manufacturing (AM) approach.

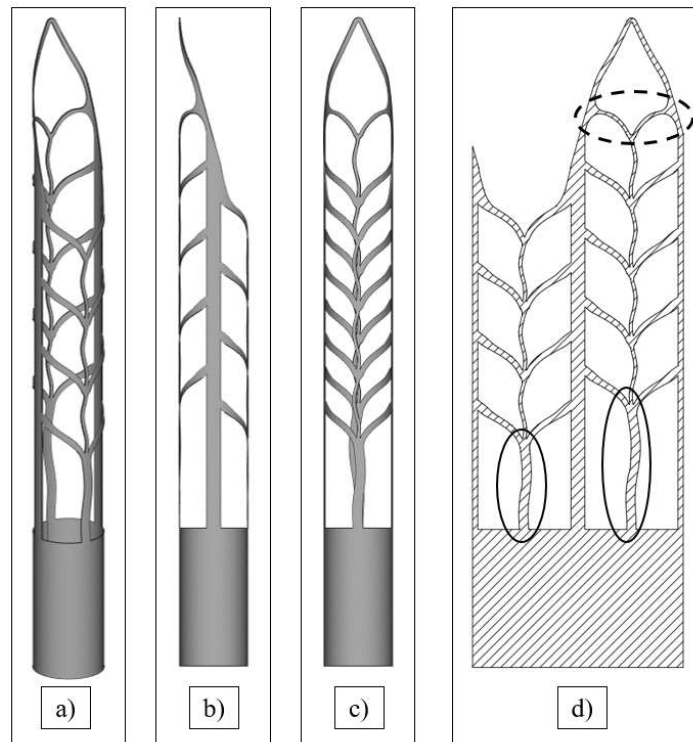


Figure 45. 3D-model of Self-Adjusting File adopted for LPBF manufacturing: a) isometry; b) XZ plane view; c) YZ plane view; d) sweep of the SAF, supplemental support strut highlighted with a solid line, critical inclined angle highlighted with a dashed line.

5.1 Regime optimization for file manufacturing

Figure 46 summarizes the results of Sections 3.3, 3.4.1, and 3.5 which include experimental data on the thin wall thicknesses, mechanical tests, and temperatures of the phase transformation, respectively. The obtained P-V diagram of the LPBF process conditions has three limitations. Firstly, from the high scanning speed side, the window is restricted by poor ultimate strength. As was shown in Sections 3.4.1 (experimentally) and 4.6 (numerically), an insufficient energy input to the volume of powder resulted in a lack of fusion defect with subsequent pores generation. Such pores provide favorable conditions for crack propagation and brittle failure with low elongation to fracture. The overall red area of the diagram corresponds to the regimes that did not provide a strain of 3 % on the consolidated thin walls samples.

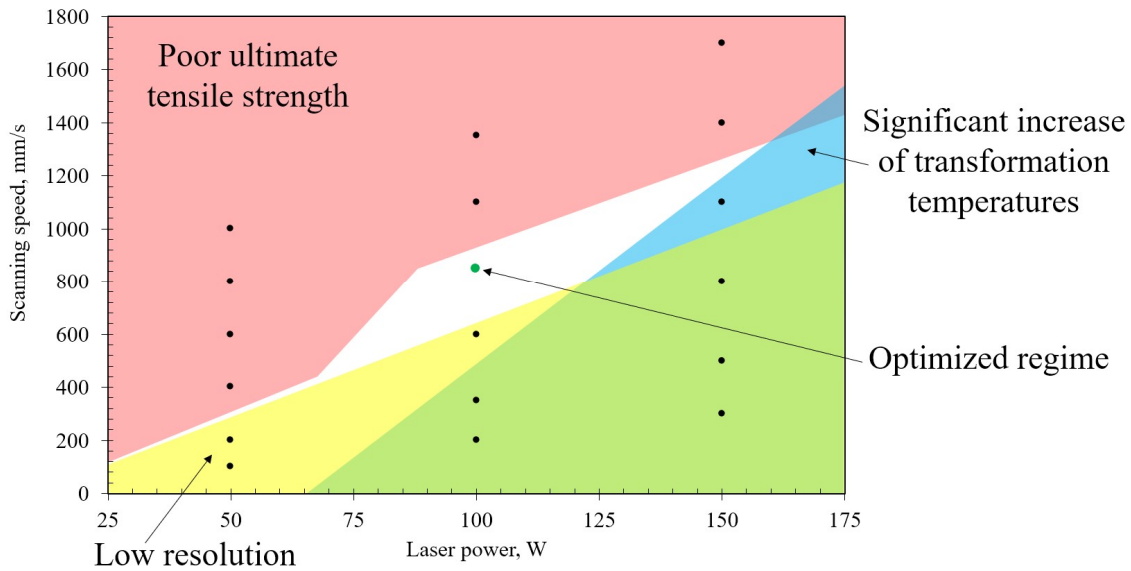


Figure 46. P-V map of high-resolution LPBF process conditions.

Secondly, a low-resolution limitation is marked on the low scanning speed side of the process diagram. As far as the width of the melt pool is growing with the energy input, the minimum feature size that can be manufactured decreases. It should be noted that despite the rapid augmentation of the melt pool depth during the transition to the keyhole mode melting, the dependence of the width from the energy input remains monotonous (Figure 17 and Figure 39). However, the width of thin walls under different inclined angles (25 – 45 °) is also significantly affected by the remelting depth. Therefore, the indicator of “low resolution” corresponds to the average width of the inclined thin walls (Figure 18) and correlates with the minimum feature size that can be manufactured. The indicator was set

to 150 μm and can be modified depending on the problem of interest. Finally, the effect of the shift in the characteristic temperatures of the martensite phase transformation should also be taken into account for NiTi alloy. The third limitation referred to an increase in TTs by more than 15 $^{\circ}\text{C}$ according to the measurements by DSC (Figure 26 and Table 6), which is significant for the files' production technology. In conclusion, the optimization procedure was demonstrated by multiple techniques that affect the quality of SAF files. In the following section, for the validation of the optimization technique samples of SAF files were manufactured in a narrow window of the process parameters but not only with an optimal regime.

5.2 SAF manufacturing via high-resolution LPBF

The SAF samples were manufactured with various levels of laser power and scanning speed. The corresponding matrix in the P-V coordinates is presented in Figure 47a. The obtained samples are subdivided by their regime into successful fabrication, failure, and low resolution. The SAF samples on the NiTi substrate after the LPBF consolidation are presented in Figure 47b. Samples P50V400, P100V1100, and P150V1400 were highly distorted and disconnected in the most inclined struts marked in Figure 45d with a dashed line. The inclined angle of the struts reaches a minimum of 24° in this place. This results in good agreement with the preliminary study of the single track thin walls (Section 3.3).

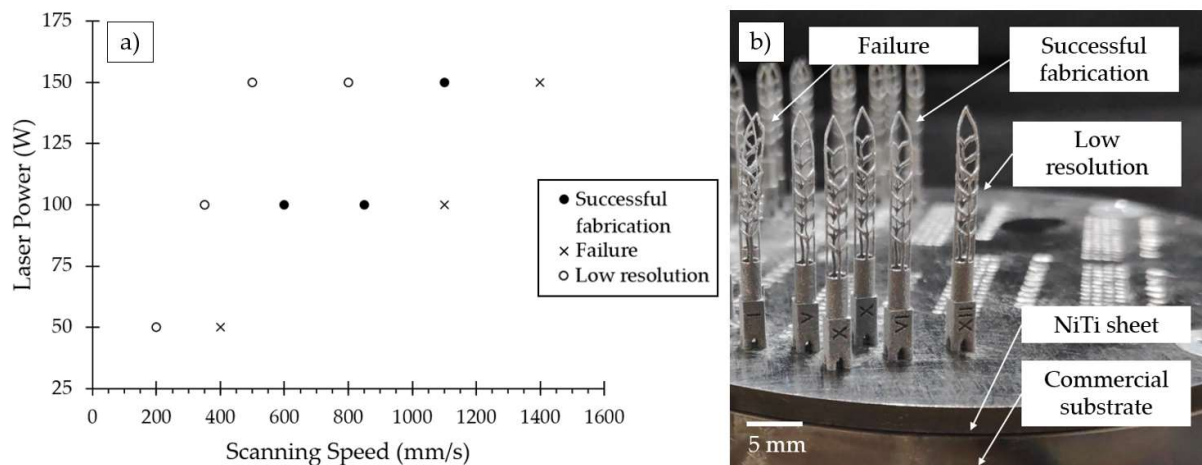


Figure 47. a) Matrix of LPBF regimes of Self-Adjusting files fabrication; b) Produced samples of SAF.

SEM images of 3D-printed SAFs manufactured with regimes P100V850, P150V1100, P100V400, and P50V200 are shown in Figure 48. As a criterion for the low-resolution regimes, SAF samples with a strut diameter over 150 μm in the upper part were considered. It should be noted that with a minimum laser power of 50 W, the desirable resolution was not achieved despite resemblant values of linear energy density for other cases. Such a trend can be related to a reduced scanning speed and an increased melt pool lifetime as a consequence. The kinetics of powder denudation and particle retraction into the melt pool will be highly affected. The agglomerates appeared within the regimes with low scanning speed and fused to the struts of the SAF samples can be seen in Figure 48c,d.

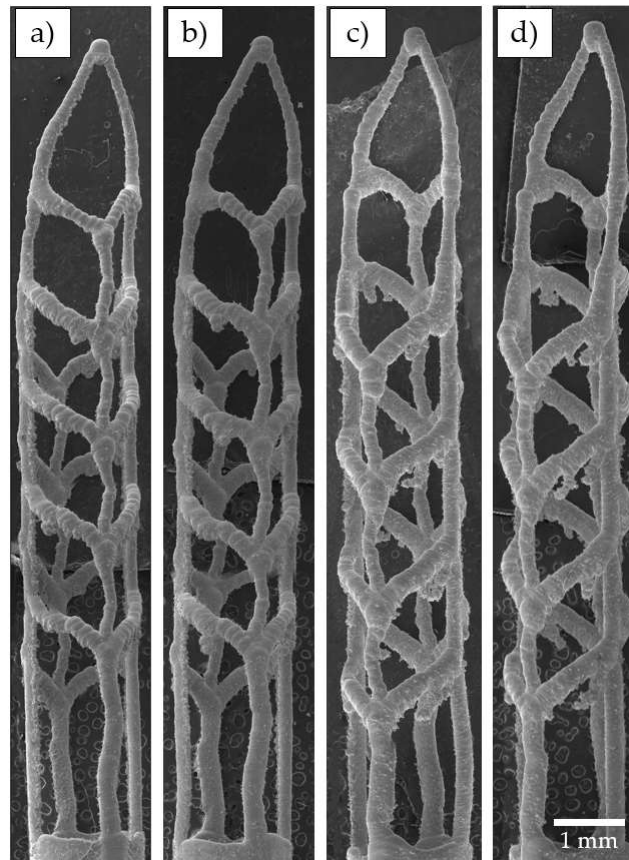


Figure 48. 3D-printed SAF samples fabricated with various regimes: a) P100V850, b) P150V1100, c) P100V400, d) P50V200.

In Figure 49 SEM images of the upper part of the P100V850 SAF sample are presented at different magnifications. The tip region shown in Figure 49a,b accumulated the highest deviations from the prescribed SAF design. The thickening not presented in the 3D model (see Figure 45a) occurred on the printed sample because of the quasi-continuous laser mode which does not allow to production of a single pulse of laser energy in the point.

However, such thickening does not affect the SAF performance (abrasive cleaning). The inherent layering effect can be clearly observed in Figure 49c. Since the SAFs were manufactured on the edge of resolution such a layering effect is inevitable. Besides, fused particles on the SAF surface are presented that are common surface defects [93], but considering the feature size of the objects these defects became more influential. It should be noted that both surface irregularities (layering and fused particles) possibly can be removed by chemical etching [42].

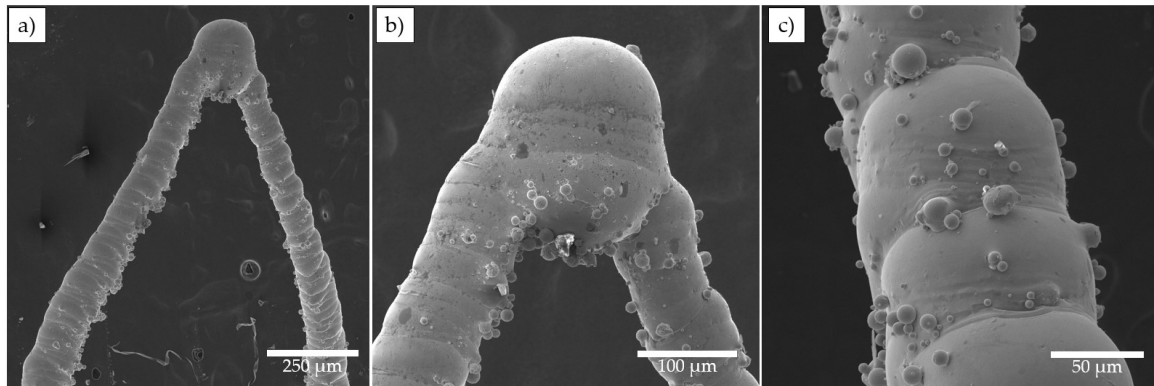


Figure 49. High magnification images of 3D-printed SAF sample P100V850: a) the upper part, b) the tip, c) the strut of the upper part.

5.3 Characterization of SAF Samples

As-built P100V850 sample that was found to be optimal for manufacturing single track SAF files was subjected to the DSC testing and compared with the raw powder DSC results. Figure 50 shows typical DSC curves for raw powder and a cut sample from the file. The exact values of characteristic transformation temperatures were found for reversible martensite phase transition during the heating/cooling cycle and are presented in Table 11. The DSC curves are represented with a single peak that corresponds to the direct cubic-monoclinic B2-B19' transformation without an intermediate rhombohedral R phase. It is seen from Figure 50 that thermal hysteresis of the transition is observed which is typical for NiTi alloys [43].

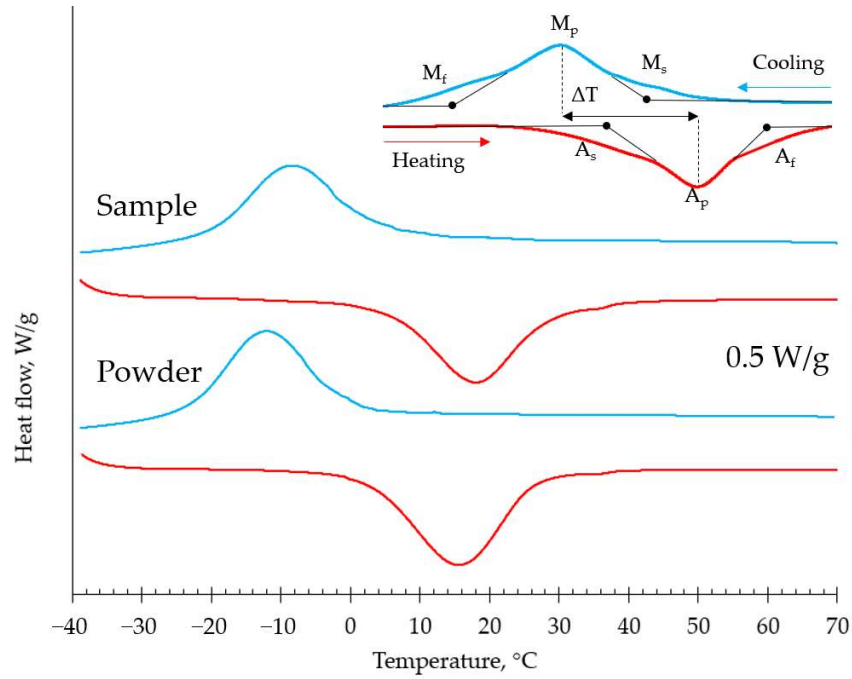


Figure 50. Differential scanning calorimetry for raw powder and sample P100V850.

For the enhanced superelastic response of the NiTi parts, the A_f temperature of the transformation should be below the working temperature by 10 °C [44]. The measured transformation temperatures presented in Table 11 indicate that characteristic temperatures were increased after the LPBF procedure, especially M_s (from -1.1 to 3.8 °C). As far as martensite transformation is sensitive to Ni-content, this shift could occur due to Ni evaporation during laser influence. It was demonstrated in the paper [45] that the hatch distance parameter has the highest influence on the resulting transformation temperatures by means of grain size and orientation. A decrease in the hatch distance led to the finest melt pools due to multiple remelting and intense overlapping. Apparently, the single track strategy manufacturing, on the contrary, may have the lowest impact which is also indicated by the obtained experimental data. Thus, achieving an enhanced superelastic response can be simplified in the micro-objects produced via LPBF by the prescribed approach.

Table 11. Temperatures of phase martensitic transition of initial powder material and fabricated sample.

Sample Name	Transformation Temperatures (°C)						
	M_s	M_p	M_f	A_s	A_p	A_f	ΔT
NiTi raw powder	-1.1	-12.2	-22.8	2.5	15.5	26.3	27.7
P100V850 sample	3.8	-8.5	-20.2	4.7	18.3	29.7	26.8

The X-ray diffractograms recorded at room temperature of raw powder and as-build file are presented in Figure 51. It is seen that the initial phase composition of the powder was represented by the high-temperature B2 austenite phase. After the LPBF process, a few peaks of a low-temperature phase (B19' -martensite) were observed which align well with the found increase of the A_f temperature in the DSC analysis. However, both diffractograms primarily correspond to B2-phase with a typical X-ray peak intensity ratio close to isotropic NiTi alloy: very strong {110}, weak {200}, and medium-strong {211}.

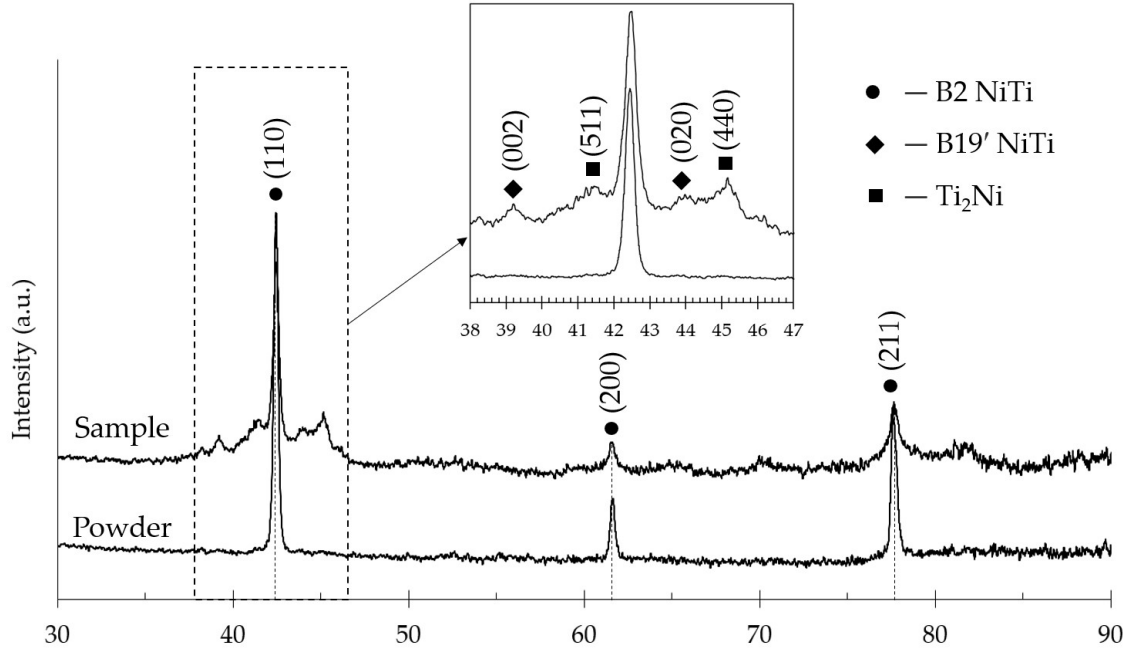


Figure 51. XRD patterns of initial NiTi powder and 3D-printed P100V850 sample.

Despite the amount of martensite phase in the as-built state does not exceed 5% this may lead to irreversible deformations during the loading/unloading loop in the superelastic region. Additionally, small peaks of the Ti_2Ni phase were observed in the low-angle region. The formation of the Ti_2Ni -phase leads to the depletion of the solid solution in Ti and a corresponding decrease in the martensitic transformation temperatures (Figure 50 and Table 11). Thus, the shift of transformation temperatures is a result of several opposite processes' interaction, i.e. Ni evaporation and Ti-rich phase formation.

5.4 Simulation of the layer-wise consolidation for SAF

In this section, developed approach of multilayer mesoscale simulation described in Chapter 4 is utilized for analysis of high-resolution LPBF consolidation of Self-

Adjusting Files. For the numerical study, a square substrate with 3 mm side was created. At the next step, a 3D model of SAF (Figure 45) was sliced with Materialise Magics software using the same process conditions and presets for scanning strategy as was utilized for the experimental procedure (Section 5.2). Coordinates of generated vectors for laser movement were extracted directly from the data file created for the Trumpf TruPrint 1000 by slicing software. Such an approach allowed to establish reliable correlation between the experimental LPBF process and simulation. Layer-wise simulation followed the same protocols as in Chapter 4: generation of powder layer with known PSD of particles, scanning the powder bed along prescribed coordinates, forming the next layer on top of the remelted one, moving of the recoated blade on the height of 45 μm from previous (refer to Section 4.2.1 for layer thickness explanation). For the simulation, 250 layers from the upper part of the SAF were selected as they include a representative part of the whole file. The calculations had been running for 317 hours (~ 13 days), when the average time required for simulation of a single layer was 76 minutes. The simulation was performed on GeForce RTX 3090 (Nvidia, USA).

After the simulation, all residual powder that has not been in contact with the liquid interface was removed with corresponding script. To render the integral geometry, an additional script was applied to activate the cells in the obtained data grid from the previous layers that was not in contact with the melt pool in the last calculation. The rendering of the calculated geometry was implemented in Blender (Open-source, ver. 3.3).

Figure 52 depicts the obtained geometry after the numerical experiment. It worth noting that in comparison with experimentally obtained morphology of the struts (Figure 48), the rendered geometry is extensively covered with powder particles. Such difference is explained by the constrained displacement of the powder during melting. As far as the denudation effect is not taken into account, the powder particles are not entertaining to the melt pool but only fusing to the surface if liquid/solid interface appeared.

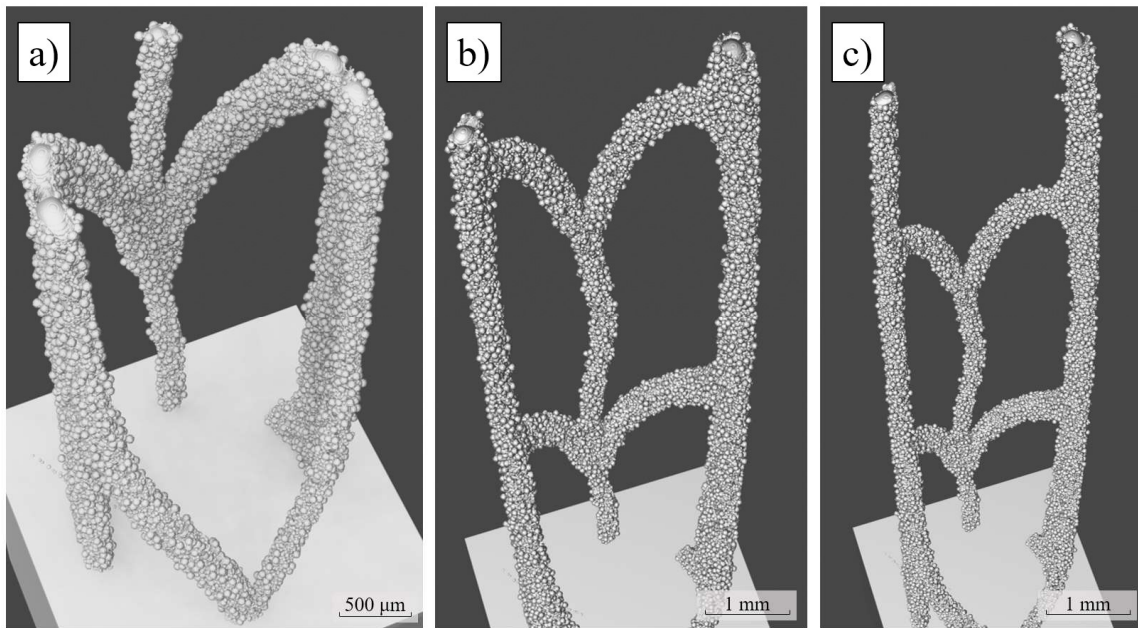


Figure 52. Rendered SAF geometry after simulation: a) layer 1250, b) layer 1350, c) layer 1484.

Such simulation of LPBF process at the mesoscale can be used in the future work for analysis of various technological problems. Firstly, local evaporation calculations at different places of the strut-based devices can be done as it discussed in Section 4.6. Secondly, residual thermal stresses, deformations during relaxation, and geometry discrepancy due to the warping can be analyzed by implementing thermomechanical coupling. Thirdly, the microstructure features can be analyzed by calculations of the solidification grains for the micro-objects. Finally, strut-based and thin-walled structures are often used to obtain lightweight parts, stents, for adaptation of the mechanical properties of the whole part.

Conclusions

In the thesis, the possibilities of manufacturing micro-objects from NiTi shape memory alloy via high-resolution Laser Powder Bed Fusion (LPBF) were studied. It was demonstrated that the functional properties in the as-built state are sensitive to the process conditions. The mechanisms of functional properties altering were studied by mesoscale simulation of the NiTi melt pool during the LPBF process. The results of the thesis can be divided into three main parts. The first part involves the experimental study of single track-based manufacturing of NiTi via LPBF. The second part includes the simulation of the melt pool during LPBF. The third part focuses on the particular application of the technology for manufacturing of NiTi endodontic files.

1. Excluding the hatch spacing by means of single track-based thin walls consolidation allowed to reveal the pure effect of the laser influence on the NiTi functional properties. The samples manufactured with the highest linear energy density (LED) of 0.5 J/mm and highest laser power exhibited a decrease in the characteristic transformation temperatures by 45 °C. On the other side, it was demonstrated that below a critical value of LED almost no change in the transformation temperatures (TTs) appeared in comparison with raw powder. It should be noted that the critical value is individual for each level of laser power. Regimes with a minimal influence on the NiTi functional properties are of interest for the applications with requirements of superelastic (SE) response. However, it was demonstrated that after a significant decrease of LED, poor ultimate strength will limit the performance of such consolidated part. In this regard, when SE response of NiTi is desirable, the optimal LPBF regime presents a compromise.

2. 4D printing feasibility via high-resolution LPBF was implemented experimentally. A thin-walled sample obtained with local variation of LPBF process parameters demonstrated activation of the shape memory effect (SME) at different temperatures without heat treatment. Multistage nature of SME in the as-built sample indicates successful *in-situ* tailoring of NiTi properties via high-resolution LPBF. The control over the SME activation temperature was done in a wide temperature range from -2 to 55 °C. Established relationships between NiTi properties (TTs, irreversible strain, volume fraction of martensitic phase) and the LPBF process conditions create a foundation for production

protocols of NiTi with SE behavior, specific SME activation temperature, or multistage SME activation.

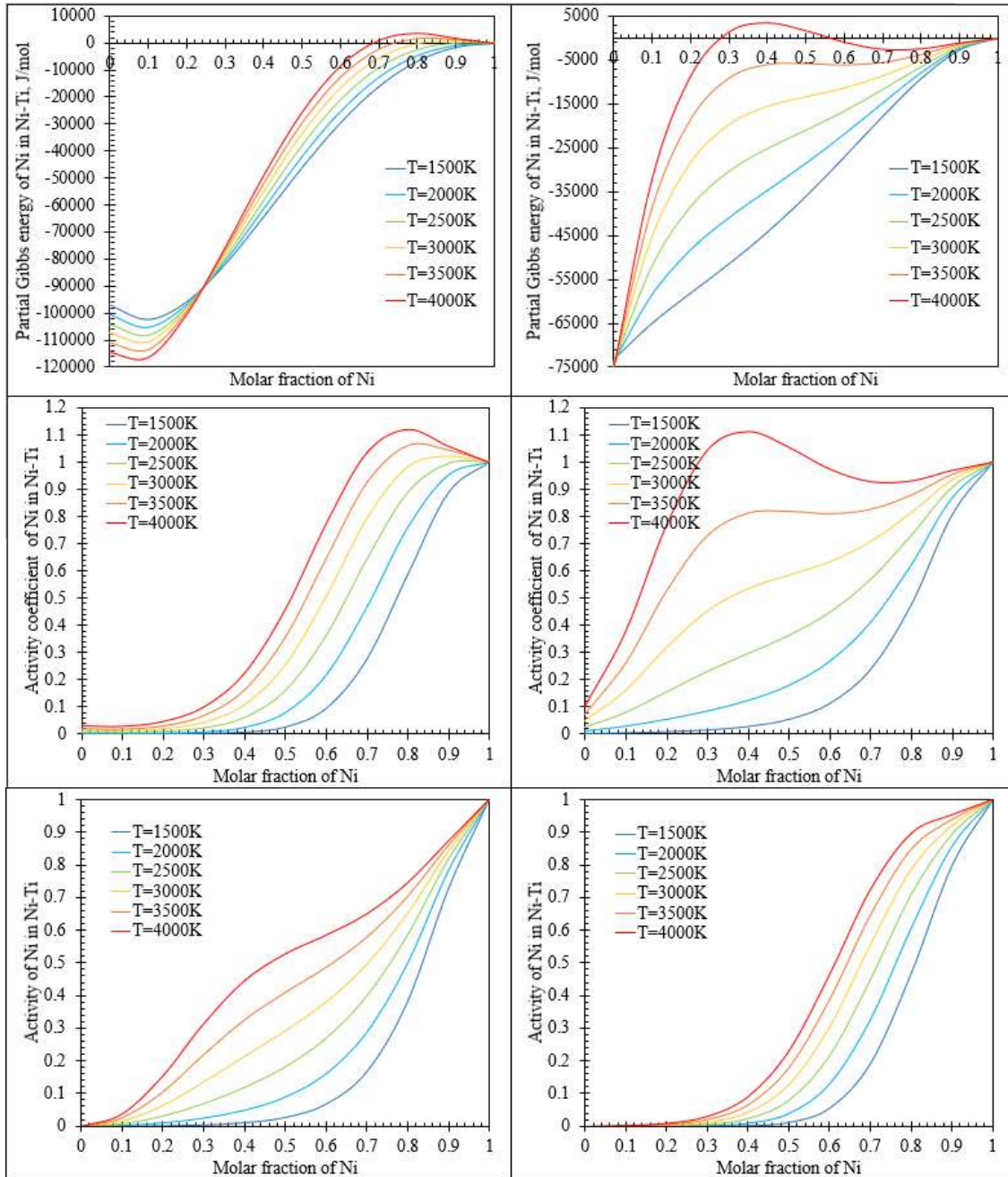
3. Thermophysical properties of NiTi alloy were investigated with emphasis on the requirements for mesoscale melt pool simulation during LPBF. Surface tension measurements for NiTi alloy were performed with pendant drop tensiometry. The value of 1530 ± 39 mN/m was obtained for NiTi melt at a temperature of 1603 K. The TiC layer acted as a barrier to carbon dissolution in the melt. Mesoscale simulation of the melt pool was carried out with surface tension obtained experimentally and from thermodynamic calculations. It was demonstrated that the melt pool morphology and temperature distribution were insignificantly affected when increased vorticity of a fluid flow and growth of velocity magnitudes were obtained for the experimental value of surface tension. It is noted that temperature coefficient of surface tension plays an important role in the CFD simulations, thus, future work will be dedicated to measurements of surface tension temperature dependence. Thermal diffusivity measurements were carried out with the flash method for manufactured NiTi samples via LPBF. Found temperature dependence is $\alpha(T) = 0.0095T + 0.9769$.

4. Simulation of the melt pool formation and consolidation of thin walls was carried out with high fidelity physical model based on an LBM hydrodynamic solver. In the simulations many significant aspects were taken into account such as Marangoni effect, recoil pressure, two component evaporation, powder recoating, and energy deposition by ray tracing of laser beam. The results of the simulations were validated by conducted experiment on the single tracks' analysis. It was shown that experimentally measured temperature of the martensite phase transformation has linear dependence from calculated Ni content in the thin wall and found dependence correlates with pioneer works dedicated to studies of Ni content influence on the martensitic phase transformation. This indicates that Ni evaporation is the main mechanism for tailoring NiTi functional properties via LPBF. However, multiple deviations are attributed to the effects of the resulting phase composition and microstructure. Both effects can be simulated simultaneously and considered for future work to precisely estimate the resulting functional properties of NiTi alloy after the LPBF procedure.

5. The feasibility of manufacturing endodontic Self-Adjusted Files from Nickel-Titanium shape memory alloy was demonstrated via high-resolution LPBF technology with found optimal process parameters including a laser power of 100 W, a scanning speed of 850 mm/s, and a layer thickness of 20 μm . Accuracy and resolution of final parts can be increased by introducing special algorithms to slicing software for implementation of scanning strategy based on single vectors without contours and subsequent hatching. In single track-based manufacturing, the inclined angle of the part plays an important role. It was demonstrated that the critical value for micro-objects is dependent on the layer thickness and linear energy density. Powder adhesion and the layering effect inherent to the LPBF technology have a higher impact on the manufacturing of the micro-object with high resolution. Such surface irregularities are inevitable; however, post-treatment can be applied to decrease the roughness of the part elements and the diameter of the struts.

Appendix A. Partial Gibbs free energy, activity coefficient, and activity

Calculated temperature dependences of partial Gibbs free energy, activity coefficient, and activity for the whole range of NiTi compositions are presented for two sets of mixing parameters. The left column corresponds to the parameters reported by Santhy [165] and the right column corresponds to the parameters obtained by Kajikawa [166].



Bibliography

- [1] D.C. Lagoudas, Shape Memory Alloys, Springer US, Boston, MA, 2008. <https://doi.org/10.1007/978-0-387-47685-8>.
- [2] G.B. Kauffman, I. Mayo, The Story of Nitinol: The Serendipitous Discovery of the Memory Metal and Its Applications, Chem. Educ. 2 (1997) 1–21. <https://doi.org/10.1007/s00897970111a>.
- [3] K.K. Alaneme, E.A. Okotete, Reconciling viability and cost-effective shape memory alloy options – A review of copper and iron based shape memory metallic systems, Eng. Sci. Technol. an Int. J. 19 (2016) 1582–1592. <https://doi.org/10.1016/j.jestch.2016.05.010>.
- [4] J.W. Mwangi, L.T. Nguyen, V.D. Bui, T. Berger, H. Zeidler, A. Schubert, Nitinol manufacturing and micromachining: A review of processes and their suitability in processing medical-grade nitinol, J. Manuf. Process. 38 (2019) 355–369. <https://doi.org/10.1016/j.jmapro.2019.01.003>.
- [5] T. Yoneyama, S. Miyazaki, Shape memory alloys for biomedical applications, Woodhead Publishing Limited, 2009. <https://doi.org/10.1533/9781845695248>.
- [6] R. Bogue, Shape-memory materials: A review of technology and applications, Assem. Autom. (2009). <https://doi.org/10.1108/01445150910972895>.
- [7] L. Yahia, ed., Shape Memory Implants, Springer Berlin Heidelberg, Berlin, Heidelberg, 2000. <https://doi.org/10.1007/978-3-642-59768-8>.
- [8] V.S. Guthikonda, R.S. Elliott, An effective interaction potential model for the shape memory alloy AuCd, Contin. Mech. Thermodyn. (2009). <https://doi.org/10.1007/s00161-009-0109-1>.
- [9] Y. Yang, A. Arabi-Hashemi, C. Leinenbach, M. Shahverdi, Influence of thermal treatment conditions on recovery stress formation in an FeMnSi-SMA, Mater. Sci. Eng. A. (2021). <https://doi.org/10.1016/j.msea.2020.140694>.
- [10] D.N. Fang, W. Lu, W.Y. Yan, T. Inoue, K.C. Hwang, Stress-strain relation of CuAlNi SMA single crystal under biaxial loading - Constitutive model and experiments, Acta Mater. (1998). [https://doi.org/10.1016/S1359-6454\(98\)00303-6](https://doi.org/10.1016/S1359-6454(98)00303-6).
- [11] C.M. Wayman, K. Shimizu, The shape memory ('marmem') effect in alloys, Met. Sci. J. (1972). <https://doi.org/10.1179/030634572790446028>.
- [12] C. Urbina, S. De Flor, F. Ferrando, New Understanding of the Influence of the Pre-Training Phase Transformation Behaviour on the TWSME in NiTi SMA Wires, (2013) 1415–1436. <https://doi.org/10.1007/s11340-013-9756-z>.
- [13] K. Otsuka, T. Kakeshita, Science and Technology of Shape-Memory Alloys: New Developments, MRS Bull. 27 (2002) 91–100. <https://doi.org/10.1557/mrs2002.43>.
- [14] Y. Liu, J. Van Humbeeck, R. Stalmans, L. Delaey, Some aspects of the properties of NiTi shape memory alloy, J. Alloys Compd. 247 (1997) 115–121. [https://doi.org/10.1016/S0925-8388\(96\)02572-8](https://doi.org/10.1016/S0925-8388(96)02572-8).
- [15] D. Hodgson, S. Russell, Nitinol melting, manufacture and fabrication, Minim. Invasive Ther. Allied Technol. 9 (2000) 61–65. <https://doi.org/10.3109/13645700009063051>.
- [16] S. Saedi, A.S. Turabi, M. Taheri Andani, C. Haberland, H. Karaca, M. Elahinia, M.T. Andani, C. Haberland, H. Karaca, M. Elahinia, The influence of heat treatment on the thermomechanical response of Ni-rich NiTi alloys manufactured by selective laser melting, J. Alloys Compd. 677 (2016) 204–210.

<https://doi.org/10.1016/j.jallcom.2016.03.161>.

- [17] S. Saedi, S.E. Saghaian, A. Jahadakbar, N. Shayesteh Moghaddam, M. Taheri Andani, S.M. Saghaian, Y.C. Lu, M. Elahinia, H.E. Karaca, Shape memory response of porous NiTi shape memory alloys fabricated by selective laser melting, *J. Mater. Sci. Mater. Med.* 29 (2018) 40. <https://doi.org/10.1007/s10856-018-6044-6>.
- [18] T. Tadaki, Y. Nakata, K. Shimizu, K. Otsuka, Crystal Structure, Composition and Morphology of a Precipitate in an Aged Ti-51 at%Ni Shape Memory Alloy, *Trans. Japan Inst. Met.* 27 (1986) 731–740. <https://doi.org/10.2320/matertrans1960.27.731>.
- [19] D.Y. Li, L.Q. Chen, Selective variant growth of coherent Ti₁₁Ni₁₄ precipitate in a TiNi alloy under applied stresses, *Acta Mater.* 45 (1997) 471–479. [https://doi.org/10.1016/S1359-6454\(96\)00207-8](https://doi.org/10.1016/S1359-6454(96)00207-8).
- [20] S. Miyazaki, K. Otsuka, Development of shape memory alloys., *ISIJ Int.* 29 (1989) 353–377. <https://doi.org/10.2355/isijinternational.29.353>.
- [21] C.A. Canbay, O. Karaduman, İ. Özkul, Lagging temperature problem in DTA/DSC measurement on investigation of NiTi SMA, *J. Mater. Sci. Mater. Electron.* (2020). <https://doi.org/10.1007/s10854-020-03881-y>.
- [22] J. Frenzel, E.P. George, A. Dlouhy, C. Somsen, M.F.-X. Wagner, G. Eggeler, Influence of Ni on martensitic phase transformations in NiTi shape memory alloys, *Acta Mater.* 58 (2010) 3444–3458. <https://doi.org/10.1016/j.actamat.2010.02.019>.
- [23] R. Piquard, A. D’Acunto, P. Laheurte, D. Dudzinski, Micro-end milling of NiTi biomedical alloys, burr formation and phase transformation, *Precis. Eng.* 38 (2014) 356–364. <https://doi.org/10.1016/j.precisioneng.2013.11.006>.
- [24] E. Kaya, İ. Kaya, A review on machining of NiTi shape memory alloys: the process and post process perspective, *Int. J. Adv. Manuf. Technol.* 100 (2019) 2045–2087. <https://doi.org/10.1007/s00170-018-2818-8>.
- [25] M.H. Elahinia, M. Hashemi, M. Tabesh, S.B. Bhaduri, Manufacturing and processing of NiTi implants: A review, *Prog. Mater. Sci.* 57 (2012) 911–946. <https://doi.org/10.1016/j.pmatsci.2011.11.001>.
- [26] P. Saha, S. Datta, M.S. Raza, D.K. Pratihari, Effects of Heat Input on Weld-Bead Geometry, Surface Chemical Composition, Corrosion Behavior and Thermal Properties of Fiber Laser-Welded Nitinol Shape Memory Alloy, *J. Mater. Eng. Perform.* (2019). <https://doi.org/10.1007/s11665-019-04077-0>.
- [27] D. Biermann, F. Kahleyss, E. Krebs, T. Upmeyer, A Study on Micro-Machining Technology for the Machining of NiTi: Five-Axis Micro-Milling and Micro Deep-Hole Drilling, *J. Mater. Eng. Perform.* 20 (2011) 745–751. <https://doi.org/10.1007/s11665-010-9796-9>.
- [28] M. Bram, A. Ahmad-Khanlou, A. Heckmann, B. Fuchs, H.P. Buchkremer, D. Stöver, Powder metallurgical fabrication processes for NiTi shape memory alloy parts, *Mater. Sci. Eng. A.* 337 (2002) 254–263. [https://doi.org/10.1016/S0921-5093\(02\)00028-X](https://doi.org/10.1016/S0921-5093(02)00028-X).
- [29] K. Alvarez, H. Nakajima, Metallic scaffolds for bone regeneration, *Materials (Basel)*. 2 (2009) 790–832. <https://doi.org/10.3390/ma2030790>.
- [30] I. Gibson, D. Rosen, B. Stucker, *Additive Manufacturing Technologies: 3D Printing, Rapid Prototyping, and Direct Digital Manufacturing*, 2015.
- [31] O.A. Mohamed, S.H. Masood, J.L. Bhowmik, Optimization of fused deposition modeling process parameters: a review of current research and future prospects, *Adv. Manuf.* 3 (2015) 42–53. <https://doi.org/10.1007/s40436-014-0097-7>.

- [32] J. Zhang, Q. Hu, S. Wang, J. Tao, M. Gou, Digital Light Processing Based Three-dimensional Printing for Medical Applications, *Int. J. Bioprinting*. 6 (2019) 1. <https://doi.org/10.18063/ijb.v6i1.242>.
- [33] X. Fu, B. Zou, H. Xing, L. Li, Y. Li, X. Wang, Effect of printing strategies on forming accuracy and mechanical properties of ZrO₂ parts fabricated by SLA technology, *Ceram. Int.* 45 (2019) 17630–17637. <https://doi.org/10.1016/j.ceramint.2019.05.328>.
- [34] P. Wen, Y. Qin, Y. Chen, M. Voshage, L. Jauer, R. Poprawe, J.H. Schleifenbaum, Laser additive manufacturing of Zn porous scaffolds: Shielding gas flow, surface quality and densification, *J. Mater. Sci. Technol.* 35 (2019) 368–376. <https://doi.org/10.1016/j.jmst.2018.09.065>.
- [35] M. Elahinia, N. Shayesteh Moghaddam, M. Taheri Andani, A. Amerinatanzi, B.A. Bimber, R.F. Hamilton, Fabrication of NiTi through additive manufacturing: A review, *Prog. Mater. Sci.* 83 (2016) 630–663. <https://doi.org/10.1016/j.pmatsci.2016.08.001>.
- [36] T.C. Dzogbewu, W.B. du Preez, Additive manufacturing of ti-based intermetallic alloys: A review and conceptualization of a next-generation machine, *Materials (Basel)*. 14 (2021). <https://doi.org/10.3390/ma14154317>.
- [37] L. Caprio, A.G. Demir, G. Chiari, B. Previtali, Defect-free laser powder bed fusion of Ti–48Al–2Cr–2Nb with a high temperature inductive preheating system, *JPhys Photonics*. 2 (2020) 0–12. <https://doi.org/10.1088/2515-7647/ab7080>.
- [38] I. Shishkovsky, V. Sherbakof, Influence of laser cycling on electro-structural features of nickel-titanium SMA fabricated by LPBF process, *Appl. Surf. Sci.* 508 (2020) 145278. <https://doi.org/10.1016/j.apsusc.2020.145278>.
- [39] A.S. Shinkaryov, D.Y. Ozherelkov, I.A. Pelevin, S.A. Eremin, V.N. Anikin, M.A. Burmistrov, S. V. Chernyshikhin, A.A. Gromov, A.Y. Nalivaiko, Laser fusion of aluminum powder coated with diamond particles via selective laser melting: Powder preparation and synthesis description, *Coatings*. 11 (2021). <https://doi.org/10.3390/coatings11101219>.
- [40] A.Y. Nalivaiko, D.Y. Ozherelkov, I.A. Pelevin, S. V. Chernyshikhin, A.E. Medvedev, A. V. Korshunov, A.N. Arnautov, A.A. Gromov, Comprehensive Study of the 3D Printing of Single Tracks and Cubic Samples by Selective Laser Melting of AlSi10MgCu Alloy, *Met. Mater. Int.* 28 (2022) 787–801. <https://doi.org/10.1007/s12540-021-01115-2>.
- [41] I.A. Pelevin, M.A. Burmistrov, D.Y. Ozherelkov, A.S. Shinkaryov, S. V. Chernyshikhin, A.A. Gromov, A.Y. Nalivaiko, Laser powder bed fusion of chromium bronze using recycled powder, *Materials (Basel)*. 14 (2021) 3644. <https://doi.org/10.3390/ma14133644>.
- [42] J.B. Forien, N.P. Calta, P.J. DePond, G.M. Guss, T.T. Roehling, M.J. Matthews, Detecting keyhole pore defects and monitoring process signatures during laser powder bed fusion: A correlation between in situ pyrometry and ex situ X-ray radiography, *Addit. Manuf.* 35 (2020) 101336. <https://doi.org/10.1016/j.addma.2020.101336>.
- [43] J.N. Zhu, E. Borisov, X. Liang, E. Farber, M.J.M.M. Hermans, A. Popovich, V.A. Popovich, Predictive analytical modelling and experimental validation of processing maps in additive manufacturing of nitinol alloys, *Addit. Manuf.* 38 (2021) 101802. <https://doi.org/10.1016/j.addma.2020.101802>.
- [44] I. Shishkovsky, I. Yadroitsev, I. Smurov, Direct Selective Laser Melting of Nitinol Powder, *Phys. Procedia*. 39 (2012) 447–454. <https://doi.org/10.1016/j.phpro.2012.10.060>.
- [45] S. V. Chernyshikhin, D.G. Firsov, I. V. Shishkovsky, Selective Laser Melting of

- Pre-Alloyed NiTi Powder: Single-Track Study and FE Modeling with Heat Source Calibration, *Materials* (Basel). 14 (2021) 7486. <https://doi.org/10.3390/ma14237486>.
- [46] T. Qi, H. Zhu, H. Zhang, J. Yin, L. Ke, X. Zeng, Selective laser melting of Al7050 powder: Melting mode transition and comparison of the characteristics between the keyhole and conduction mode, *Mater. Des.* 135 (2017) 257–266. <https://doi.org/10.1016/j.matdes.2017.09.014>.
- [47] C. Haberland, M. Elahinia, J.M. Walker, H. Meier, J. Frenzel, On the development of high quality NiTi shape memory and pseudoelastic parts by additive manufacturing, *Smart Mater. Struct.* 23 (2014). <https://doi.org/10.1088/0964-1726/23/10/104002>.
- [48] S. Dadbakhsh, M. Speirs, J.P. Kruth, J. Van Humbeeck, Influence of SLM on shape memory and compression behaviour of NiTi scaffolds, *CIRP Ann. - Manuf. Technol.* 64 (2015) 209–212. <https://doi.org/10.1016/j.cirp.2015.04.039>.
- [49] T. Bormann, B. Müller, M. Schinhammer, A. Kessler, P. Thalmann, M. de Wild, Microstructure of selective laser melted nickel–titanium, *Mater. Charact.* 94 (2014) 189–202. <https://doi.org/10.1016/j.matchar.2014.05.017>.
- [50] W. Hoffmann, T. Bormann, A. Rossi, B. Müller, R. Schumacher, I. Martin, M. de Wild, D. Wendt, Rapid prototyped porous nickel–titanium scaffolds as bone substitutes, *J. Tissue Eng.* (2014). <https://doi.org/10.1177/2041731414540674>.
- [51] B. Zhang, J. Chen, C. Coddet, Microstructure and transformation behavior of in-situ shape memory alloys by selective laser melting Ti-Ni mixed powder, *J. Mater. Sci. Technol.* (2013). <https://doi.org/10.1016/j.jmst.2013.05.006>.
- [52] Z. Xiong, Z. Li, Z. Sun, S. Hao, Y. Yang, M. Li, C. Song, P. Qiu, L. Cui, Selective laser melting of NiTi alloy with superior tensile property and shape memory effect, *J. Mater. Sci. Technol.* 35 (2019) 2238–2242. <https://doi.org/10.1016/j.jmst.2019.05.015>.
- [53] C. Kusuma, S.H. Ahmed, A. Mian, R. Srinivasan, Effect of Laser Power and Scan Speed on Melt Pool Characteristics of Commercially Pure Titanium (CP-Ti), *J. Mater. Eng. Perform.* 26 (2017) 3560–3568. <https://doi.org/10.1007/s11665-017-2768-6>.
- [54] I. Yadroitsev, A. Gusarov, I. Yadroitsava, I. Smurov, Single track formation in selective laser melting of metal powders, *J. Mater. Process. Technol.* 210 (2010) 1624–1631. <https://doi.org/10.1016/j.jmatprotec.2010.05.010>.
- [55] W.E. King, H.D. Barth, V.M. Castillo, G.F. Gallegos, J.W. Gibbs, D.E. Hahn, C. Kamath, A.M. Rubenchik, Observation of keyhole-mode laser melting in laser powder-bed fusion additive manufacturing, *J. Mater. Process. Technol.* 214 (2014) 2915–2925. <https://doi.org/10.1016/j.jmatprotec.2014.06.005>.
- [56] J.J.S.S. Dilip, S. Zhang, C. Teng, K. Zeng, C. Robinson, D. Pal, B. Stucker, Influence of processing parameters on the evolution of melt pool, porosity, and microstructures in Ti-6Al-4V alloy parts fabricated by selective laser melting, *Prog. Addit. Manuf.* 2 (2017) 157–167. <https://doi.org/10.1007/s40964-017-0030-2>.
- [57] Y. Liu, C. Liu, W. Liu, Y. Ma, S. Tang, C. Liang, Q. Cai, C. Zhang, Optimization of parameters in laser powder deposition AlSi10Mg alloy using Taguchi method, *Opt. Laser Technol.* 111 (2019) 470–480. <https://doi.org/10.1016/j.optlastec.2018.10.030>.
- [58] Z. Yu, Z. Xu, Y. Guo, R. Xin, R. Liu, C. Jiang, L. Li, Z. Zhang, L. Ren, Study on properties of SLM-NiTi shape memory alloy under the same energy density, *J. Mater. Res. Technol.* 13 (2021) 241–250. <https://doi.org/10.1016/j.jmrt.2021.04.058>.
- [59] Z.X. Khoo, J.E.M. Teoh, Y. Liu, C.K. Chua, S. Yang, J. An, K.F. Leong, W.Y. Yeong, 3D printing of smart materials: A review on recent progresses in 4D printing, *Virtual Phys. Prototyp.* (2015). <https://doi.org/10.1080/17452759.2015.1097054>.

- [60] I. V. Shishkovsky, V.I. Scherbakov, M. V. Kuznetsov, O. V. Belousova, Y.G. Morozov, 4D Laser Printing of Functionally Graded Structures and Items from Mixtures of Powdered Polymers with Functional Micro- and Nanoparticles: An Autoreview, *Int. J. Self-Propagating High-Temperature Synth.* 29 (2020) 77–86. <https://doi.org/10.3103/S1061386220020132>.
- [61] G. Shi, L. Li, Z. Yu, R. Liu, P. Sha, Z. Xu, Y. Guo, R. Xi, J. Liu, R. Xin, L. Chen, X. Wang, Z. Zhang, The interaction effect of process parameters on the phase transformation behavior and tensile properties in additive manufacturing of Ni-rich NiTi alloy, *J. Manuf. Process.* (2022). <https://doi.org/10.1016/j.jmapro.2022.03.027>.
- [62] B. Feng, C. Wang, Q. Zhang, Y. Ren, L. Cui, Q. Yang, S. Hao, Effect of laser hatch spacing on the pore defects, phase transformation and properties of selective laser melting fabricated NiTi shape memory alloys, *Mater. Sci. Eng. A.* (2022). <https://doi.org/10.1016/j.msea.2022.142965>.
- [63] Z. Yu, Z. Xu, Y. Guo, P. Sha, R. Liu, R. Xin, L. Li, L. Chen, X. Wang, Z. Zhang, L. Ren, Analysis of microstructure, mechanical properties, wear characteristics and corrosion behavior of SLM-NiTi under different process parameters, *J. Manuf. Process.* (2022). <https://doi.org/10.1016/j.jmapro.2022.01.010>.
- [64] Y. Guo, Z. Xu, Q. Wang, S. Zu, M. Liu, Z. Yu, Z. Zhang, L. Ren, Corrosion resistance and biocompatibility of graphene oxide coating on the surface of the additively manufactured NiTi alloy, *Prog. Org. Coatings.* (2022). <https://doi.org/10.1016/j.porgcoat.2022.106722>.
- [65] Y. Luo, H. Lu, H. Ma, W. Cai, A. Yan, C. Yang, Microstructure and mechanical properties of Ni_{50.7}Ti_{49.3} shape memory alloy fabricated by selective laser melting, in: *J. Phys. Conf. Ser.*, 2021. <https://doi.org/10.1088/1742-6596/2044/1/012078>.
- [66] X. Wang, J. Yu, J. Liu, L. Chen, Q. Yang, H. Wei, J. Sun, Z. Wang, Z. Zhang, G. Zhao, J. Van Humbeeck, Effect of process parameters on the phase transformation behavior and tensile properties of NiTi shape memory alloys fabricated by selective laser melting, *Addit. Manuf.* 36 (2020) 101545. <https://doi.org/10.1016/j.addma.2020.101545>.
- [67] Y. Yang, J.B. Zhan, J.B. Sui, C.Q. Li, K. Yang, P. Castany, T. Gloriant, Functionally graded NiTi alloy with exceptional strain-hardening effect fabricated by SLM method, *Scr. Mater.* (2020). <https://doi.org/10.1016/j.scriptamat.2020.07.019>.
- [68] C. Zhao, H. Liang, S. Luo, J. Yang, Z. Wang, The effect of energy input on reaction, phase transition and shape memory effect of NiTi alloy by selective laser melting, *J. Alloys Compd.* (2020). <https://doi.org/10.1016/j.jallcom.2019.153288>.
- [69] S. Saedi, A.S. Turabi, M.T. Andani, N.S. Moghaddam, M. Elahinia, H.E. Karaca, Texture, aging, and superelasticity of selective laser melting fabricated Ni-rich NiTi alloys, *Mater. Sci. Eng. A.* (2017). <https://doi.org/10.1016/j.msea.2017.01.008>.
- [70] N. Shayesteh Moghaddam, S. Saedi, A. Amerinatanzi, A. Jahadakbar, E. Saghaian, H. Karaca, M. Elahinia, Influence of SLM on compressive response of NiTi scaffolds, in: 2018. <https://doi.org/10.1117/12.2305251>.
- [71] R.F. Hamilton, B.A. Bimber, M. Taheri Andani, M. Elahinia, Multi-scale shape memory effect recovery in NiTi alloys additive manufactured by selective laser melting and laser directed energy deposition, *J. Mater. Process. Technol.* 250 (2017) 55–64. <https://doi.org/10.1016/j.jmatprotec.2017.06.027>.
- [72] J. Ma, B. Franco, G. Tapia, K. Karayagiz, L. Johnson, J. Liu, R. Arroyave, I. Karaman, A. Elwany, Spatial Control of Functional Response in 4D-Printed Active Metallic Structures, *Sci. Rep.* 7 (2017) 46707. <https://doi.org/10.1038/srep46707>.

- [73] M. Speirs, X. Wang, S. Van Baelen, A. Ahadi, S. Dadbakhsh, J.P. Kruth, J. Van Humbeeck, On the Transformation Behavior of NiTi Shape-Memory Alloy Produced by SLM, *Shape Mem. Superelasticity*. (2016). <https://doi.org/10.1007/s40830-016-0083-y>.
- [74] T. Bormann, R. Schumacher, B. Müller, M. Mertmann, M. de Wild, Tailoring Selective Laser Melting Process Parameters for NiTi Implants, *J. Mater. Eng. Perform.* 21 (2012) 2519–2524. <https://doi.org/10.1007/s11665-012-0318-9>.
- [75] S. Hatami, T. Ma, T. Vuoristo, J. Bertilsson, O. Lyckfeldt, Fatigue Strength of 316 L Stainless Steel Manufactured by Selective Laser Melting, *J. Mater. Eng. Perform.* 29 (2020) 3183–3194. <https://doi.org/10.1007/s11665-020-04859-x>.
- [76] N. Mohammadian, S. Turenne, V. Brailovski, Surface finish control of additively-manufactured Inconel 625 components using combined chemical-abrasive flow polishing, *J. Mater. Process. Technol.* 252 (2018) 728–738. <https://doi.org/10.1016/j.jmatprotec.2017.10.020>.
- [77] D.A. Lesyk, S. Martinez, B.N. Mordiyuk, V. V. Dzhemelinskyi, Lamikiz, G.I. Prokopenko, Post-processing of the Inconel 718 alloy parts fabricated by selective laser melting: Effects of mechanical surface treatments on surface topography, porosity, hardness and residual stress, *Surf. Coatings Technol.* (2020). <https://doi.org/10.1016/j.surfcoat.2019.125136>.
- [78] J.J.S. Dilip, S. Zhang, C. Teng, K. Zeng, C. Robinson, D. Pal, B. Stucker, Influence of processing parameters on the evolution of melt pool, porosity, and microstructures in Ti-6Al-4V alloy parts fabricated by selective laser melting, *Prog. Addit. Manuf.* 2 (2017) 157–167. <https://doi.org/10.1007/s40964-017-0030-2>.
- [79] P. Gao, Z. Wang, X. Zeng, Effect of process parameters on morphology, sectional characteristics and crack sensitivity of Ti-40Al-9V-0.5Y alloy single tracks produced by selective laser melting, *Int. J. Light. Mater. Manuf.* 2 (2019) 355–361. <https://doi.org/10.1016/j.ijlmm.2019.04.001>.
- [80] S. Li, H. Hassanin, M.M. Attallah, N.J.E. Adkins, K. Essa, The development of TiNi-based negative Poisson's ratio structure using selective laser melting, *Acta Mater.* 105 (2016) 75–83. <https://doi.org/10.1016/j.actamat.2015.12.017>.
- [81] L. Parry, I. Ashcroft, D. Bracket, R.D. Wildman, Investigation of Residual Stresses in Selective Laser Melting, *Key Eng. Mater.* 627 (2014) 129–132. <https://doi.org/10.4028/www.scientific.net/KEM.627.129>.
- [82] J. Hajnys, M. Pagáč, J. Měsíček, J. Petru, M. Król, Influence of Scanning Strategy Parameters on Residual Stress in the SLM Process According to the Bridge Curvature Method for AISI 316L Stainless Steel, *Materials (Basel)*. 13 (2020) 1659. <https://doi.org/10.3390/ma13071659>.
- [83] N. Shayesteh Moghaddam, S. Saedi, A. Amerinatanzi, A. Hinojos, A. Ramazani, J. Kundin, M.J. Mills, H. Karaca, M. Elahinia, Achieving superelasticity in additively manufactured NiTi in compression without post-process heat treatment, *Sci. Rep.* 9 (2019) 41. <https://doi.org/10.1038/s41598-018-36641-4>.
- [84] D. Wang, Y. Yang, R. Liu, D. Xiao, J. Sun, Study on the designing rules and processability of porous structure based on selective laser melting (SLM), *J. Mater. Process. Technol.* 213 (2013) 1734–1742. <https://doi.org/10.1016/j.jmatprotec.2013.05.001>.
- [85] D. Wang, Y. Yang, Z. Yi, X. Su, Research on the fabricating quality optimization of the overhanging surface in SLM process, *Int. J. Adv. Manuf. Technol.* 65 (2013) 1471–1484. <https://doi.org/10.1007/s00170-012-4271-4>.

- [86] I. Yadroitsev, P. Bertrand, I. Smurov, Parametric analysis of the selective laser melting process, *Appl. Surf. Sci.* 253 (2007) 8064–8069. <https://doi.org/10.1016/j.apsusc.2007.02.088>.
- [87] S. Qu, J. Ding, X. Song, Achieving Triply Periodic Minimal Surface Thin-Walled Structures by Micro Laser Powder Bed Fusion Process, *Micromachines*. 12 (2021) 705. <https://doi.org/10.3390/mi12060705>.
- [88] L. Caprio, A.G. Demir, B. Previtali, Comparative study between CW and PW emissions in selective laser melting, *J. Laser Appl.* 30 (2018) 032305. <https://doi.org/10.2351/1.5040631>.
- [89] Z. Wu, S.P. Narra, A. Rollett, Exploring the fabrication limits of thin-wall structures in a laser powder bed fusion process, *Int. J. Adv. Manuf. Technol.* (2020). <https://doi.org/10.1007/s00170-020-05827-4>.
- [90] D. Lesyk, O. Lymar, V. Dzhemelinkyi, Surface Characterization of the Cobalt-Based Alloy Stents Fabricated by 3D Laser Metal Fusion Technology, *Lect. Notes Networks Syst.* 233 (2021) 357–364. https://doi.org/10.1007/978-3-030-75275-0_40/FIGURES/4.
- [91] A. Orla, M. Mcgee, S. Geraghty, C. Hughes, P. Jamshidi, D.P. Kenny, M.M. Attallah, C. Lally, An Investigation into Patient-Specific 3D Printed Titanium Stents and the use of Etching to Overcome Selective Laser Melting Design Constraints, *BioRxiv*. (2021) 2021.03.07.434132. <https://doi.org/10.1101/2021.03.07.434132>.
- [92] B. Paul, A. Lode, A.M. Placht, A. Voß, S. Pilz, U. Wolff, S. Oswald, A. Gebert, M. Gelinsky, J. Hufenbach, Cell-Material Interactions in Direct Contact Culture of Endothelial Cells on Biodegradable Iron-Based Stents Fabricated by Laser Powder Bed Fusion and Impact of Ion Release, *ACS Appl. Mater. Interfaces*. 14 (2022) 439–451. https://doi.org/10.1021/ACSAMI.1C21901/SUPPL_FILE/AM1C21901_SI_001.PDF.
- [93] S. Maffia, V. Finazzi, F. Berti, F. Migliavacca, L. Petrini, B. Previtali, A.G. Demir, Selective laser melting of NiTi stents with open-cell and variable diameter, *Smart Mater. Struct.* 30 (2021) 105010. <https://doi.org/10.1088/1361-665X/ac1908>.
- [94] C. Momma, U. Knop, S. Nolte, Laser Cutting of Slotted Tube Coronary Stents – State-of-the-Art and Future Developments, (1999) 39–44.
- [95] Y.Y. Kaplanskii, E.A. Levashov, A. V. Korotitskiy, P.A. Loginov, Z.A. Sentyurina, A.B. Mazalov, Influence of aging and HIP treatment on the structure and properties of NiAl-based turbine blades manufactured by laser powder bed fusion, *Addit. Manuf.* 31 (2020) 100999. <https://doi.org/10.1016/j.addma.2019.100999>.
- [96] K. Gruber, I. Smolina, M. Kasprowicz, T. Kurzynowski, Evaluation of inconel 718 metallic powder to optimize the reuse of powder and to improve the performance and sustainability of the laser powder bed fusion (Lpbf) process, *Materials (Basel)*. (2021). <https://doi.org/10.3390/ma14061538>.
- [97] M. Leary, M. Mazur, J. Elambasseril, M. McMillan, T. Chirent, Y. Sun, M. Qian, M. Easton, M. Brandt, Selective laser melting (SLM) of AlSi12Mg lattice structures, *Mater. Des.* 98 (2016) 344–357. <https://doi.org/10.1016/j.matdes.2016.02.127>.
- [98] Z. Xiao, Y. Yang, R. Xiao, Y. Bai, C. Song, D. Wang, Evaluation of topology-optimized lattice structures manufactured via selective laser melting, *Mater. Des.* 143 (2018) 27–37. <https://doi.org/10.1016/j.matdes.2018.01.023>.
- [99] N. Sabahi, W. Chen, C.H. Wang, J.J. Kruzic, X. Li, A Review on Additive Manufacturing of Shape-Memory Materials for Biomedical Applications, *Jom.* 72 (2020) 1229–1253. <https://doi.org/10.1007/s11837-020-04013-x>.

- [100] J. Fu, S. Qu, J. Ding, X. Song, M.W. Fu, Comparison of the microstructure, mechanical properties and distortion of stainless steel 316 L fabricated by micro and conventional laser powder bed fusion, *Addit. Manuf.* (2021). <https://doi.org/10.1016/j.addma.2021.102067>.
- [101] L. Cao, Workpiece-scale numerical simulations of SLM molten pool dynamic behavior of 316L stainless steel, *Comput. Math. with Appl.* (2020). <https://doi.org/10.1016/j.camwa.2020.04.020>.
- [102] A. V. Gusarov, I. Yadroitsev, P. Bertrand, I. Smurov, Model of Radiation and Heat Transfer in Laser-Powder Interaction Zone at Selective Laser Melting, *J. Heat Transfer*. 131 (2009). <https://doi.org/10.1115/1.3109245>.
- [103] L.E. Loh, C.K. Chua, W.Y. Yeong, J. Song, M. Mapar, S.L. Sing, Z.H. Liu, D.Q. Zhang, Numerical investigation and an effective modelling on the Selective Laser Melting (SLM) process with aluminium alloy 6061, *Int. J. Heat Mass Transf.* 80 (2015) 288–300. <https://doi.org/10.1016/j.ijheatmasstransfer.2014.09.014>.
- [104] S. Gao, Y. Feng, J. Wang, M. Qin, O.P. Bodunde, W.-H. Liao, P. Guo, Molten pool characteristics of a nickel-titanium shape memory alloy for directed energy deposition, *Opt. Laser Technol.* 142 (2021) 107215. <https://doi.org/10.1016/j.optlastec.2021.107215>.
- [105] S. Singh, N. Resnina, S. Belyaev, A.N. Jinoop, A. Shukla, I.A. Palani, C.P. Paul, K.S. Bindra, Investigations on NiTi shape memory alloy thin wall structures through laser marking assisted wire arc based additive manufacturing, *J. Manuf. Process.* 66 (2021) 70–80. <https://doi.org/10.1016/j.jmapro.2021.04.004>.
- [106] M. Mehrpouya, A. Gisario, H. Huang, A. Rahimzadeh, M. Elahinia, Numerical study for prediction of optimum operational parameters in laser welding of NiTi alloy, *Opt. Laser Technol.* (2019). <https://doi.org/10.1016/j.optlastec.2019.05.010>.
- [107] M.F. Ashby, *Materials Selection in Mechanical Design Third Edition*, 2005.
- [108] O. Parate, N. Gupta, Material selection for electrostatic microactuators using Ashby approach, *Mater. Des.* 32 (2011) 1577–1581. <https://doi.org/10.1016/j.matdes.2010.09.012>.
- [109] J. Ma, I. Karaman, R.D. Noebe, High temperature shape memory alloys, *Int. Mater. Rev.* 55 (2010) 257–315. <https://doi.org/10.1179/095066010X12646898728363>.
- [110] J. Mohd Jani, M. Leary, A. Subic, M.A. Gibson, A review of shape memory alloy research, applications and opportunities, *Mater. Des.* 56 (2014) 1078–1113. <https://doi.org/10.1016/j.matdes.2013.11.084>.
- [111] I. V. Shishkovsky, L.T. Volova, M. V. Kuznetsov, Y.G. Morozov, I.P. Parkin, Porous biocompatible implants and tissue scaffolds synthesized by selective laser sintering from Ti and NiTi, *J. Mater. Chem.* 18 (2008) 1309. <https://doi.org/10.1039/b715313a>.
- [112] I. Shishkovsky, Y. Morozov, I. Smurov, Nanofractal surface structure under laser sintering of titanium and nitinol for bone tissue engineering, *Appl. Surf. Sci.* 254 (2007) 1145–1149. <https://doi.org/10.1016/j.apsusc.2007.09.021>.
- [113] S. V. Chernyshikhin, I.A. Pelevin, F. Karimi, I. V. Shishkovsky, The Study on Resolution Factors of LPBF Technology for Manufacturing Superelastic NiTi Endodontic Files, *Materials (Basel)*. 15 (2022) 6556. <https://doi.org/10.3390/ma15196556>.
- [114] A. Bansiddhi, T.D. Sargeant, S.I. Stupp, D.C. Dunand, Porous NiTi for bone implants: A review, *Acta Biomater.* 4 (2008) 773–782. <https://doi.org/10.1016/j.actbio.2008.02.009>.
- [115] M. Jalali, K. Mohammadi, M.R. Movahhedy, F. Karimi, S.K. Sadrnezhad, S. V. Chernyshikhin, I. V. Shishkovsky, SLM Additive Manufacturing of NiTi Porous Implants:

A Review of Constitutive Models, Finite Element Simulations, Manufacturing, Heat Treatment, Mechanical, and Biomedical Studies, The Korean Institute of Metals and Materials, 2023. <https://doi.org/10.1007/s12540-023-01401-1>.

[116] K. Kanjwal, R. Yeasting, J.D. Maloney, C. Baptista, H. Elsamaloty, M. Sheikh, M. Elahinia, W. Anderson, J.D. Maloney, Retro-cardiac esophageal mobility and deflection to prevent thermal injury during atrial fibrillation ablation: an anatomic feasibility study, *J. Interv. Card. Electrophysiol.* 30 (2011) 45–53. <https://doi.org/10.1007/s10840-010-9524-2>.

[117] E. Tarkesh Esfahani, M.H. Elahinia, Developing an Adaptive Controller for a Shape Memory Alloy Walking Assistive Device, *J. Vib. Control.* 16 (2010) 1897–1914. <https://doi.org/10.1177/1077546309344163>.

[118] J. Fu, Z. Hu, X. Song, W. Zhai, Y. Long, H. Li, M. Fu, Micro selective laser melting of NiTi shape memory alloy: Defects, microstructures and thermal/mechanical properties, *Opt. Laser Technol.* 131 (2020) 106374. <https://doi.org/10.1016/j.optlastec.2020.106374>.

[119] S.N. Zhevnenko, M. V. Gorshenkov, I.S. Petrov, Effect of B on improving wetting and imbibition of sintered porous Ta by Cu melt, *J. Alloys Compd.* 860 (2021) 157886. <https://doi.org/10.1016/j.jallcom.2020.157886>.

[120] A. Zakirov, S. Belousov, M. Bogdanova, B. Korneev, A. Stepanov, A. Perepelkina, V. Levchenko, A. Meshkov, B. Potapkin, Predictive modeling of laser and electron beam powder bed fusion additive manufacturing of metals at the mesoscale, *Addit. Manuf.* 35 (2020) 101236. <https://doi.org/10.1016/J.ADDMA.2020.101236>.

[121] M.C. Sukop, D.T. Thorne, *Lattice Boltzmann Modeling*, Springer Berlin Heidelberg, Berlin, Heidelberg, 2006. <https://doi.org/10.1007/978-3-540-27982-2>.

[122] J. Brillo, T. Schumacher, K. Kajikawa, Density of Liquid Ni-Ti and a New Optical Method for its Determination, *Metall. Mater. Trans. A Phys. Metall. Mater. Sci.* (2019). <https://doi.org/10.1007/s11661-018-5047-8>.

[123] C.J. Knight, Theoretical Modeling of Rapid Surface Vaporization with Back Pressure, *AIAA J.* 17 (1979) 519–523. <https://doi.org/10.2514/3.61164>.

[124] A. Klassen, Simulation of Evaporation Phenomena in Selective Laser Melting, 2018. <https://doi.org/10.25593/978-3-96147-091-4>.

[125] C.B. Alcock, V.P. Itkin, M.K. Horrigan, Vapour Pressure Equations for the Metallic Elements: 298–2500K, *Can. Metall. Q.* 23 (1984) 309–313. <https://doi.org/10.1179/cmq.1984.23.3.309>.

[126] A.T. Sutton, C.S. Kriewall, M.C. Leu, J.W. Newkirk, A.T. Sutton, C.S. Kriewall, M.C. Leu, J.W. Newkirk, Powder characterisation techniques and effects of powder characteristics on part properties in powder-bed fusion processes, 2759 (2016). <https://doi.org/10.1080/17452759.2016.1250605>.

[127] K. Kassym, A. Perveen, Atomization processes of metal powders for 3D printing, in: *Mater. Today Proc.*, 2019. <https://doi.org/10.1016/j.matpr.2020.02.364>.

[128] G.S. Altug-Peduk, S. Dilibal, O. Harrysson, S. Ozbek, H. West, Characterization of Ni–Ti Alloy Powders for Use in Additive Manufacturing, *Russ. J. Non-Ferrous Met.* 59 (2018) 433–439. <https://doi.org/10.3103/S106782121804003X>.

[129] A.S. Shinkaryov, M. V. Cherkasova, I.A. Pelevin, D.Y. Ozherelkov, S. V. Chernyshikhin, N.A. Kharitonova, A.A. Gromov, A.Y. Nalivaiko, Aluminum powder preparation for additive manufacturing using electrostatic classification, *Coatings.* 11 (2021). <https://doi.org/10.3390/coatings11060629>.

[130] S.E. Brika, M. Letenneur, C.A. Dion, V. Brailovski, Influence of particle

- morphology and size distribution on the powder flowability and laser powder bed fusion manufacturability of Ti-6Al-4V alloy, *Addit. Manuf.* 31 (2020) 100929. <https://doi.org/10.1016/j.addma.2019.100929>.
- [131] S. Vock, B. Klöden, A. Kirchner, T. Weißgärber, B. Kieback, Powders for powder bed fusion: a review, *Prog. Addit. Manuf.* 4 (2019) 383–397. <https://doi.org/10.1007/s40964-019-00078-6>.
- [132] M. Bonesso, P. Rebesan, C. Gennari, S. Mancin, R. Dima, A. Pepato, I. Calliari, Effect of Particle Size Distribution on Laser Powder Bed Fusion Manufacturability of Copper, 166 (2021) 256–262. <https://doi.org/10.1007/s00501-021-01107-0>.
- [133] L. Xue, K.C. Atli, S. Picak, C. Zhang, B. Zhang, A. Elwany, R. Arroyave, I. Karaman, Controlling martensitic transformation characteristics in defect-free NiTi shape memory alloys fabricated using laser powder bed fusion and a process optimization framework, *Acta Mater.* 215 (2021) 117017. <https://doi.org/10.1016/j.actamat.2021.117017>.
- [134] N.K. Tolochko, S.E. Mozzharov, I.A. Yadroitsev, T. Laoui, L. Froyen, V.I. Titov, M.B. Ignatiev, Balling processes during selective laser treatment of powders, *Rapid Prototyp. J.* (2004). <https://doi.org/10.1108/13552540410526953>.
- [135] P. Wei, Z. Wei, Z. Chen, J. Du, Y. He, J. Li, Y. Zhou, The AlSi10Mg samples produced by selective laser melting: single track, densification, microstructure and mechanical behavior, *Appl. Surf. Sci.* 408 (2017) 38–50. <https://doi.org/10.1016/j.apsusc.2017.02.215>.
- [136] J.M. Walker, Additive Manufacturing towards the Realization of Porous and Stiffness-tailored NiTi Implants, 2014.
- [137] C. Tan, S. Li, K. Essa, P. Jamshidi, K. Zhou, W. Ma, M.M. Attallah, Laser Powder Bed Fusion of Ti-rich TiNi lattice structures: Process optimisation, geometrical integrity, and phase transformations, *Int. J. Mach. Tools Manuf.* 141 (2019) 19–29. <https://doi.org/10.1016/j.ijmactools.2019.04.002>.
- [138] Z. Wu, S.P. Narra, A. Rollett, Exploring the fabrication limits of thin-wall structures in a laser powder bed fusion process, *Int. J. Adv. Manuf. Technol.* 110 (2020) 191–207. <https://doi.org/10.1007/s00170-020-05827-4>.
- [139] S.K. Nayak, S.K. Mishra, C.P. Paul, A.N. Jinoop, K.S. Bindra, Effect of energy density on laser powder bed fusion built single tracks and thin wall structures with 100 µm preplaced powder layer thickness, *Opt. Laser Technol.* 125 (2020) 106016. <https://doi.org/10.1016/j.optlastec.2019.106016>.
- [140] P.C. Collins, D.A. Brice, P. Samimi, I. Ghamarian, H.L. Fraser, Microstructural Control of Additively Manufactured Metallic Materials, *Annu. Rev. Mater. Res.* 46 (2016) 63–91. <https://doi.org/10.1146/annurev-matsci-070115-031816>.
- [141] A. Pineau, A.A. Benzerga, T. Pardoen, Failure of metals I: Brittle and ductile fracture, *Acta Mater.* 107 (2016) 424–483. <https://doi.org/10.1016/j.actamat.2015.12.034>.
- [142] G.N. Dayananda, M.S. Rao, Effect of strain rate on properties of superelastic NiTi thin wires, *Mater. Sci. Eng. A.* 486 (2008) 96–103. <https://doi.org/10.1016/j.msea.2007.09.006>.
- [143] H. Sitepu, W.W. Schmahl, J. Khalil Allafi, G.F. Eggeler, T. Reinecke, H.G. Brokmeier, M. Tovar, D.M. Töbrens, Texture and Quantitative Phase Analysis of Aged Ni-Rich NiTi using X-Ray and Neutron Diffractions, *Mater. Sci. Forum.* 394–395 (2002) 237–240. <https://doi.org/10.4028/www.scientific.net/MSF.394-395.237>.
- [144] E.A. Prokofiev, J.A. Burow, E.J. Payton, R. Zarnetta, J. Frenzel, D. V Gunderov,

- R.Z. Valiev, G. Eggeler, Suppression of Ni₄Ti₃ Precipitation by Grain Size Refinement in Ni-Rich NiTi Shape Memory Alloys, *Adv. Eng. Mater.* 12 (2010) 747–753. <https://doi.org/10.1002/adem.201000101>.
- [145] S. Kou, *Welding Metallurgy*, Second. Wiley, 1987.
- [146] A. Kreitchberg, V. Sheremetyev, M. Tsaturyants, S. Prokoshkin, V. Brailovski, Optimization of Post-processing Annealing Conditions of the Laser Powder Bed-Fused Ti–18Zr–14Nb Shape Memory Alloy: Structure and Functional Properties, *Shape Mem. Superelasticity*. (2019). <https://doi.org/10.1007/s40830-019-00218-5>.
- [147] V. Brailovski, V. Kalinicheva, M. Letenneur, K. Lukashevich, V. Sheremetyev, S. Prokoshkin, Control of Density and Grain Structure of a Laser Powder Bed-Fused Superelastic Ti-18Zr-14Nb Alloy: Simulation-Driven Process Mapping, *Metals (Basel)*. 10 (2020) 1697. <https://doi.org/10.3390/met10121697>.
- [148] D. Gunderov, K. Kim, S. Gunderova, A. Churakova, Y. Lebedev, R. Nafikov, M. Derkach, K. Lukashevich, V. Sheremetyev, S. Prokoshkin, Effect of High-Pressure Torsion and Annealing on the Structure, Phase Composition, and Microhardness of the Ti-18Zr-15Nb (at. %) Alloy, *Materials (Basel)*. 16 (2023) 1754. <https://doi.org/10.3390/ma16041754>.
- [149] J.C. Chekotu, R. Goodall, D. Kinahan, D. Brabazon, Control of Ni-Ti phase structure, solid-state transformation temperatures and enthalpies via control of L-PBF process parameters, *Mater. Des.* 218 (2022) 110715. <https://doi.org/10.1016/j.matdes.2022.110715>.
- [150] P. Bellen, K.C.H. Kumar, P. Wollants, Thermodynamic Assessment of the Ni-Ti Phase Diagram, *Int. J. Mater. Res.* 87 (1996) 972–978. <https://doi.org/10.1515/ijmr-1996-871207>.
- [151] P. Jamshidi, C. Panwisawas, E. Langi, S.C. Cox, J. Feng, L. Zhao, M.M. Attallah, Development, characterisation, and modelling of processability of nitinol stents using laser powder bed fusion, *J. Alloys Compd.* 909 (2022) 164681. <https://doi.org/10.1016/j.jallcom.2022.164681>.
- [152] C. Zanotti, P. Giuliani, P. Bassani, Z. Zhang, A. Chrysanthou, Comparison between the thermal properties of fully dense and porous NiTi SMAs, *Intermetallics*. (2010). <https://doi.org/10.1016/j.intermet.2009.06.001>.
- [153] S.C. Duan, H.J. Guo, Determination of viscosity and surface tension of liquid Ni–Al–Ti system using the evaluated thermodynamic properties by AMCT, *J. Mater. Sci.* 55 (2020) 11071–11085. <https://doi.org/10.1007/s10853-020-04841-x>.
- [154] J.D. Berry, M.J. Neeson, R.R. Dagastine, D.Y.C. Chan, R.F. Tabor, Measurement of surface and interfacial tension using pendant drop tensiometry, *J. Colloid Interface Sci.* 454 (2015) 226–237. <https://doi.org/10.1016/J.JCIS.2015.05.012>.
- [155] R. Novakovic, E. Ricci, Surface and transport properties of Ni-Ti liquid alloys, *J. Alloys Compd.* 452 (2008) 167–173. <https://doi.org/10.1016/j.jallcom.2007.01.176>.
- [156] W.J. Parker, R.J. Jenkins, C.P. Butler, G.L. Abbott, Flash method of determining thermal diffusivity, heat capacity, and thermal conductivity, *J. Appl. Phys.* (1961). <https://doi.org/10.1063/1.1728417>.
- [157] R.D. Cowan, Pulse method of measuring thermal diffusivity at high temperatures, *J. Appl. Phys.* 34 (1963) 926–927. <https://doi.org/10.1063/1.1729564>.
- [158] I. V. Shishkovsky, Shape memory effect in porous volume NiTi articles fabricated by selective laser sintering, *Tech. Phys. Lett.* (2005). <https://doi.org/10.1134/1.1894427>.
- [159] K. Riener, N. Albrecht, S. Ziegelmeier, R. Ramakrishnan, L. Haferkamp, A.B.

- Spierings, G.J. Leichtfried, Influence of particle size distribution and morphology on the properties of the powder feedstock as well as of AlSi10Mg parts produced by laser powder bed fusion (LPBF), *Addit. Manuf.* 34 (2020) 101286. <https://doi.org/10.1016/j.addma.2020.101286>.
- [160] S. Gladush, *Physics Of Laser Materials Processing*, in: D. Schwoecker (Ed.), *High Power Lasers Their Ind. Appl.*, 1986: p. 188. <https://doi.org/10.1117/12.938099>.
- [161] M.J. Matthews, G. Guss, S.A. Khairallah, A.M. Rubenchik, P.J. Depond, W.E. King, Denudation of metal powder layers in laser powder bed fusion processes, *Acta Mater.* 114 (2016) 33–42. <https://doi.org/10.1016/j.actamat.2016.05.017>.
- [162] S. Dadbakhsh, M. Speirs, J.-P. Kruth, J. Schrooten, J. Luyten, J. Van Humbeeck, Effect of SLM Parameters on Transformation Temperatures of Shape Memory Nickel Titanium Parts, *Adv. Eng. Mater.* 16 (2014) 1140–1146. <https://doi.org/10.1002/adem.201300558>.
- [163] A. Klassen, V.E. Forster, V. Juechter, C. Körner, Numerical simulation of multi-component evaporation during selective electron beam melting of TiAl, *J. Mater. Process. Technol.* 247 (2017) 280–288. <https://doi.org/10.1016/j.jmatprotec.2017.04.016>.
- [164] M. Hillert, Partial Gibbs energies from Redlich-Kister polynomials, *Thermochim. Acta.* (1988). [https://doi.org/10.1016/0040-6031\(88\)87198-3](https://doi.org/10.1016/0040-6031(88)87198-3).
- [165] K. Santhy, K.C.H. Kumar, Thermodynamic assessment of Mo-Ni-Ti ternary system by coupling first-principle calculations with CALPHAD approach, *Intermetallics.* 18 (2010) 1713–1721. <https://doi.org/10.1016/j.intermet.2010.05.008>.
- [166] K. Kajikawa, K. Oikawa, F. Takahashi, H. Yamada, K. Anzai, Reassessment of liquid/solid equilibrium in Ni-rich side of Ni-Nb and Ni-Ti systems, *Mater. Trans.* 51 (2010) 781–786. <https://doi.org/10.2320/MATERTRANS.M2009351>.
- [167] W. Tang, B. Sundman, R. Sandström, C. Qiu, New modelling of the B2 phase and its associated martensitic transformation in the Ti-Ni system, *Acta Mater.* 47 (1999) 3457–3468. [https://doi.org/10.1016/S1359-6454\(99\)00193-7](https://doi.org/10.1016/S1359-6454(99)00193-7).
- [168] Z. Metzger, *The Self-Adjusting File system*, 7 (2013) 189–210.
- [169] K. Bansal, *SAF : Paving A Way to Minimal Invasive Endodontics*, 3 (2015) 144–149.
- [170] M. Solomonov, Eight Months of Clinical Experience with the Self-Adjusting File System, *J. Endod.* 37 (2011) 881–887. <https://doi.org/10.1016/j.joen.2011.02.036>.
- [171] S. Dadbakhsh, M. Speirs, J. Van Humbeeck, J.P. Kruth, Laser additive manufacturing of bulk and porous shape-memory NiTi alloys: From processes to potential biomedical applications, *MRS Bull.* 41 (2016) 765–774. <https://doi.org/10.1557/mrs.2016.209>.
- [172] J. Frenzel, E.P. George, A. Dlouhy, C. Somsen, M.F.X. Wagner, G. Eggeler, Influence of Ni on martensitic phase transformations in NiTi shape memory alloys, *Acta Mater.* 58 (2010) 3444–3458.
- [173] S. Saedi, A.S. Turabi, M.T. Andani, C. Haberland, M. Elahinia, H. Karaca, Thermomechanical characterization of Ni-rich NiTi fabricated by selective laser melting, *Smart Mater. Struct.* 25 (2016) 035005. <https://doi.org/10.1088/0964-1726/25/3/035005>.